

MODEL-BASED APPROACHES TO DIFFUSE OPTICAL IMAGING AND DOSIMETRY

Johan Axelsson

Doctoral Thesis
2009



LUND UNIVERSITY

MODEL-BASED APPROACHES TO DIFFUSE OPTICAL IMAGING AND DOSIMETRY

© 2009 Johan Axelsson
All rights reserved
Printed in Sweden by Media-Tryck, Lund, 2009

Division of Atomic Physics
Department of Physics
Faculty of Engineering, LTH
Lund University
P.O. Box 118
SE-221 00 Lund
Sweden
<http://www.atomic.physics.lu.se>

ISSN 0281-2762
Lund Reports on Atomic Physics, LRAP-412

ISBN: 978-91-628-7990-7

To my family

ABSTRACT

The work within this thesis investigates Photodynamic therapy and Fluorescence imaging for therapeutics and visualization of deeply embedded lesions.

Photodynamic therapy (PDT) is a cancer treatment modality that can eradicate tumors when light, a photosensible drug and oxygen are present. In recent decades there has been an interest in adapting this modality to deep-seated solid tumors. This requires the use of interstitially placed fibers for light delivery. The technique has been shown to be safe with minor complications but the treatment outcome show substantial inter- and intra-patient variations. This is inherited from the intrinsically complex interactions between the three components. In order to find a remedy to these problems dosimetry is needed. PDT-dosimetry adheres to the determination of parameters such as treatment time and light source positions in order to induce treatment response in the target volume, while sparing healthy tissue.

In this thesis a dosimetry scheme for interstitial PDT (IPDT) of prostate cancer has been developed. It was implemented on an instrument utilizing 18 optical fibers for light delivery and monitoring. Measurements are performed before, during and after PDT in order to evaluate the optical properties. The calculation of a light dose, based on these properties, allows patient-specific and realtime treatment dosimetry. Experimental validation of the instrument and dosimetric tools confirmed the capability to tailor a light dose to a specific target volume as well as compensate for potential variations in the light propagation. The same rationale was applied in a clinical trial incorporating four patients. A finding from the trial was that the patients were subject to under-treatment. One postulated explanation is that local absorbers and heterogenous tissue in the vicinity of the fibers will decrease the therapeutic light power. In addition the threshold dose, i.e. the light dose required for tumor eradication, was too low. This was also confirmed in a pre-clinical canine study where the light-dose was escalated.

The dosimetry scheme above only takes light into account. Work within the thesis has also been devoted to extend the dose

model so that the concentration of the photosensible drug can be included. A method has been implemented that relies on the drug fluorescence in order to assess the spatial and temporal distribution, in connection to prostate-PDT. The feasibility was concluded in an experimental study. The method has also been applied to data from the clinical trial. Initial work has also been performed using another approach to dosimetry. During treatment the drug concentration can decrease, referred to as photobleaching. The photobleaching rate is dependent on several factors such as light and oxygen. Hence by assessing the photobleaching throughout the target volume treatment assessment can potentially be performed. This was investigated with measurements acquired from the clinical trial. Potential correspondence between treatment assessment using MRI, two weeks post-PDT, and the photobleaching dose is discussed.

The determination of the drug distribution within the prostate using fluorescence can be referred to as fluorescence enhanced diffuse optical tomography (FDOT). Another vast field of research where such methods are applied, is the study of fluorescent compounds inside small animals. Then, measurements are performed on the surface of the animal followed by the execution of a theoretical reconstruction method, called an *inverse model*. Two approaches have been taken with the common goal to improve tomographic fluorescence imaging.

By acquiring fluorescence measurements in several spectral bands, means arise for localization of several fluorophores simultaneously inside the body. The problem is that the theoretical calculation is challenging and requires ample amount of computational power. In order to alleviate this problem a tomographic imaging algorithm was implemented that decrease the computational burden. Another method, also relying on multispectral measurements, was developed with the intent to increase the robustness of the theoretical problem. Experimental work on optical phantoms has been performed to verify these methods.

A problem in fluorescence imaging and tomography is the ever present autofluorescence arising from the tissue, surrounding a fluorophore. This problem was targeted using upconverting nanocrystals as fluorescent agents. In these nanocrystals, fluorescence is emitted at a shorter wavelength, compared to the excitation light. Autofluorescence, on the other hand, will be induced as normal, i.e. at longer wavelengths. Hence, autofluorescence-free imaging can be performed due to the spectral separation between the auto- and nanocrystal fluorescence. This was verified in both transillumination imaging and FDOT within an experimental phantom study.

POPULÄRVETENSKAPLIG SAMMANFATTNING

Den här avhandlingen handlar om metoder som syftar till att avbilda och behandla cancertumörer djupt inuti kroppen med hjälp av ljus.

Fotodynamisk terapi är en metod som bygger på att ljus, syre, samt ett ljuskänsligt läkemedel interagerar och ger upphov till syreradikaler. Dessa kan i sin tur reagera med vävnaden och då uppstår celldöd, s.k. nekros. Fotodynamisk terapi är vanligt förekommande inom behandling av exempelvis hudcancer. Det ljuskänsliga ämnet, som kallas fotosensibiliserare, brukar även ha en annan egenskap, nämligen att den fluorescerar. Denna process sker då läkemedlet belyses med ljus av en viss färg. Detta ljus absorberas av ämnet och avges sedan som ljus med en annan färg. I samband med t.ex. behandling av hudcancer kan man använda sig av fluorescens för att lokalisera läkemedlet. Vanligtvis kallas denna metod för fluorescensdiagnostik.

Det finns flera fördelar med fotodynamisk terapi. Till skillnad från strålningen i radioterapi är ljus helt ofarligt för kroppen. Detta gör att en patient kan behandlas vid flera tillfällen eftersom biverkningarna är små. Vid radioterapi finns det en risk att man ger för mycket strålning, vilket gör att vävnaden kan ta skada vid upprepad behandling. En annan fördel är att läkningen efter fotodynamisk terapi är mycket god.

På senare år har intresset för att behandla tumörer inuti kroppen med fotodynamisk terapi ökat. Dock är ljusets förmåga att penetrera vävnad är ganska begränsad. Därför används optiska fiber som sticks in i kroppen med hjälp av nålar. Fibrerna kopplas till en ljuskälla och leder sedan in ljuset till den plats i kroppen där behandling skall ges. Metoden kallas interstitiell fotodynamisk terapi (IPDT).

Ett instrument för IPDT-behandling har utvecklats. Detta instrument kan dels leverera ljus genom flera fibrer men även mäta ljus-transmissionen mellan fibrer när dessa är placerade inuti kroppen. Genom att göra dessa transmissions-mätningar med många

färger fås information om syresättningen inuti vävnaden. Dessutom mäts fluorescens från läkemedlet. Mätningarna utförs dels före men även under behandling. Dessa gör det möjligt att specificera behandlingsparametrar för varje individuell patient. Dessutom kan ljusutbredning, syresättning samt läkemedlets fluorescens monitoreras under behandlingens gång. Om dessa ändras kan det leda till ineffektiv behandling. Med detta i åtanke utvecklades en teoretisk metod för att kompensera för ändringar av behandlingsljusets utbredning. Instrumentet har använts i en klinisk studie där fyra personer med prostatacancer har genomgått IPDT. Målet var att behandla hela prostata men behandlingseffekt upptäcktes enbart i delar av organet.

Stort fokus har således lagts på vidareutveckling av metoden ovan. Läkemedlets distribution inuti vävnaden kan variera. Detta kan således påverka behandlingseffekten. För att uppskatta detta läkemedlets spatiella variation görs fluorescensmätningar från flera olika positioner inuti behandlingsvolymen. Mätningarna jämförs sedan med en matematisk modell där fluorescensens utbredning beräknas teoretiskt. Distributionen av fotosensibiliseraren fås när den matematiska modellen och mätningarna stämmer överens. Genom att kompensera för varierande fotosensibiliserare är vår förhoppning att behandlingsresultatet kan förbättras.

Det finns andra tillfällen då ett fluorescerande ämne skall lokaliseras. Ett exempel är avbildning av möss i djurstudier där man försöker undersöka hur t.ex. ett läkemedel tas upp av olika organ. Om man fäster ett fluorescerande ämne på läkemedlet kan detta hittas genom att söka efter fluorescens. Eftersom läkemedlet finns inuti djuret måste man ta till sofistikerade avbildningsmetoder för att kunna återskapa vad som finns på insidan. Detta kallas fluorescens-tomografi eftersom det påminner om vanlig tomografi, dock med användandet av fluorescensljus istället för röntgenstrålning. Metoder för att göra tomografiska avbildningar med hjälp av fluorescens har undersökts inom ramen för denna avhandling.

En tomografisk avbildning görs genom att svepa en ljuskälla till olika positioner på t.ex. djurets mage. Samtidigt mäts fluorescens vid olika positioner på djurets rygg. Mätningarna anpassas till en matematisk modell som beskriver fluorescensljusets utbredning inuti djuret. När modellen och mätningarna stämmer överens fås distributionen av det fluorescerande ämnet inuti djurets kropp.

Avhandlingsarbetet, har inom detta område, syftat till att vidareutveckla denna metod. Två olika fall har studerats. Det första fallet syftade till att göra det möjligt att studera olika fluorescerande ämnen som befinner sig inuti djuret samtidigt. Genom att inkludera fler fluorescensmätningar med olika färg kan den tomografiska bilden blir något bättre. Detta är generellt ett problem som kräver mycket datorkraft. Därför utvecklades en metod som kunde lösa dessa problem men fortfarande med hjälp av en vanlig

hemdator.

I det andra fallet användes nanopartiklar som fluorescerar på ett karaktäristiskt sätt. Ett vanligt problem är att vävnaden också fluorescerar, vilket stör ljuset från det som skall underökas. Med nanopartiklarna kan detta undvikas.

Sammanfattningsvis har arbetet som presenteras i denna avhandling haft prägel av teoretiska, experimentella samt kliniska aspekter.

LIST OF PUBLICATIONS

This thesis is based on the following papers, which will be referred to by their Roman numerals in the text.

I Spatially varying regularization based on spectrally resolved fluorescence emission in fluorescence molecular tomography

J. Axelsson, J. Svensson, S. Andersson-Engels.
Optics Express **15(21)**, 13574-13584 (2007).

II A matrix-free algorithm for multiple wavelength fluorescence tomography

A. Zacharopoulos, P. Svenmarker, J. Axelsson, M. Schweiger, S. Arridge, S. Andersson-Engels.
Optics Express **17(5)**, 3025-3035 (2009).

III Autofluorescence insensitive imaging using upconverting nanocrystals in scattering media

C. Xu, N. Svensson, J. Axelsson, P. Svenmarker, G. Somesfalean, G. Chen, H. Liang, Z. Zhang, S. Andersson-Engels.
Applied Physics Letters **93 (17)**, 171103-1 - 171103-3 (2008).

IV Fluorescence diffuse optical tomography using upconverting nanoparticles

C. Xu, J. Axelsson, S. Andersson-Engels.
Applied Physics Letters **94**, 251107-1 - 251107-3 (2009).

V Fluorescence monitoring of a topically applied liposomal Temoporfin formulation and photodynamic therapy of non-pigmented skin malignancies

N. Bendsoe, L. Persson, A. Johansson, J. Svensson, J. Axelsson, S. Andersson-Engels, S. Svanberg, K. Svanberg.

Journal of Environmental Pathology, Toxicology and Oncology **26(2)**, 117-226 (2007).

VI Realtime light dosimetry software tools for interstitial photodynamic therapy of the human prostate

A. Johansson, J. Axelsson, J. Swartling, S. Andersson-Engels.

Medical Physics **34(11)**, 4309-4321 (2007).

VII System for interstitial photodynamic therapy with online dosimetry - first clinical experiences of prostate

J. Swartling, J. Axelsson, G. Ahlgren, K. Kalkner, S. Nilsson, S. Svanberg, K. Svanberg, S. Andersson-Engels. (2009) *Manuscript in preparation*.

VIII In vivo photosensitizer tomography inside the human prostate

J. Axelsson, J. Swartling, S. Andersson-Engels.

Optics Letters **34 (3)**, 232-234 (2009).

Related publications:

Localization of embedded inclusions using detection of fluorescence: Feasibility study based on simulation data, LS-SVM modeling and EPO pre-processing

F. Chauchard, J. Svensson, J. Axelsson,
S. Andersson-Engels, S. Roussel.

Chemometrics and Intelligent Laboratory Systems **91**, 34-42
(2008).

ABBREVIATIONS

ALA	amino-laevulinic acid
ART	algebraic reconstruction technique
ATP	adenosine triphosphate
BLI	bioluminescence imaging
Bold-MRI	Blood-oxygen-level dependent magnetic resonance imaging
BPD	benzoporphyrin derivative
BPD-MA	benzoporphyrin derivative monoacid ring A
BT	brachytherapy
CCD	charge-coupled device
CT	computerized tomography
DE	diffusion equation
DLI	drug-light interval
DOS	diffusion optical spectroscopy
DOT	diffusion optical tomography
EBC	extrapolated boundary condition
EBRT	external beam radiation therapy
EIT	electrical impedance tomography
EGF	epidermal growth factor
EGFr	epidermal growth factor receptor
ESA	excited-state absorption
ETU	energy transfer upconversion
FDOT	fluorescence enhanced diffuse optical tomography
FEM	finite element method
FI	fluorescence imaging
FP	fluorescent protein
GB	gigabyte
GFP	green fluorescent protein

GLS	Generalized Least squares
GMRES	generalized minimum residual
HER2	human epidermal growth factor receptor 2
HpD	haematoporphyrin derivative
ICG	indocyanine-green
IDOSE	interactive dosimetry by sequential evaluation
IGRT	image-guided radiation therapy
IPDT	interstitial photodynamic therapy
LED	light emitting diode
LDL	low-density lipoprotein
LLS	Linear Least squares
Lutex	lutetium texaphyrin
MC	Monte Carlo
MI	molecular imaging
mTHPC	meso-tetrahydroxyphenylchlorin
MRI	magnetic resonance imaging
NA	numerical aperture
NIR	near-infrared
PEG	polyethylene glycol
PEI	polyethyleneimine
PET	positron emission tomography
PDT	photodynamic therapy
PMT	photomultiplier tube
PpIX	protoporphyrin IX
PS	photosensitiser
PSA	prostate-specific antigen
QD	quantum dot
RA	rheumatoid arthritis
RBC	Robin-type boundary condition
ROS	reactive oxygen species
RTE	radiative transport equation
SAI	small animal imaging
SNR	signal-to-noise ratio
SPECT	single photon emission computed tomography
SVD	singular value decomposition
TCT	targeted cancer therapy
TOF	time-of-flight
TF	treatment fraction

US	ultrasound
VTP	vascular targeted photodynamic therapy
WHO	World Health Organization
WST09	Pd-bacteriopheoporbide
WST11	Bacteriochlorophyll a derivative

NOMENCLATURE

A	internal reflection parameter
\mathbf{A}	FEM system matrix
b	scattering power
c	speed of light (mm/s)
C	calibration constant)
D	diffusion coefficient (mm)
D_{flu}	explicit Fluence dose (J/mm ²)
D_{oxy}	direct singlet oxygen dose
D_{pdt}	explicit PDT dose
D_{ps}	implicit dose metric
DPF	differential path length factor
E	energy (J)
$\mathbf{F}(\mathbf{r}, t)$	photon flux (W/mm ²)
g	anisotropy factor
\tilde{g}	normalized green function (1/mm ²)
\tilde{g}_m	fluorescence escape function (1/mm ²)
h	Planck's constant (Js)
Hb	deoxygenated haemoglobin
HbO ₂	oxygenated haemoglobin
\mathbf{J}	sensitivity matrix, Jacobian
\mathbf{I}	identity matrix
I_T	transmitted light intensity (W/mm ²)
I_0	incident light intensity (W/mm ²)
$L(\mathbf{r}, \hat{\mathbf{s}}, t)$	radiance (W/mm ² sr)
\mathbf{L}	regularization matrix
mfp'	reduced mean free path
n, n_0	refractive index
$\hat{\mathbf{n}}$	normal unit vector

$N(\mathbf{r}, \hat{\mathbf{s}}, t)$	photon distribution ($1/\text{mm}^3\text{sr}$)
1O_2	excited singlet state oxygen
3O_2	ground state oxygen
$p(\hat{\mathbf{s}}', \hat{\mathbf{s}})$	scattering phase function
$q_0(\mathbf{r}, t)$	source term (W/mm^3)
$q_m(\mathbf{r}, t)$	fluorescence source term (W/mm^3)
P_0, P	source power (W)
$q(\mathbf{r}, \hat{\mathbf{s}}, t)$	photon source term ($1/\text{sm}^3\text{sr}$)
\mathbf{Q}	FEM source vector
\mathbf{r}	position (mm)
\mathbf{r}_d	detector position (mm)
\mathbf{r}_s	source position (mm)
$R(\theta)$	reflectivity
$R_m^{+,-}$	extrapolated source-detector distance (mm)
$\hat{\mathbf{s}}, \hat{\mathbf{s}}'$	direction unit vectors
S_0	photosensitiser ground state
S_1	excited photosensitiser state
t	time (s)
T_1	excited photosensitiser triplet state
$[x]$	concentration of substance x (M or %)
z_b	extrapolation distance (mm)
$z_m^{+,-}$	extrapolated source z-position (mm)
ε	extinction coefficient (mm^{-1}/M)
η	fluorescent yield (1/mm)
γ	fluorescence quantum yield (spectrally normalized)
Γ_m	fluorescence measurable intensity
Γ_x	excitation measurable intensity
Θ	deflection angle (sr)
θ	incidence angle (sr)
θ'	refraction angle (sr)
λ	wavelength (nm) or regularization parameter
μ_a	absorption coefficient (1/mm)
μ_{af}	fluorophore absorption coefficient (1/mm)
μ_{eff}	effective attenuation coefficient (1/mm)
μ_s	scattering coefficient (1/mm)
μ'_s	reduced scattering coefficient (1/mm)
ρ	radial distance (mm)

$\Phi(\mathbf{r}_s, \mathbf{r})$	fluence rate (W/mm ²)
$\Phi_x(\mathbf{r}_s, \mathbf{r})$	excitation fluence rate (W/mm ²)
$\Phi_m(\mathbf{r}_s, \mathbf{r}_d)$	fluorescence fluence rate (W/mm ²)
Φ_F	fluorescence quantum yield
σ	singular value
$d\omega, d\omega'$	solid angle (sr)
ω	frequency (Hz)
ξ	uniformly distributed random number

CONTENTS

1	Introduction	1
1.1	Modern clinical diagnosis and therapy	2
1.2	Optical diagnosis and therapy	3
1.3	Aim and Outline of the thesis	4
2	Light-Tissue Interactions	7
2.1	Scattering	8
2.2	Absorption	9
2.3	Fluorescence	10
2.3.1	Endogenous fluorophores	12
2.3.2	Exogenous fluorophores	13
2.4	Photodynamic action	16
2.4.1	Photosensitizing agents	17
2.4.2	Biological response	19
3	Simulating diffuse light	21
3.1	The forward problem	22
3.2	Radiative transport equation	22
3.3	Diffusion equation	24
3.3.1	Boundary conditions	25
3.3.2	Source representation	26
3.3.3	Measurement representation	27
3.3.4	Diffusion equation considerations	27
3.4	Solving the forward problem	29
3.4.1	Monte Carlo model for the RTE	29
3.4.2	Finite Element Method for the DE	30
3.4.3	Analytical solutions for the DE	31
3.5	Fluorescence diffusion equation	32
3.6	Reciprocity theorem	34
4	Estimating tissue properties	35
4.1	The inverse problem	36
4.2	Measurement geometries	36
4.3	Homogeneous optical properties	37
4.3.1	Spatially resolved spectroscopy	38
4.3.2	Time- and frequency-domain spectroscopy	39
4.3.3	Fluorescence spectroscopy	40
4.4	Heterogeneous optical properties	40
4.4.1	Perturbation approach	41
4.4.2	Formulation of the general problem	41
4.4.3	The sensitivity matrix	42
4.4.4	Regularization parameter	44
4.4.5	<i>A-priori</i> information	46
4.4.6	Alternative inverse models	47
4.4.7	Practical implementation	48

5	Fluorescence imaging	49
5.1	Clinical photodiagnosis	49
5.2	Molecular imaging	52
5.3	Multispectral tomographic imaging	55
5.4	Nanoparticle-mediated imaging	58
6	Photodynamic therapy	61
6.1	Factors affecting PDT efficacy	63
6.2	Dosimetry models	66
6.2.1	Dosimetry through biological response	67
6.2.2	Direct dosimetry	67
6.2.3	Implicit dosimetry	68
6.2.4	Explicit dosimetry	69
6.3	PDT for prostate cancer	72
6.4	Rationale for prostate-PDT	74
6.4.1	Instrumentation	74
6.4.2	Procedure	74
6.4.3	Clinical study	78
6.5	Towards photosensitizer dosimetry	82
6.5.1	Explicit photosensitizer reconstruction	82
6.5.2	Analysis of reconstruction perturbations	85
6.5.3	Implicit photosensitizer reconstruction	87
A	The Finite Element Method	91
B	Least squares minimization with Tikhonov regularization	95
C	Matrix free inverse solver	97
D	Analysis of perturbations	99
D.1	Perturbation of light-fluence dose	99
D.2	Perturbation of photosensitizer reconstruction	101
D.2.1	Fiber-specific absorbers	101
D.2.2	Absorbing heterogeneities	102
D.2.3	Fiber position inaccuracies	103
	Comments on the Papers	105
	Acknowledgements	111
	References	113

Papers

I	Spatially varying regularization based on spectrally resolved fluorescence emission in fluorescence molecular tomography	143
II	A matrix-free algorithm for multiple wavelength fluorescence tomography	157
III	Autofluorescence insensitive imaging using upconverting nanocrystals in scattering media	171
IV	Fluorescence diffuse optical tomography using upconverting nanoparticles	177
V	Fluorescence monitoring of a topically applied liposomal Temoporfin formulation and photodynamic therapy of non-pigmented skin malignancies	183
VI	Realtime light dosimetry software tools for interstitial photodynamic therapy of the human prostate	195
VII	System for interstitial photodynamic therapy with online dosimetry - first clinical experiences of prostate	211
VIII	In vivo photosensitizer tomography inside the human prostate	223

INTRODUCTION

Cancer is the second most common cause of death in the world, next after cardiovascular diseases [1]. Estimates for 2008, from the World Health Organization (WHO), show that 8 million patients died due to cancer whereas 12 million new cases were diagnosed [2]. Indications with the highest incidence are shown in Figure 1.1. Furthermore, in 2030 WHO predicts that more than 20 million new cases are diagnosed [2]. To manage the cancer burden, efforts are needed in order to improve prevention, diagnosis and treatment of malignant diseases [2].

The work presented in this thesis exploits optical techniques in order to improve diagnosis and treatment of cancer. More specifically fluorescence imaging (FI) and photodynamic therapy (PDT) are investigated for imaging and therapy of deep-seated lesions.

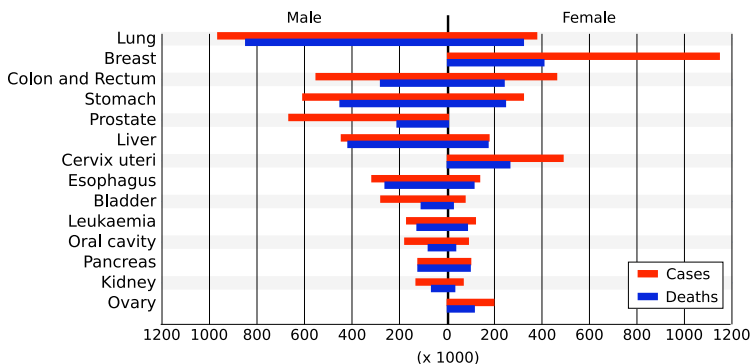


Figure 1.1. Estimated rates of incidence and death globally of different cancer indications, from Globocan 2002 [3].

Before these two optical techniques are introduced a short survey of the current state-of-art in clinical diagnosis and therapeutics is given below.

1.1 Modern clinical diagnosis and therapy

Tumor growth is initiated by abnormal mutation of cells and as neoplasia evolves the tissue structure will be affected [4]. A key aspect in cancer control, is the early detection and staging of neoplastic tissues. The probability for successful treatment is increased when therapeutic schemes are mobilized at an early stage of cancer progression [2]. Current techniques, with the intent to image these morphological changes, include X-ray, computerized tomography (CT), ultrasound (US), and magnetic resonance imaging (MRI) [5].

The abnormal tissue growth is controlled by cellular mechanisms that alter the physiology, or function, of the tissue. Current techniques, capable of image these changes, include positron emission tomography (PET) and single photon emission computed tomography (SPECT). An example is imaging of tracer compounds, attached to a biomarker. Many cancer cells show increased uptake of glucose. By attaching a radioactive isotope to a glucose analogue, that accumulates in malignant tissues, tumor-specific contrast can be retrieved [5]. Hence, the imaging targets include cellular and molecular processes, normally referred to as *molecular imaging* (MI). Both anatomical and molecular imaging techniques are applied after therapy in order to assess the treatment response [2].

In recent years, multimodality schemes have become more frequently used. Then, anatomical images are complemented with images of molecular events. This approach has rendered substantial improvements of cancer diagnosis as well as therapeutic assessment [2].

Treatment rationales rely to a large extent on surgery, chemotherapy and radiotherapy. The latter include techniques where ionizing radiation is employed, e.g. external radiation therapy (EBRT) and brachytherapy (BT) [6, 7]. The highly energetic radiation is a risk factor for cancer which potentially can induce neoplasia. Hence the absorbed dose in healthy tissue should be limited whereas the dose within the tumorous volume should be sufficiently high [8]. In other words, dosimetry is of ample importance. Improvements in treatment-planning have been reported during the recent decade where the imaging techniques, mentioned above, are used to define the target volume for the therapeutic session. This is referred to as image-guided radiation therapy (IGRT) [9].

In analogy with MI, targeted cancer therapy (TCT) relies on

the use of the biomarkers that accumulates in malignant tissue [10]. Instead of an imaging probe, a pharmaceutical is attached with the intent to render localized response. This modality has so far shown limited effect on complex solid tumors [10].

Although substantial improvements of current diagnostic and therapeutic rationales have been achieved during recent years, there are few malignancies that can be completely cured. The most devastating example is pancreas cancer with a 5 year survival rate of less than 5% [2]. Hence there is a need for additional, or complementary, treatment modalities. Furthermore, there is a need to find cellular cancer targets in order to improve targeted and tumor-specific treatments.

1.2 Optical diagnosis and therapy

In the beginning of the 20th century, Raab discovered the single-cell organisms, paramecia, were killed when exposed to a combination of light and an organic compound, acridine [11]. He postulated that this was related to the energy transfer occurring in chlorophyll, i.e. the energy transfer from light to the chemical compound. In 1907, Tappeiner demonstrated that oxygen was required for the process to occur [12]. He defined the phenomenon as *the dynamic interaction among light, a photosensitizing agent and oxygen resulting in tissue destruction*, naming it "photodynamic action".

Another class of compounds that have shown the possibility to induce photodynamic action are the porphyrins. Meyer-Betz was the first to report on human photosensitization, in 1913. He injected himself with hematoporphyrin which resulted in pain and swelling of the skin when exposed to light [13].

In addition to the photodynamic action, the porphyrins also evidence more pronounced localization in tumors. This was discovered in 1924 by Policard [14]. He observed red fluorescence from a rat tumor when illuminating with UV light. Consequently, efforts trying to identify compounds that had tumor-seeking properties were initiated. In 1955, Schwartz concluded that the compound hematoporphyrin was a mixture of several substances. Lipson et al. later isolated one of these and reported on improved tumor-selectivity as compared to the original mixture [15]. The isolated compound is called Hematoporphyrin Derivative (HpD). Following this work, HpD became a well studied agent for localization of malignant neoplasia employing fluorescence imaging, see e.g. [16, 17]. We note that due to the tumor-selectivity of some photosensitizers, these agents can be categorized as molecular imaging probes.

A major milestone was reached when Dougherty et al. reported on complete tumor response in animal tumor models in 1975 [18]. This work showed that successful, and selective, tumor

treatment could be obtained when utilizing HpD and red light illumination 24-48 hours post drug-administration. With this rationale, Dougherty et al. later initiated a clinical trial where various superficial indications were targeted [19]. Today, PDT is approved for numerous indications.

PDT holds some advantages compared to radiotherapy [20]. Light is non-ionizing, hence there is no cumulative toxicity which is the case in therapeutics with ionizing radiation. This fact allows repeated treatments of e.g. recurrent malignancies. Furthermore some photosensitizers have the important property to selectively accumulate to a higher degree in tumors. Another important feature of PDT is that healing after treatment is excellent. The photodynamic action spares collagen which is the main component in connective tissues [21]. Most photosensitizing agents are fluorescent. This is exploited, as above, for tumor localization but also for assessment of treatment progression.

A disadvantage of PDT may be the short penetration depth of light. In order to remedy this problem a new generation of photosensitizers have been developed throughout recent decades. These are all activated at longer wavelengths where light is less attenuated. In addition interstitially placed optical fibers are used to target solid tumors deeply embedded within the body. When applying this rationale dosimetry is of ample importance.

In addition to molecular imaging in radiology, mentioned in Section 1.1, optical molecular imaging is a progressing field of research. Here fluorescence imaging plays an important role since ample amount of fluorescent agents exist [22]. The common rationale is to attach fluorophores to target probes which then provides contrast for a specific cell receptor, cell mechanism or process. An important application of fluorescence based molecular imaging is pre-clinical research where small animals are imaged.

As many biological process occur deep inside the body, there is a need for methods that can reconstruct the internal distribution of a fluorophore. This method is referred to as *fluorescence enhanced diffuse optical tomography* (FDOT) which is explained in detail in this thesis.

1.3 Aim and Outline of the thesis

Two general aims can be stated

- (i) to improve fluorescence imaging and tomography of fluorescent agents
- (ii) to improve PDT and PDT-dosimetry for treatment of deep-seated tumors

The progress towards these goals are detailed in the outline below.

Chapter 2 details the light-tissue interactions occurring when light propagates through biological media, i.e. scattering, absorption, fluorescence and photodynamic action.

Chapter 3 is focused on the theoretical aspects of how light propagation is modeled, i.e. the *forward model*.

Chapter 4 describes different theoretical schemes, i.e. *inverse models*, for estimation of the optical properties of the tissue. These properties provide the foundation for optical diagnosis and are inherently connected to the light-tissue interactions.

Chapter 5 gives an overview of fluorescence imaging.

The first two parts provide a review of fluorescence imaging for clinical diagnosis and molecular imaging.

The third part adhere to multispectral measurements of fluorescence and how these measurement can be employed in the reconstruction of fluorescent inclusions. Essentially two ways are investigated. In Paper **I** a multispectral approach was taken that rendered increased robustness to the theoretical tomographic reconstruction problem. The capability to image several fluorophores, i.e. multilabeling, was rendered with the scheme presented in Paper **II**.

In the fourth part, upconverting nanocrystals employed as fluorescent agents are introduced. The motivation for using these particles is that the measurements are not affected by the background fluorescence. Papers **III** and **IV** present the experimental demonstration of imaging and tomography of these agents.

Chapter 6 discusses several aspects related to PDT.

In the first part, factors affecting the treatment outcome, or efficacy, are presented. In Paper **V** one of these factors, namely the tumor localization was investigated using a liposomal formulation of the photosensitizer.

The second part holds information about different *dose models* that can be adopted with the intent to predict the outcome.

The third part reviews the current status of PDT for prostate cancer.

In the fourth part, our efforts towards patient-specific and realtime dosimetry for interstitial PDT of the prostate is summarized. An instrument incorporating optical fibers for light delivery and monitoring has been developed. The instrument acquires optical measurements during the therapeutic session and these are used to evaluate the treatment

progression. The dosimetric tools for this evaluation is presented in Paper **VI**. Furthermore the rationale was applied in a clinical trial incorporating four patients. The results are presented in Paper **VII**. A finding from the trial was that the patients were subject to undertreatment. Discussion and analysis of the cause behind this is included in this part as well as Appendix D.

The last part introduce the use of tomographic imaging of photosensitizer distribution inside the prostate. The reconstruction scheme is presented in Paper **VIII**. Furhermore, reconstruction of the temporal variation of the drug, during treatment, is implemented and discussed in this part.

LIGHT-TISSUE INTERACTIONS

When light propagates in biological media it will interact with the tissue constituents. The two fundamental interactions are elastic scattering and absorption which are responsible for determining the photon distribution within the medium. Following absorption in a fluorophore, fluorescence is emitted. The fluorescence can indicate disease and the quantification of fluorophores based on fluorescence detection is a recurrent theme throughout this thesis. Fluorescence is naturally occurring but often exogenous probes are employed to increase imaging contrast. The main advantage with the exogenous probes is that they can target specific biological and cellular components, increasing the specificity for e.g. cancer man-

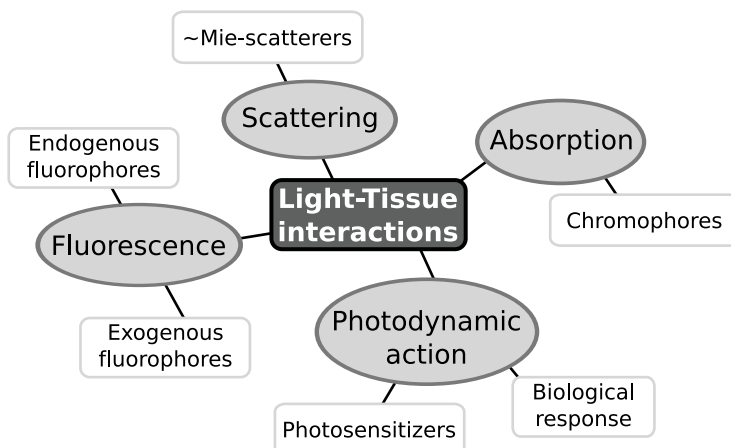


Figure 2.1. Graphical representation of the contents of present chapter.

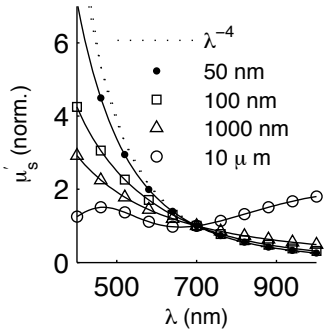


Figure 2.2. The influence of particle size on the reduced scattering coefficient as predicted by Mie-scattering theory. μ'_s is normalized with $\mu'_s(\lambda = 700)$.

ifold. A special type of exogenous probes are the photosensitizers. Apart from fluorescence they can also induce photodynamic action which is the basis for the tumor treatment modality Photodynamic therapy.

In this chapter the light-tissue interactions will be introduced according to the graphical representation in Figure 2.1.

2.1 Scattering

Tissues are composed of cells where the intracellular organelles and extracellular structures form a complex matrix that macroscopically govern the anatomy of the organs. Evidently there exist numerous of different tissue types each with its own composition of constituents. For instance connective tissues hold collagen and elastin proteins whereas muscular tissues are built up by muscle cells filled with myosin and actin. Irrespective of what tissue is regarded the origin of scattering is thought to be the same namely the variation of refractive index within the medium [23]. In addition the size of the tissue components will affect the scattering. The size distribution range from *nm* (proteins) to μm (cells). This fact has rendered the use of scattering-based diagnostic methods to probe morphological changes in the tissue [24, 25].

In the theoretical analysis of scattering properties, the tissue components are assumed to be spherically shaped particles. The electromagnetic wavepropagation is then modeled within the framework of Mie theory. The scattering from one sphere can then be described by the radiation caused by a dipole induced through the interaction with the incident electromagnetic field [26]. Mie-theory can very well describe the scattering pattern from a limited number of spheres but the complexity of biological tissues make it impractical to adopt in real applications. Normally in tissue optical studies the macroscopic properties are of interest. Then two physical quantities are defined; the scattering coefficient μ_s and the anisotropy factor $g = \langle \cos(\theta) \rangle$, where θ is the scattering angle. μ_s states the probability for scattering per unit length. g holds the information about what direction, on average, the light is scattered. As will be further discussed in Section 3.2 the scattering angle is given by a probability density function called the phase function. The composition of tissue renders an anisotropy factor approaching unity meaning that a biological medium is forward scattering. In highly scattering tissues the two quantities are combined into the reduced scattering coefficient $\mu'_s = (1 - g)\mu_s$. Empirical findings alleviate the analysis of the macroscopic scattering [27]. The general approach is to describe the spectrally dependent scattering according to

$$\mu'_s = a\lambda^{-b} \quad (2.1)$$

where a is the scattering amplitude reflecting the number density of spherical particles in the tissue, while b is the scattering power related to the particle size [25]. When the particles are very small compared to the wavelength $\mu'_s \propto \lambda^{-4}$, the so called Rayleigh limit. As depicted in Figure 2.2 the scattering power decreases when particle size increase [28].

2.2 Absorption

When light encounter an absorbing chromophore where the energy difference between two electronic states match the energy carried by the optical radiation it can be absorbed. Due to this fact the absorption is spectrally dependent and forms the basis for an ample amount of applications. If the scattering of a medium is negligible the transmitted intensity (I_T) decreases exponentially with propagation distance (d) according to the Beer-Lambert law, i.e.

$$I_T(\lambda) = I_0(\lambda) \times \exp(-\mu_a d). \quad (2.2)$$

Here μ_a is the absorption coefficient stating the probability of absorption per unit length. The absorption coefficient is essentially the summation of all chromophore contributions, i.e.

$$\mu_a(\lambda) = \sum_i \varepsilon_i(\lambda)[C_i] \quad (2.3)$$

where ε_i and C_i is the extinction coefficient and concentration respectively for chromophore i . In biological tissues the scattering is normally much larger than absorption hence the Beer-Lambert law can only be applied with modifications and in certain occasions [29]. A more rigorous theoretical approach is given in Chapters 3 and 4. The main absorbing chromophores in biological tissues are given below.

Hemoglobin can be oxygenated or deoxygenated. The spectral absorption characteristics of the two forms are different, seen in Figure 2.3, which can be utilized to assess the tissue oxygenation [33, 34]. The tissue oxygenation is a valuable tool in assessment of hypoxia since the status of a tumor can show oxygen deficiency.

Water absorbs mainly in the NIR wavelength region, depicted in Figure 2.3. Water is present in abundance throughout the body and normally represented by the water fraction (% of pure water).

Lipids is the family name of many different types of substrates. An example where lipids play an important role is as a building block in the cell membranes. Similar to water, lipids

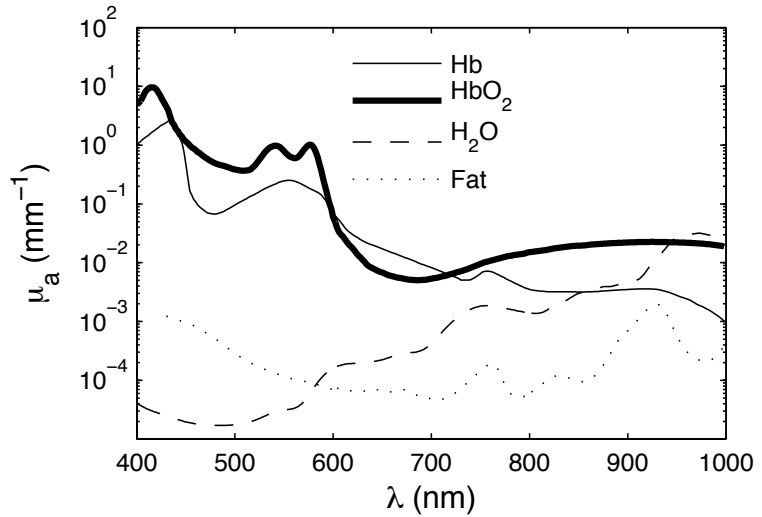


Figure 2.3. Absorption coefficient for the main absorbing chromophores in biological tissues. The absorption coefficient is calculated using 20 μM deoxygenated hemoglobin (Hb), 80 μM oxygenated hemoglobin (HbO_2) [30], 70 % water (H_2O) [31] and 15 % fat [32].

absorb at longer wavelengths seen in Figure 2.3. Although a comparatively weak absorber, relative water, it has been reported that the lipid content was reduced in malignant breast tumors indicating potential for lipid-spectroscopy [35].

Melanin acts as a protecting layer for the sun's UV radiation thus present in the superficial skin. Melanin is responsible for the color of our skin. It can also be found in other parts of the body, e.g. brain [36].

Myoglobin has similar absorption characteristics as hemoglobin and both oxy- and deoxy-myoglobin exist. Myoglobin is mainly found in muscular tissues [37].

Cytochromes are substrates with the common feature that they reflect the mitochondrial content. A spectroscopic assessment of such substrates could potentially render information about the metabolism of the medium under study [38].

2.3 Fluorescence

Following the absorption of light in a chromophore the excess energy must dissipate. One route is the emission of lower energy op-

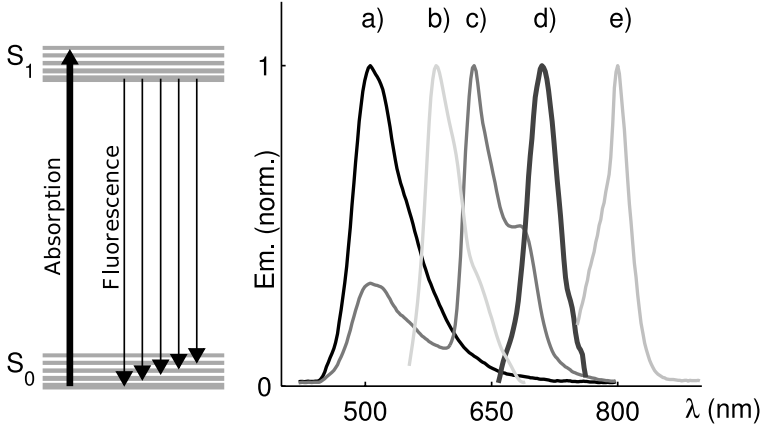


Figure 2.4. (left) Schematic Jablonski diagram depicting the fluorescence process. (right) Fluorescence spectra from selected fluorophores. The spectra are normalized to maximum intensity while the excitation wavelength is indicated in parenthesis for a) skin (405 nm), b) DsRed (545 nm), c) ALA-induced PpIX on skin (405 nm), d) mTHPC (652 nm), e) Dy782 (782 nm)

tical radiation, called fluorescence, see Figure 2.4. A chromophore where this process takes place is defined as a fluorophore. Consider light incident on a unit volume fluorophore. The excitation light intensity is given by $I_0(\lambda_x)$ [W/m^2] and the absorbed power per unit volume is given by $\mu_{af}I_0(\lambda_x)$. The fluorescent power per unit volume is then stated as [39]

$$I_F(\lambda_x, \lambda_m) = \gamma(\lambda_x, \lambda_m)\mu_{af}(\lambda_x)I_0(\lambda_x). \quad (2.4)$$

Here $\gamma(\lambda_x, \lambda_m)$ is the probability for the event resulting in emission of a fluorescence photon within a spectral band centered at wavelength λ_m . $\gamma(\lambda_x, \lambda_m)$ can be retrieved from the quantum yield (Φ_F), i.e.

$$\frac{1}{\Phi_F} \int_0^{\infty} F(\lambda_x, \lambda_m)d\lambda_m = \frac{1}{\gamma(\lambda_x, \lambda_m)} \int_{\lambda_m - \Delta\lambda/2}^{\lambda_m + \Delta\lambda/2} F(\lambda_x, \lambda_m)d\lambda_m. \quad (2.5)$$

$F(\lambda_x, \lambda_m)$ is the probability for inducing fluorescence per spectral band hence it defines the fluorescence spectrum [39]. The absorption coefficient in Equation (2.4) can be stated in terms of extinction coefficient and concentration, as seen in Equation (2.3) hence the fluorescence emission is linearly dependent on the concentration. Normally the *fluorescent yield* is defined as $\eta(\lambda_x, \lambda_n) = \gamma(\lambda_x, \lambda_m)\mu_{af}$ [40]. The quantum yield is affected by the environment in which the fluorophore is present. Temperature, pH and

presence of quenchers are factors that will introduce alterations of the quantum yield hence inducing spectral shifts in the measured fluorescence spectrum [39].

In addition, to the steady-state treatment above, the fluorescence process has a temporal dependence. When the fluorophore is excited by a short light pulse the fluorescence emission will decay exponentially as a function of time. The *fluorescence lifetime* is in the order of ns but can be altered dependent on the biochemical environment [39, 41].

2.3.1 Endogenous fluorophores

Endogenous fluorophores exist naturally in biological tissues and fluoresce mainly when excited by UV-radiation [24, 42, 43]. The fluorescence from the endogenous fluorophores is called *autofluorescence* and a typical example from skin is seen in Figure 2.4a. Apart from the porphyrins the endogenous fluorophores emit spectra without any distinct spectral features. A difficulty with autofluorescence spectroscopy is then to spectrally decompose the measured spectra into its fluorophore constituents. In addition only surface examination is possible due to the high tissue absorption in the UV wavelength range. The most important endogenous fluorophores are summarized below.

NADH and **FAD** take part in the metabolism within cells. NADH is the reduced form of nicotinamide adenine dinucleotide while FAD is the oxidized form of flavin adenine dinucleotide. The fluorescence due to these substrates is reduced within tumors relative healthy tissues due to changes in metabolic states. This alteration in cell function forms an important tool in cancer diagnostics [43, 44].

Collagen and **Elastin** build up the connective tissues. Fluorescence due to these proteins can indicate biochemical changes in tissues [45].

Lipopigments are granules of oxidized lipids, e.g. lipofuscin, that are present in the cytoplasm. These fluorophores are associated with ageing, retinal degeneration and atherosclerosis [43, 46].

Amino acids such as tryptophan, tyrosine and phenylalanine contribute to the tissue fluorescence. The amino acids act for example as building blocks in the biosynthesis of several proteins.

Porphyrins are compounds acting within the heme cycle. They emit red fluorescence upon excitation in the UV-blue wavelength region. Porphyrins can be classified as endogenous

photosensitizers and will be further described in Section 2.4.1.

2.3.2 Exogenous fluorophores

Exogenous fluorophores are fluorescent probes that need to be administered to the tissue. An astounding number of probes are available due to development triggered by the use in fluorescence microscopy for tissue studies. Despite this only a limited number is clinically approved for humans. Conversely, in small animal imaging there exist several classes summarized here.

Systemic fluorophores are non-specific substrates without the affinity to bind to a particular tissue component. The clinically approved probe indocyanine-green (ICG) can be categorized into this class. It binds to albumin in the blood and is used to demarcate vasculature [47]. Increased vascularization within a volume is commonly associated with malignant tissue [48].

Targeting probes are composed of two substrates fused together; one fluorescent compound and one targeting molecule. The targeting molecule, or ligand, is responsible for binding to a specific receptor on e.g. the cell membrane whereas the fluorescent molecule produce imaging contrast upon excitation [49]. Disease targeting can be accomplished through the use of antibodies that bind to specific antigens present in e.g. neovascularized tissue [50] or certain forms of cancer [51]. A peptide, such as epidermal growth factor (EGF), is another example of a ligand that can mark solid tumors through the binding to epidermal growth factor receptor (EGFr). EGFr is commonly indicative of tumor progression [52]. Inflammatory disease, such as rheumatoid arthritis (RA), can also be imaged when fusing a fluorophore with a folate-molecule since folate-receptors are abundant in RA [53]. The choice of fluorophore is dependent on the derivatization process, i.e. fusing between target molecule and fluorescent compound. The chemistry of the fluorophore and the targeting ligand must be compatible but fortunately a wide variety exist [54]. An example of a fluorophore that can be used in targeted fluorescence imaging is DY782, see Figure 2.4e. The main complication, apart from finding specific ligands, is that fluorescence can be emitted even though the probe has not found its binding site. Typically imaging is performed several hours after administration in order to reach a sufficient amount of the probe attached to its target whereas the rest is cleared from the body.

Activatable probes are a type of targeting probes that can emit fluorescence only after a specific event has occurred. Typically enzyme-mediated activity, e.g. tumor-specific proteases are imaged [55]. The probe is composed of several fluorophores

joined together with a peptide link. Due to the small distance between the molecules the fluorophores are initially quenched, hence non-fluorescent. Upon reaction with a protease the link breaks and the probe becomes fluorescent [55]. High specificity is reached due to the increased target-to-background contrast as compared to normal targeting probes, mentioned above.

Smart probes are another type of activatable probes. These fluorophores alter their fluorescence spectra upon binding to a specific substrate within a cell. Intracellular ions, e.g. calcium (Ca^{2+}), can in this way be imaged [56]. Spectral shifts can also occur whenever the environment, in which the fluorophore sits, is changed. A typical application is indication of pH-changes [57].

Fluorescent proteins (FPs) are genetically encoded into an animal's genome, e.g. in transgenic mice. The genome holds the DNA which is responsible for protein synthesis within all cells. Proteins are important since they take part in all physiological processes occurring in the body; from cell signaling to organ function. The important feature of protein synthesis is that all proteins are not produced by all cells, although the DNA is present in every cell nucleus. This arises from the transcription factors that control, i.e. regulate, what proteins that should be synthesised. Evidently the cells throughout the body do not have the same function hence different transcription factors are activated. Upon activation the DNA is transcribed into RNA which in turn diffuses out from the cell nuclei. The RNA is then translated, meaning that the protein is constructed by amino-acids present in the cytoplasm [58]. In malignant cells this process, i.e. gene expression, is altered in several ways [59]. Fluorescent proteins provide the possibility to visualize the gene expression. In essence the FPs are introduced into the genome as reporter genes. When the gene is transcribed the FP is automatically fused to the specific protein. The fluorescence originating from a substrate will then indicate the occurrence of a specific event as well as the localization [60, 61]. The first fluorescent protein to be imaged using this rationale was the green fluorescent protein (GFP) [60]. Due to limiting factors, such as autofluorescence and low penetration depth, FPs emitting at longer wavelengths are now being developed and employed [59, 62, 63]. A spectrum from the red fluorescent protein DsRed is seen in Figure 2.4b.

Nanoparticles in different forms can be used. These are semiconductor crystals where the absorption and emission characteristics can be controlled through the size of the particle. Generally these particles are small, in the order of several nm, giving rise to the name Quantum Dots (QDs). Compared to biological fluorophores the absorption spectra is broad and the

extinction coefficient increase with shorter wavelengths. This fact arise from the presence of a band-gap in all semiconductors [64]. Whenever the excitation light energy overcome the band-gap the QD can be excited. Following excitation electron-hole pairs are generated. Recombination of these give rise to fluorescence. The emission spectrum from a QD is characteristic in that is symmetric, around a center-wavelength and relatively sharp (~ 50 nm). By changing the size of the QD the quantized energy levels are altered. In turn this will change the center-wavelength of the emission profile. Another feature of the QD-emission is the long fluorescence lifetime [65]. QDs are normally coated, meaning that a protective shell is grown outside the semiconductor core. The coating renders many advantageous feature. First the photostability and quantum yield is increased since the shell prohibit non-radiative recombination. This allows long-term imaging and it has been reported that QDs can be retained in the mouse-body for months [64]. Secondly the chemical composition of the shell can be of varying art providing the basis for biocompatible and targeting QDs. The semiconductor crystal is hydrophobic and to avoid aggregation it can be made water-dispersible through coating with amphiphilic compounds [66]. A common approach is to employ polyethylene glycol (PEG) that will prolong the circulation time and possibly the retention to tumor sites [67]. The vast arsenal of targeting moieties adapted from biological probes, exemplified in previous sections, can also be realized for QDs. The fusing of e.g. antibodies, peptides or other disease-targeting ligands, normally referred to as functionalization, can increase the specificity manifold [66, 67].

Another range of nanoparticles receiving ample interest in recent years are the lanthanide-doped nanocrystals [68]. They hold an interesting property in that the fluorescence emission is up-converted. In essence this means that excitation is performed at longer wavelengths, typically NIR-radiation, whereas a two-photon process will present fluorescence at a shorter wavelength. Application of such particles in small-animal imaging renders practically autofluorescence-free imaging, see Papers **III** and **IV** as well as [69, 70]. The use of up-converting nanocrystals will be further discussed in Chapter 5.

Photosensitizers can selectively accumulate, to various degrees, in malignant tissues providing an alternative for cancer diagnosis based on fluorescence measurements [15, 16, 71, 72]. Different photosensitizer classes and their properties are summarized in Section 2.4.1

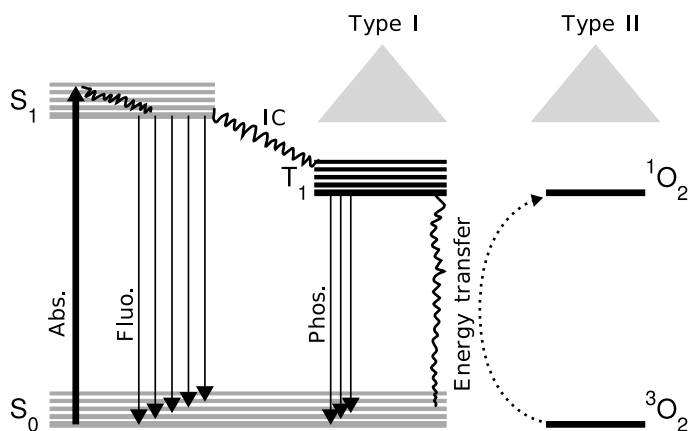


Figure 2.5. Schematic Jablonski diagram of the photodynamic process. The notation is defined by (S_0) Photosensitizer ground state, (S_1) Excited state, (T_1) Triplet state, (Abs.) Absorption of treatment light, (Fluo.) Fluorescence, (IC) Intersystem crossing, (Phos.) Phosphorescence, (3O_2) Oxygen triplet ground state and (1O_2) Oxygen singlet excited state.

2.4 Photodynamic action

While some photosensitizers fluoresce all of them have the important property to mediate the photodynamic action. Following absorption of light the excited molecule can decay to its ground state through fluorescence, radiation-less energy dissipation or intersystem crossing (IC) to its triplet state (T_1), see Figure 2.5. Since a transition from triplet to singlet state is quantum mechanically forbidden the life time of the photosensitizer triplet state is long (\sim ms). The longer lifetime increases the possibility for the photosensitizer to transfer its energy through collisions with other compounds present in the tissue. In environments where oxygen is abundant the dominating interaction is between the photosensitizer triplet state and oxygen triplet ground state (3O_2). The reaction is termed *Type II*-reaction and generates excited singlet oxygen (1O_2) [73]. The singlet oxygen is highly reactive hence the diffusion distance is very short (\sim 10 nm) before it interacts with a biological substrate. *Type I*-reactions occur when the photosensitizer, excited to its triplet state, interacts with other substrates than oxygen. This typically occurs in hypoxic tissues or when photosensitizer concentration is high [74, 75]. The reactive compounds produced by either Type I or II reactions are referred to as reactive oxygen species (ROS). Most photosensitizers are believed to render a Type II reaction [76]. Hence singlet oxygen is the important

ROS that will interact with tissue constituents, cells and subcellular structures leading to cell death, vascular shutdown and immunological response. The intention with photodynamic therapy is to induce these processes in malignant cells, ideally rendering tumor regression.

2.4.1 Photosensitizing agents

Most photosensitizers used today contain the aromatic compound *tetrapyrrole* [77]. Through alterations of the chemical structure the photosensitizer can adopt different properties in terms of its ability to fluoresce and mediate generation of ROS. The chemical structure also defines the hydrophobicity, or hydrophilicity, of the molecule which will influence the biodistribution of the photosensitizer when administered to the vasculature. In general terms; hydrophobic, and amphiphilic, agents bind to lipoproteins, such as low-density lipoprotein (LDL), present in the blood [78]. Due to the agent's hydrophobicity these compounds are normally administered in a formulation making it more soluble in water. Hydrophilic photosensitizers preferentially bind to albumin when injected into the bloodstream [79, 80]. The photosensitizer complex will diffuse through the vessel walls and eventually be taken up by cells. Malignant cells are believed to hold a higher number of LDL-receptors leading to increased uptake of agents bound to LDL [81, 82]. Albumin-bound agents on the other hand mainly localize in the tumor stroma, i.e. connective tissues within the tumor [79]. Selective retention can also be attributed to the leaky vasculature and the poor lymphatic drainage commonly present in tumors [83]. The main classes of photosensitizers commonly utilized in photodynamic therapy are discussed below.

Porphyrins are compounds that take part in e.g. the biosynthesis of heme. It was early discovered that porphyrin mixtures could selectively localize to malignant tissue. The first photosensitizer to be studied was Hematoporphyrin Derivative (HpD) [19]. By removing less photoactive compounds from the mixture the purified version, called Porfimer sodium (Photofrin[®]), is retrieved. The ability to localize to tumors is highly dependent on the porphyrin mixture since the compounds will bind to different intracellular species [84].

In addition to the chemically refined hematoporphyrins above a naturally produced photosensitizer exist, namely Protoporphyrin IX (PpIX) [85]. A precursor to PpIX is 5-Aminolevulinic Acid (ALA). When administered to the tissue ALA will undergo several enzymatic reactions yielding a higher concentration of PpIX. When the enzyme ferrochelatase is present in the cells PpIX will be transformed to heme [86]. Deficiency of ferrochelatase in malignant cells leads to selective accumulation of PpIX in tumor

tissues [87]. PpIX is fluorescent and a spectrum acquired from human skin is shown in Figure 2.4c. Porphyrins are photodynamically activated using light sources emitting at 630-635 nm. Due to the blood absorption in biological tissue the penetration depth is fairly short. PpIX is cleared from the body with one or two days [85]. The porphyrins, on the other hand, are cleared slowly from the tissues which practically means that photosensitivity remains for 4-6 weeks after administration [75]. These factors have triggered to development of alternative photosensitizers.

Chlorins have red-shifted absorption spectra relative the porphyrins due to alterations in the aromatic ring present in both chlorins and porphyrins [74]. This leads to increased penetration depth of the treatment light. Benzoporphyrin derivate (BPD) or Benzoporphyrin derivate monoacid-A (BPD-MA, Verteporfin[®]) is activated at 692 nm leading to larger treatment volumes. In addition it is fluorescent when excited at shorter wavelengths [88]. BPD binds to lipoproteins hence targets the LDL-receptors of malignant cells. This leads to slightly higher retention in tumor tissue as compared to normal muscle tissue [82]. The important feature though is the fast clearance of BPD which is in the order 24-48 hours leading to low systemic photosensitivity [89, 90]. In addition to cancer therapy, BPD is employed to a large extent in the treatment of choroidal neovascularization due to age-related macular degeneration [89, 91].

Meso-tetra(hydroxyphenyl)chlorin (mTHPC, Foscan[®]) is termed to be the most potent photosensitizer present [74, 92]. Several factors are responsible for this definition. The extinction coefficient at the treatment wavelength is large as compared to the porphyrins. In addition the intracellular localization is believed to render increased photodynamic efficacy [93]. mTHPC is activated at 652 nm and fluoresce around 710 when excited with the treatment light, see Figure 2.4d. This fact is exploited in Paper **VIII** for estimation of mTHPC-concentration in the human prostate. mTHPC is a hydrophobic agent hence is normally administered in a polyethylene glycol (PEG) formulation in order to avoid aggregation and prolong circulation time. The clearance of mTHPC is slower than BPD-MA; approximately three weeks [74].

Bacteriochlorophylls are compounds related to chlorophyll implying the capability to transform light to oxygen. Replacing the magnesium atom, within the bacteriochlorophyll, with a palladium atom the photosensitizer WST09 (Tookad[®]) can be produced. WST09 has low solubility in aqueous solutions hence the agent is normally delivered in an amphiphilic formulation, i.e. Chremophor[®] [94, 95]. The excitation is performed at 762 nm. An important feature is the high yield for transition to the triplet state. Conversely the yield for fluorescence is very low [96]. The

photoactive agent is different from other agents in that it stays in the vasculature and is not taken up by malignant cells [97].

A water-soluble version of WST09 has recently been developed, namely WST11 (Stekel[®]) [98]. It has the same features as WST09 without the need for an administration vehicle, such as Chremophor[®]. It has been shown that WST11 binds to albumin limiting the uptake of the drug by cells [99]. The intention by employing WST09 or WST11 is to target the vasculature instead of the cancer cells directly. The limited uptake in tumor cells also leads to fast clearance in the order of an hour.

Texaphyrins is a family holding e.g. the photosensitizer Lutetium texaphyrin (Lutex). Treatment light at 732 nm is utilized to activate this amphiphilic water-soluble agent [100]. In addition the agents is fluorescent when excited by shorter wavelengths [101]. Limited phototoxicity is rendered due to the fact that the clearance time is relatively short, i.e. 24-48 hours [102]. The photosensitizer is believed to bind to lipoproteins hence tumor selectivity is rendered through LDL-receptor targeting [103]. An interesting feature of the texaphyrin is that it can act as a magnetic contrast agent in addition to its photoactive properties. This is achieved by replacing the diamagnetic lutetium with the paramagnetic ion gadolinium in the texaphyrin core [100, 104].

2.4.2 Biological response

As mentioned above the excitation of the photosensitizer causes generation of ROS which in turn will interact with the cells in close proximity to the generation site. The outcome is highly dependent on the intra- and inter-cellular localization of the photosensitizer. The biological response can be divided into three main categories, as described below. In addition the light irradiation time and power as well as incubation time will influence the therapeutic outcome. Since these parameters are within the scope of PDT dosimetry they are left for Chapter 6. The predominant photosensitizer localization and biological response are summarized in Table 2.1.

Direct cell death through *necrosis* occurs when the ROS oxidize sub-cellular structures or the plasma membrane [106]. Characteristic features of such events are cytoplasm swelling, destruction of organelles and release of intracellular contents. Necrosis is typically a rapid process leading to cell degeneration [107–109].

Apoptosis is a result of the altered cellular signaling induced by the photodynamic action within sub-cellular structures such as mitochondria, lysosomes and endoplasmic reticulum. This "suicidal" pathway requires ATP and the cell is intact during

Photosensitizer	Localization	Response
Photofrin	Golgi apparatus	Direct cell death
	Plasma membrane	
ALA-PpIX	Vascular endothelium	Vasular damage
	Mitochondria	Direct cell death
	Cytosolic membranes	
BPD	Mitochondria	Direct cell death
	Perinuclear	
mTHPC	Vascular endothelium	Vasular damage
	Endoplasmic reticulum	Direct cell death
	Mitochondria	
WST09/11	Vascular endothelium	Vasular damage
	Serum proteins	Vasular damage
Lutex	Lysosomes	Direct cell death
	Vascular endothelium	Vasular damage

Table 2.1: Photosensitizer localization and response [77, 91, 105].

the apoptotic process [110]. An apoptotic cell is characterized by cell shrinkage and membrane blebbing, i.e. that the cellular wall bulge outwards [107]. The residues after apoptosis are consumed by phagocytes. The mitochondria play an important role in the apoptotic route due to the release of cytochromes, e.g. cytochrome c, that activate caspases [109, 111]. These enzymes are then responsible for DNA fragmentation leading to cell mortality [110].

Vascular shutdown, also referred to as indirect cell death, occurs when the epithelial cells in the vessel wall are damaged [91, 112]. In addition the blood platelets can aggregate forming blood flow stasis [113]. In this way ischaemia is induced hence limiting the oxygen and nutrient supply to the cells [114].

Immunological response is induced in all of the above inflections through an acute inflammation following photodynamic action [115]. Alterations in cell signalling will cause neutrophils, i.e. a type of white blood cells, mast cells and macrophages to assemble within the traumatized region [116–118]. In addition the lymphoid T cells can cause a systemic immune response following photodynamic action [119, 120]. This photo-induced immune response could have ample importance in preventing recurrence of malignancies [115]. Opposed to this advantageous feature of photodynamic action, chemotherapy, radiotherapy and surgery all suppress the immune system [115].

SIMULATING DIFFUSE LIGHT

A prerequisite for quantitative imaging and dosimetry is the ability to simulate light propagation. This procedure is described by the *forward model* which is the topic of this chapter. In Chapter 2 the tissue optical properties were introduced for scattering $[\mu_s, g, \mu'_s]$, absorption $[\mu_a]$ and fluorescence $[\gamma, \mu_{af}]$. These theoretical properties define how the light propagates through the tissue. As will be seen in Chapter 4 the forward problem plays a central role when optical properties of the medium are assessed.

The contents of this chapter is depicted in Figure 3.1.

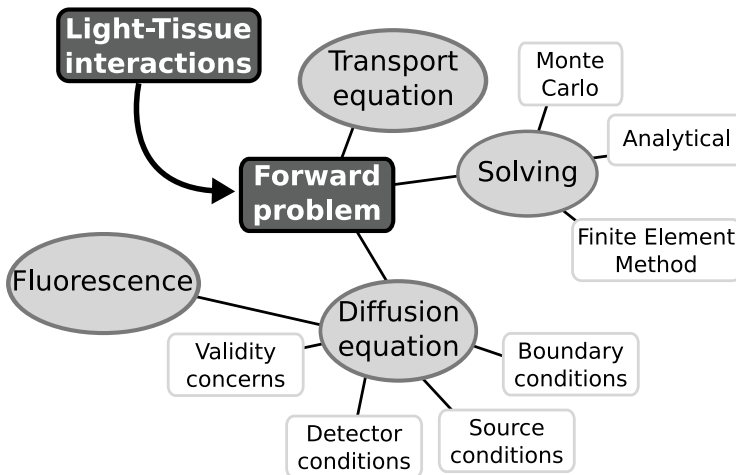


Figure 3.1. Graphical representation of the contents of present chapter.

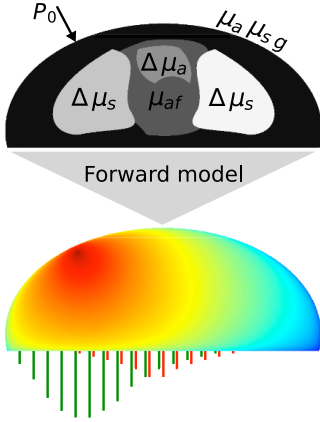


Figure 3.2. A schematic picture describing the forward problem where the light propagation within a medium is simulated.

3.1 The forward problem

In the forward problem one seeks a solution to the forward model describing the light propagation within a medium, schematically depicted in see Figure 3.2. The requirement is the knowledge of the tissue optical properties. When proper boundary conditions are implemented the boundary exitance can be computed.

The theoretical quantities relevant for the forward model in diffuse light propagation are defined here

Photon distribution $N(\mathbf{r}, \hat{\mathbf{s}}, t)$ [$1/m^3 sr$]

is the number of photons per unit volume at a position \mathbf{r} , propagating in direction $\hat{\mathbf{s}}$ within a solid angle $d\omega$ at a specific time t .

Radiance $L(\mathbf{r}, \hat{\mathbf{s}}, t) = h\nu c N(\mathbf{r}, \hat{\mathbf{s}}, t)$ [$W/m^2 sr$]

is the power per steradian and per unit area where h is Planck's constant, ν is the frequency of the light and c is the speed of light in the medium.

Fluence rate $\Phi(\mathbf{r}, t) = \int_{4\pi} L(\mathbf{r}, \hat{\mathbf{s}}, t) d\omega$ [W/m^2]

is the power per unit area at a given time at a certain position. It is related to the photon density (ρ [$1/m^3$]) through $\Phi(\mathbf{r}, t) = h\nu c \rho(\mathbf{r}, t)$.

Photon flux $\mathbf{F}(\mathbf{r}, t) = \int_{4\pi} L(\mathbf{r}, \hat{\mathbf{s}}, t) \hat{\mathbf{s}} d\omega$ [W/m^2] is a vector quantity.

3.2 Radiative transport equation

The fundamental forward model for photon transport through diffuse media is the radiative transport equation (RTE) [121, 122]. It is an energy balance equation which is reached by considering a small volume V with boundary S and an outward pointing unit normal $\hat{\mathbf{n}}$. Let N be the photon distribution as defined in Section 3.1. According to the energy conservation principle, considered in a direction $\hat{\mathbf{s}}$, the net change must equal the difference between the inward and outward travelling photons. Within the volume photons are lost and gained through the processes depicted in Figure 3.3.

The net change of the photon distribution is given by

$$\int_V \frac{\partial N}{\partial t} dV = \dots$$

Photon gain

$$+ \underbrace{\int_V q dV}_i + \underbrace{\int_V c\mu_s \int_{4\pi} p(\hat{s}', \hat{s}) N d\omega'}_{ii} dV \dots$$

Photon loss

$$- \underbrace{\oint_S cN\hat{s}\hat{n}dS}_{iii} - \underbrace{\int_V c\mu_s N dV}_{iv} - \underbrace{\int_V c\mu_a N dV}_{v}$$

- i) Photon gain due to sources inside the volume where $q = q(\mathbf{r}, \hat{s}, t)$ [$1/sm^3sr$] is the number of photons emitted per unit volume, time and steradian.
- ii) Photon gain due to scattering from a propagation direction \hat{s}' to direction \hat{s} where $\mu_s = \mu_s(\mathbf{r})$ [$1/m$] is the scattering coefficient and $p(\hat{s}', \hat{s})$ is the scattering phase function.
- iii) Photon loss due to photons crossing the boundary. Here Gauss' theorem has been utilized so that the surface integral can be transferred to a volume integral according to $-\oint_S cN\hat{s}\hat{n}dS = -\int_V c\nabla N \cdot \hat{s}dV$.
- iv) Photon loss due to scattering.
- v) Photon loss due to absorption where $\mu_a = \mu_a(\mathbf{r})$ [$1/m$] is the absorption coefficient.

Replacing the photon distribution with the radiance and dropping the volume integral the radiative transport equation becomes

$$\frac{1}{c} \frac{\partial L}{\partial t} = h\nu q + \mu_s \int_{4\pi} p(\hat{s}', \hat{s}) L d\omega' - \hat{s} \cdot \nabla L - \mu_s L - \mu_a L. \quad (3.1)$$

The scattering phase function $p(\hat{s}', \hat{s})$ in ii) describes the probability for scattering in any direction. It is a function of the angle between the incoming propagation direction (\hat{s}') and the scattered propagation direction (\hat{s}). Hence $p(\hat{s}', \hat{s}) = p(\theta)$ where θ is the scattering angle. The simplest choice of $p(\theta)$ is the isotropic phase function, i.e.

$$p(\theta) = \frac{1}{4\pi}. \quad (3.2)$$

Photons affected by a scattering phase function of the form in Equation (3.2) will have equal probability to scatter in any direction. Biological tissues are forward scattering [123, 124]. Hence

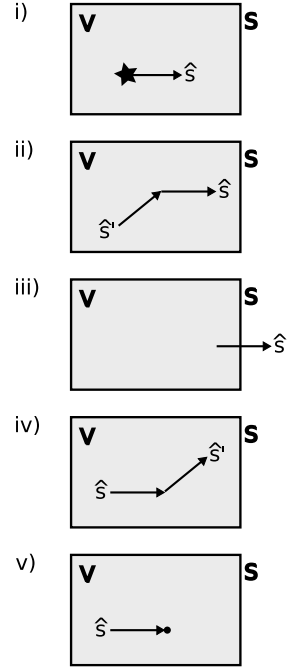


Figure 3.3. Processes in radiative transport equation.

the scattering phase function should adopt another form. There exist several alternatives but the most commonly applied is the Heyney-Greenstein phase function [125].

$$p(\theta) = \frac{1}{4\pi} \frac{1 - g^2}{(1 + g^2 - 2g \cos(\theta))^{3/2}}. \quad (3.3)$$

In Equation (3.3) the scattering anisotropy factor is defined through $g = \langle \cos \theta \rangle$, meaning the average of the cosine of the scattering angle. Solving the RTE implies finding the radiance in every location as well as every direction of an arbitrary object. Due to limited computational power simplifications to the RTE are needed.

3.3 Diffusion equation

An ever present forward model in diffuse optical imaging and therapeutics is the diffusion approximation to the RTE, i.e. diffusion equation (DE) [121, 122, 126]. In order to reach the DE, the approach is normally to expand the radiance, source term, and phase function into infinite series of spherical harmonics. The series are inserted into Equation (3.1) resulting in an infinite set of coupled equations. In the first order approximation, referred to as the P_1 -approximation, the spherical harmonics are truncated at the first degree [127–130]. Utilizing the fluence rate Φ and flux \mathbf{F} , see Section 3.1 the first order approximation of the radiance is expressed by

$$L(\mathbf{r}, \hat{\mathbf{s}}, t) \approx \frac{1}{4\pi} \Phi(\mathbf{r}, t) + \frac{3}{4\pi} \mathbf{F}(\mathbf{r}, t) \cdot \hat{\mathbf{s}}. \quad (3.4)$$

The first term on the RHS in Equation (3.4) is isotropic and the second term is linearly anisotropic. The P_1 -approximation implies that the light is treated as diffuse hence it cannot describe directed light. Inserting Equation (3.4) into the RTE results in two coupled equations

$$\left(\frac{1}{c} \frac{\partial}{\partial t} + \mu_a \right) \Phi + \nabla \mathbf{F} = q_0, \quad (3.5)$$

$$\left(\frac{1}{c} \frac{\partial}{\partial t} + \mu_a + \mu'_s \right) \mathbf{F} + \frac{1}{3} \nabla \Phi = \mathbf{q}_1. \quad (3.6)$$

In Equation (3.6) the reduced scattering coefficient $\mu'_s = (1 - g)\mu_s$ is introduced. Two assumptions are now made.

- (i) the linearly anisotropic source term $\mathbf{q}_1 = 0$ meaning that only isotropic sources exist.

- (ii) the temporal change of the flux is assumed to be negligible, i.e. $\partial \mathbf{F} / \partial t = 0$.

For these two assumptions to hold the following condition must be satisfied

$$\mu'_s \gg \mu_a. \quad (3.7)$$

With the two assumptions stated above, Equation (3.6) reduces to Fick's law

$$\mathbf{F} = -\frac{1}{3(\mu_a + \mu'_s)} \nabla \Phi = -D \nabla \Phi \quad (3.8)$$

where D is the diffusion coefficient. Inserting Equation (3.8) into Equation (3.5) yields the diffusion equation

$$\frac{1}{c} \frac{\partial \Phi(\mathbf{r}, t)}{\partial t} - \nabla D(\mathbf{r}) \nabla \Phi(\mathbf{r}, t) + \mu_a(\mathbf{r}) \Phi(\mathbf{r}, t) = q_0(\mathbf{r}, t). \quad (3.9)$$

The DE in frequency-domain can be retrieved through a Fourier transform of Equation (3.9) [131]. The steady-state DE is given by

$$-\nabla D(\mathbf{r}) \nabla \Phi(\mathbf{r}) + \mu_a(\mathbf{r}) \Phi(\mathbf{r}) = q_0(\mathbf{r}). \quad (3.10)$$

3.3.1 Boundary conditions

Boundary conditions are a requirement for retrieving unique solutions to the RTE or the DE. The boundary condition should describe the fact that photons leaving the medium never return. In addition photons propagating in the medium, bounded by S , are reflected on the boundary if the medium refractive index (n) and the outside refractive index (n_0) are mismatched. The reflectivity $R(\theta)$ is given by Fresnel's law [132], i.e.

$$R(\theta) = \frac{1}{2} \left(\frac{n \cos \theta' - n_0 \cos \theta}{n \cos \theta' + n_0 \cos \theta} \right)^2 + \frac{1}{2} \left(\frac{n \cos \theta - n_0 \cos \theta'}{n \cos \theta + n_0 \cos \theta'} \right)^2 \quad (3.11)$$

θ and θ' denote the incidence and refraction angle respectively, see Figure 3.4. The refraction angle is given by Snell's law and defined relative the surface normal. The RTE boundary condition for an index-mismatched boundary is given by [133]

$$L(\mathbf{r}, \hat{\mathbf{s}}', t) = R(\theta) L(\mathbf{r}, \hat{\mathbf{s}}, t). \quad (3.12)$$

Here $\hat{\mathbf{s}}$ is pointing outwards, i.e. $\hat{\mathbf{s}} \cdot \hat{\mathbf{n}} > 0$, while $\hat{\mathbf{s}}' \cdot \hat{\mathbf{n}} < 0$. Due to the approximate representation of the radiance, stated in Equation (3.4), the RTE boundary condition in Equation (3.12) can not be described exactly within the DE [121, 126]. This is inherited from the truncation of the spherical harmonics. Instead the

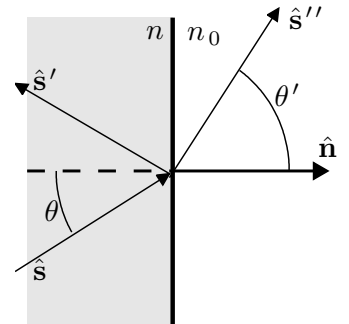


Figure 3.4. The incidence and refraction angles defined relative the medium boundary.

total inward (or outward) flux is adopted. The general boundary condition for the DE is then

$$\int_{\hat{\mathbf{s}}' \cdot \hat{\mathbf{n}} < 0} \hat{\mathbf{s}}' \cdot \hat{\mathbf{n}} L(\mathbf{r}, \hat{\mathbf{s}}', t) d\omega' = \int_{\hat{\mathbf{s}} \cdot \hat{\mathbf{n}} > 0} R(\theta) \hat{\mathbf{s}} \cdot \hat{\mathbf{n}} L(\mathbf{r}, \hat{\mathbf{s}}, t) d\omega, \quad \mathbf{r} \in S. \quad (3.13)$$

Integrating over the hemispheres after insertion of Equation (3.4) and Equation (3.8) yields the modified Robin-type boundary condition (RBC)

$$\Phi(\mathbf{r}, t) + 2AD\nabla\Phi(\mathbf{r}, t) \cdot \hat{\mathbf{n}} = 0, \quad \mathbf{r} \in S. \quad (3.14)$$

The parameter A takes the refractive index mismatch at the boundary into account. Utilizing Fresnel's law in Equation (3.11) A can be approximated through [132]

$$A = \frac{2/(1 - R_0) - 1 + |\cos\theta_c|^3}{1 - |\cos\theta_c|^2}, \quad (3.15)$$

$$R_0 = \frac{(n - n_0)^2}{(n + n_0)^2} \quad (3.16)$$

$$\theta_c = \arcsin\left(\frac{n_0}{n}\right). \quad (3.17)$$

Calculation of A for a tissue-air interface with $n = 1.4$ and $n_0 = 1$ yields $A \approx 2.74$. At an index-matched boundary $R_0 = 0$, $\cos\theta_c = 0$ and $A = 1$. In Section 3.4 the specific solution methods will be presented together with relevant implementation of the boundary conditions.

3.3.2 Source representation

Light irradiating the boundary, or light emitted from a fiber, can be modelled as an isotropic point source placed at one reduced scattering length from the actual source [134]. This approach is motivated by the assumption that all photons are scattered at the depth $d = 1/\mu'_s$ [134]. If the photon distribution is computed some distance from the incidence position this source representation produce valid results. Close to the source and in highly forward scattering media (large g -value) this approach will render erroneous photon distribution. Another alternative to represent a light source incident on the boundary is to modify the boundary condition in Equation (3.14) [127]. The boundary source is then

$$\Phi(\mathbf{r}, t) + 2AD\nabla\Phi(\mathbf{r}, t) \cdot \hat{\mathbf{n}} = -P_{src}w(\mathbf{r}, t), \quad \mathbf{r} \in S_{src} \quad (3.18)$$

where P_{src} is the source strength and $w(\mathbf{r}, t)$ is a weighting function describing the source shape.

3.3.3 Measurement representation

The photons that escape the medium through the surface is referred to as the exitance, denoted Γ . Formally the exitance is defined through a measurement operator that transform the internal fluence rate to boundary exitance, i.e.

$$\Gamma = \mathcal{M}[\Phi]. \quad (3.19)$$

The measurement operator is dependent on the boundary conditions, and detector model applied. When an optical fiber collects the photons, the exitance constitute all outward travelling photons within the aperture of the fiber. The aperture is given by the cross-sectional area (S_f) of the fiber tip and its numerical aperture (NA). With the acceptance angle defined by $\theta_f = \sin^{-1}(\text{NA}/n)$, the exitance is given by

$$\Gamma = \int_{S_f} \int_{\hat{\mathbf{s}} \cdot \hat{\mathbf{n}} > \cos \theta_f} T(\theta) L(\mathbf{r}, \hat{\mathbf{s}}, t) \hat{\mathbf{s}} \hat{\mathbf{n}} d\omega dS. \quad (3.20)$$

$T(\theta) = 1 - R(\theta)$ is the transmission through the boundary. The corresponding expression for the DE is retrieved by inserting the radiance approximation, see Equation (3.4), into Equation (3.20). Carrying out the integration for an index-mismatched boundary where $n = 1.4$, $n_0 = 1$ and $\theta_f = \pi/2$ the exitance becomes [135, 136]

$$\Gamma = S_f (0.118\Phi(\mathbf{r}, t) - 0.306D\nabla\Phi(\mathbf{r}, t)\hat{\mathbf{n}}). \quad (3.21)$$

In the case of an index-matched boundary, typically the case for an interstitially placed optical fiber, $T(\theta) = 1$ and the integral becomes

$$\Gamma = S_f \left(\frac{\sin^2 \theta_f}{4} \Phi(\mathbf{r}, t) - D\nabla\Phi(\mathbf{r}, t)\hat{\mathbf{n}} \frac{1 - \cos^3 \theta_f}{4} \right). \quad (3.22)$$

In addition to the expressions above approaches where the photon flux alone defines the exitance have been reported [137]. In that case the corresponding exitance to Equation (3.21) is given by $\Gamma = 0.170\Phi(\mathbf{r}, t)$ [136]. This might seem to be contradictory but inserting the Robin-type boundary condition for the DE into Equation (3.21) the exitance reduces to $\Gamma = 0.173\Phi(\mathbf{r}, t)$. The final remark concerning the measurement representation is that the exitance is directly proportional to the fluence rate when applying the Robin-type boundary condition. For future reference this imply that $\Gamma = \mathcal{M}[\Phi] = C\Phi$.

3.3.4 Diffusion equation considerations

There are several considerations that need to be addressed when applying the DE to describe diffuse light propagation. The main concerns are discussed here.

Optical properties

The DE is valid when the optical properties satisfy Equation (3.7), i.e. the scattering should be much larger than the absorption. The exact limit where validity of the DE breaks down is not explicitly stated since it is influenced by many factors such as the definition of diffusion coefficient, boundary conditions and source representation. The diffusion coefficient was introduced in Equation (3.8) where it depends on both the absorption and reduced scattering coefficient. It has been argued that the diffusion coefficient should be independent of the absorption coefficient. This conclusion is reached after assuming the flux to have an exponentially decaying term, i.e. $\mathbf{F} \sim \exp(-cat)$ [129]. This discussion leads to another definition of the diffusion coefficient, i.e.

$$D = \frac{1}{3(\alpha\mu_a + \mu'_s)}, \quad \alpha \in [0, 1]. \quad (3.23)$$

The validity of DE has been reported to extend into highly absorbing media, for steady-state measurements, when $\alpha \in [0, 0.5]$ [130, 138, 139]. The general approach within this thesis is to implement the diffusion coefficient as stated in Equation (3.8).

Although the validity of the DE might be extended by modifying the diffusion coefficient in steady-state analysis the same is not true for time-resolved analysis, employing the DE. The limited validity for the time-resolved DE is due to the assumption that the flux does not vary in time. For short times this assumption is erroneous. A better approach is then to utilize the RTE if applicable [140].

Boundary conditions

As stated in Section 3.3 the DE cannot accurately describe the boundary condition in Equation (3.12). Instead of the angular resolved radiance the total radiance, approximated with Equation (3.4) within a hemisphere is treated leading to the Robin-type boundary condition. Since this boundary condition relies on an approximation the influence of the boundary condition is an important factor. In small geometries the influence of the boundaries is large leading to limited validity of the DE.

Source representation

The isotropic source representation leads to a non-valid light distribution close to the source. The analysis of light propagation utilizing the DE should be performed at distances longer than a few reduced mean free paths, i.e. $> 3 - 5 \text{ mfp}'$ where $\text{mfp}' = 1/(\mu_a + \mu'_s)$ [141, 142].

Higher order approximations

The DE is the first order approximation to the RTE and higher order approximations of course exist. Since extensive computational power is more easily accessible today many research groups are investigating the use of spherical harmonics expansion to higher degrees [143, 144]. Essentially this renders a problem consisting of multiple coupled differential equations, instead of two as is the case in the P_1 -approximation. In addition to the higher approximations numerical schemes to solve the RTE have appeared in recent years [145, 146].

The non-validity of the DE close to sources can be avoided employing hybrid models. In this approach the RTE is solved close to sources, boundaries as well as high absorbing media whereas the DE is solved in regions where the diffusion approximation holds [147]. The coupling between the DE and RTE is typically realized through a boundary condition between the RTE-region and DE-region [148, 149].

3.4 Solving the forward problem

Despite the considerations that needs to be taken into account, the DE can produce valid results. Hence it is utilized extensively in diffuse optical imaging and dosimetry. The main reason is the versatility since solution schemes allows simulations to be performed in arbitrary volumes with limited computational requirements. In this section three approaches to solve the forward problem will be discussed. In Section 3.4.1 the Monte Carlo method for stochastic modelling of the RTE is briefly discussed. In Section 3.4.2 and Appendix A the Finite Element Method for solving the DE is introduced. Analytical solutions to the diffusion equation exist in simple cases and these are summarized in Section 3.4.3.

3.4.1 Monte Carlo model for the RTE

In the Monte Carlo (MC) method the processes that can occur within the RTE, see Figure 3.3, are treated as stochastic processes. A flowchart depicting the main components of a Monte Carlo scheme is shown in Figure 3.5. Practically the photons are treated as photon packages with an initial weight. When launched into the scattering medium the propagation direction is sampled from a distribution given by the scattering phase function. The photon is then moved a step with length given by $s = -\ln(\xi)/(\mu_a + \mu_s)$, where ξ is a uniformly distributed random variable. After the move the weight is decreased by a fraction whereas the left-over is logged as absorption. This process continues until the photon escapes a boundary or the weight is too small. When the latter occurs either the photon package is terminated or it is given a

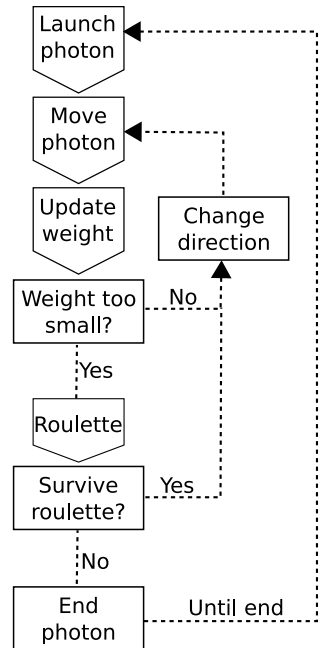


Figure 3.5. Monte Carlo simulation flowchart.

certain probability to survive. If the photon survives, the weight is increased and the propagation continues [150]. Monte Carlo methods for light propagation simulation in simple geometries that exploit symmetries are widely available [150–153]. Monte Carlo schemes for three-dimensional heterogeneous media has also been implemented [154]. The main limitation of MC methods is the long computational time due to the high number of photon packages that need to be simulated. In recent years schemes based on parallel computing have shown decreased computational time with the use of graphics card [155, 156].

3.4.2 Finite Element Method for the DE

The Finite Element Method (FEM) is extensively applied to engineering problems of varying art. The method originates from the field of structural mechanics in the mid 1950s [157] but the potential was rapidly appreciated in problems such as heat conduction, fluid mechanics and electromagnetism [158]. Within the scope of diffuse light propagation the FEM is utilized to render a solution to the DE. The procedure of reaching the FEM formulation is detailed in Appendix A. The main aspect is that the DE is discretized into a number of elements, described by a mesh. Since the elements are small the fluence rate is taken to vary linearly over each element. This fact renders a linear equation system described by the matrix equation in Equation (3.24),

$$\left[\mathbf{K}(D) + \mathbf{C}(\mu_a) + \frac{1}{2A} \mathbf{F} \right] \Phi = \mathbf{A} \Phi = \mathbf{Q}. \quad (3.24)$$

Equation (3.24) is solved for each nodal value of the fluence rate. A key feature of the FEM is that the method can be applied to heterogeneous media as well as arbitrary geometries. Several FEM packages exist in order to solve the DE for light propagation in diffuse media. Comsol Multiphysics [159] was utilized in Paper **VI** for simulation the treatment light propagating in a human prostate. It has also been adopted in Paper **VIII** for meshing a geometry simulating the human prostate. Two other packages more focused on sole light propagation modelling exist, namely TOAST [127, 160, 161] and NIRFAST [142, 162]. These packages solve the forward problem with FEM but in addition the inverse problem, see Chapter 4, can be solved. TOAST was exploited and modified for multispectral three-dimensional fluorescence imaging in Paper **II**. NIRFAST was adapted for interstitial FEM simulation in Paper **VIII** and non-linear three-dimensional fluorophore imaging in Paper **IV**.

3.4.3 Analytical solutions for the DE

Numerical methods, such as the FEM, provide versatile means to render a solution to the DE. Since the FEM utilizes a discretized geometry large volumes will lead to a mesh with high nodal density. When such problems are to be analyzed the available computer memory can impose a limit to the mesh size. One alternative to overcome this discrepancy is presented in Paper **II** but in simple geometries analytical solutions exist.

Infinite homogeneous medium

Consider a source, positioned at \mathbf{r}_s in an infinite homogeneous medium. The source delivers a power of P_0 [W] hence the source term is given by $q_0 = P_0\delta(\mathbf{r} - \mathbf{r}_s)$. The steady-state DE, see Equation (3.10), reduces to a Helmholtz equation,

$$\left[-\nabla^2 + \frac{\mu_a}{D}\right]\Phi(\mathbf{r}) = \frac{P_0}{D}\delta(\mathbf{r} - \mathbf{r}_s). \quad (3.25)$$

A solution to Equation (3.25) is the Green's function [126, 141, 163–165] given by

$$\Phi(\mathbf{r}_s, \mathbf{r}) = P_0\tilde{g}(\mathbf{r}_s, \mathbf{r}) = P_0\frac{\exp(-\mu_{\text{eff}}|\mathbf{r} - \mathbf{r}_s|)}{4\pi D|\mathbf{r} - \mathbf{r}_s|}. \quad (3.26)$$

Here μ_{eff} [1/m] is called the effective attenuation coefficient and defined through

$$\mu_{\text{eff}} = \sqrt{\frac{\mu_a}{D}}. \quad (3.27)$$

Equation (3.26) was utilized in Paper **VI** to model light delivered by a bare-end optical fiber. The Green's function for the time resolved DE is given by [134].

$$\Phi(\mathbf{r}_s, \mathbf{r}, t) = c(4\pi Dct)^{-3/2}\exp\left(-\frac{|\mathbf{r} - \mathbf{r}_s|^2}{4\pi Dct} - \mu_a ct\right). \quad (3.28)$$

A corresponding Green's function for the frequency-domain DE exist [131].

Semi-infinite and slab-shaped homogeneous media

When a boundary is introduced Equation (3.26) needs to be modified in order to account for the reflection at the boundary. Consider a light source positioned at the physical surface of the semi-infinite medium. As above the source is simulated by placing an isotropic source at a depth $z_0^+ = 1/\mu'_s$. At an index-matched boundary no photon current is allowed back into the medium. In the case of an index-mismatched boundary the only inward directed current

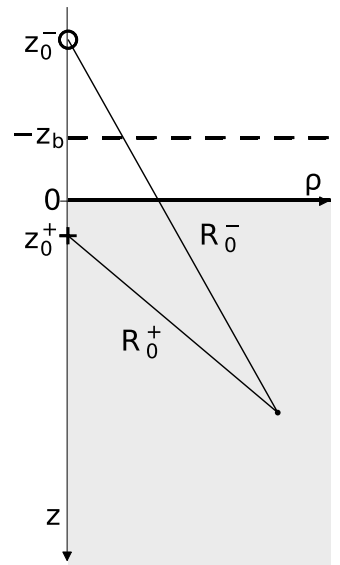


Figure 3.6. Positive (+) and negative (-) source configuration in a semi-infinite homogeneous medium.

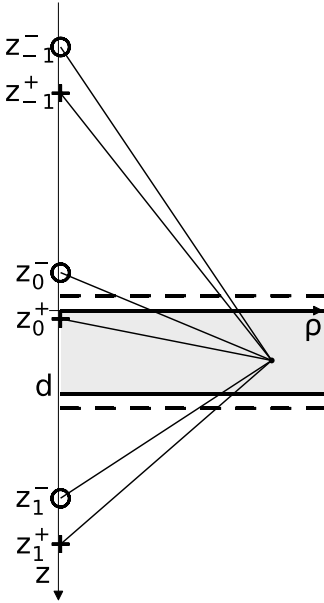


Figure 3.7. Positive (+) and negative (-) source configuration in a homogeneous slab.

is due to the reflection at the boundary. This boundary condition can approximately be described by placing a source with negative strength at a distance $z_0^- = -2z_b - z_0^+$ where $z_b = 2AD$. This is called the extrapolated boundary condition (EBC) since practically it renders a virtual boundary at $z = z_b$ where the fluence rate is zero, Figure 3.6 [141]. The fluence rate is given by the sum of the two isotropic sources, i.e.

$$\Phi(\mathbf{r}) = \frac{P}{4\pi D} \left(\frac{\exp(-\mu_{\text{eff}} R_0^+)}{R_0^+} - \frac{\exp(-\mu_{\text{eff}} R_0^-)}{R_0^-} \right) \quad (3.29)$$

where $R_0^{+,-} = \sqrt{\rho^2 + (z - z_0^{+,-})^2}$, indicated in Figure 3.6.

In the case of two boundaries, also called an infinite slab, the boundary condition should be satisfied at both interfaces. The procedure is the same as above but instead of two sources an infinite sum of sources is retrieved [134]. The z -position of a source with index m in the series can be expressed by [166]

$$\begin{aligned} z_m^{(+)} &= 2m(d + 2z_b) + z_0^{(+)} \\ z_m^{(-)} &= 2m(d + 2z_b) - 2z_b - z_0^{(+)} \\ m &= 0, \pm 1, \pm 2, \pm 3, \dots \end{aligned} \quad (3.30)$$

Figure 3.7 depicts the positive and negative sources for $m = 0, \pm 1$. The fluence rate at any point within the slab now becomes

$$\Phi(\mathbf{r}) = \frac{P}{4\pi D} \sum_{m=-\infty}^{m=+\infty} \frac{\exp(-\mu_{\text{eff}} R_m^+)}{R_m^+} - \frac{\exp(-\mu_{\text{eff}} R_m^-)}{R_m^-}. \quad (3.31)$$

As above the distance is given by $R_m^{+,-} = \sqrt{\rho^2 + (z - z_m^{+,-})^2}$. Equation (3.31) was used in Paper I when modelling the light within a slab due to a laser beam irradiating the surface within a small spot.

3.5 Fluorescence diffusion equation

The forward models described above can be extended to fluorescence light propagation. Consider a fluorophore within a volume V of infinitesimal volume δV at a position \mathbf{r} . The excitation light at this position is denoted $\Phi_x(\mathbf{r})$. As described in Section 2.3 the coupling between excitation and emission light is governed by the fluorescent yield, i.e. $\eta = \gamma \times \mu_{\text{af}}$, where μ_{af} is the fluorophore absorption coefficient at the excitation wavelength. Since the fluorophore is small and finite it can be treated as a point source denoted $q_m(\mathbf{r}) = \gamma \mu_{\text{af}}(\mathbf{r}) \Phi_x(\mathbf{r})$ [153, 167]. The fluorescence forward model is then given by two coupled equations; one for the excitation light and one for the emission light, as schematically

depicted in Figure 3.8. Adopting the steady-state DE the fluorescence forward model becomes [40, 168–170]

$$[-\nabla D_x(\mathbf{r})\nabla + \mu_{ax}(\mathbf{r})]\Phi_x(\mathbf{r}) = q_0(\mathbf{r}), \quad (3.32)$$

$$[-\nabla D_m(\mathbf{r})\nabla + \mu_{am}(\mathbf{r})]\Phi_m(\mathbf{r}) = \Phi_x(\mathbf{r})\gamma\mu_{af}(\mathbf{r}). \quad (3.33)$$

Here x and m denotes excitation and emission respectively. Equations (3.32) and (3.33) omits any temporal characteristics since they describe fluorescence propagation induced by a continuous light source. Conversely when a short light-pulse governs the excitation, at time t , the fluorescence lifetime will induce a temporal lag before the emission photon is generated, at time t' . In order to retrieve a time-resolved fluorescence forward model the steady-state DE is replaced with the time-domain analogue, i.e. Equation (3.9). Assuming a mono-exponential decay the fluorescence point source for time-resolved fluorescence can be defined as [168–170]

$$q_m(r, t) = \frac{\gamma\mu_{af}}{\tau} \int_0^t \exp\left(\frac{-(t-t')}{\tau}\right) \Phi(r, t') dt'. \quad (3.34)$$

Correspondingly in frequency-domain the fluorescent point source is defined through [40, 142, 168, 170]

$$q_m(\mathbf{r}, \omega) = \Phi_x(\mathbf{r}, \omega)\gamma\mu_{af}(\mathbf{r}) \frac{1 - i\omega\tau(\mathbf{r})}{1 + \omega^2\tau(\mathbf{r})^2}. \quad (3.35)$$

The solution of the fluorescence forward model is typically retrieved through a two-step FEM-solution. Throughout this thesis the steady-state fluorescence model will be considered while it is solved adapting a frequency-domain FEM-solver with frequency $\omega = 0$.

Analytical schemes exist when the bulk optical properties, i.e. μ_a and μ'_s , are homogeneous. In order to satisfy homogeneity the condition $\mu_{af} \ll \mu_a$ should hold. In essence this means that the fluorophore absorption coefficient must be so small that it does not perturb the excitation field. With notation according to Figure 3.8 the fluorescence fluence rate is given by [168, 171]

$$\Phi_m(\mathbf{r}_s, \mathbf{r}_d) = \int_V \Phi_x(\mathbf{r}_s, \mathbf{r})\gamma\mu_{af}(\mathbf{r})\tilde{g}_m(\mathbf{r}, \mathbf{r}_d)\delta V \quad (3.36)$$

Φ_x and \tilde{g}_m is the excitation fluence rate and fluorescence escape function respectively and can be identified in Equation (3.26). The spatial extent of the fluorophore causes implications for retrieval of explicit solutions to Equation (3.36). Assuming a homogeneous

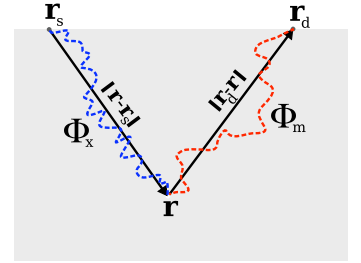


Figure 3.8. Schematic of the photon migration of excitation light and fluorescence light.

distribution, i.e. $\mu_{\text{af}}(\mathbf{r}) = \mu_{\text{af}}$ the fluorescence at a radial distance $|\mathbf{r}_d - \mathbf{r}_s|$ from the source becomes [168, 172–174]

$$\Phi_m(\mathbf{r}_s, \mathbf{r}_d) = \frac{P_0 \gamma \mu_{\text{af}}}{4\pi D_x D_m} \frac{1}{|\mathbf{r}_d - \mathbf{r}_s|} \times \quad (3.37)$$

$$\dots \left(\frac{\exp(-\mu_{\text{eff},m} |\mathbf{r}_d - \mathbf{r}_s|)}{(\mu_{\text{eff},x}^2 - \mu_{\text{eff},m}^2)} - \frac{\exp(-\mu_{\text{eff},x} |\mathbf{r}_d - \mathbf{r}_s|)}{(\mu_{\text{eff},x}^2 - \mu_{\text{eff},m}^2)} \right).$$

Here Φ_x and \tilde{g}_m from Equation (3.26) has been inserted explicitly into Equation (3.36). In addition to the homogeneous case above several simplifying models have been presented where the inclusion is taken to be spherical [172] or layered [175, 176]. Since these models are somewhat restricted to special cases the common way for arbitrary fluorophore shapes, if not FEM, is to discretize Equation (3.36) and calculate the fluorescence photon propagation through a matrix multiplication [171].

The discussion above adapts the DE in order to solve for the fluorescence photon migration. The RTE, and higher order approximations of the same, are also applicable to fluorescence. In the same way as the coupled DE:s were formed, coupled RTE:s can be implemented although with a substantial increase in computational cost [144, 177, 178]. Another approach is to utilize the Monte Carlo method given that symmetry can be exploited, e.g. cylindrical symmetry [167].

3.6 Reciprocity theorem

An important principle within diffuse optical modelling is the *reciprocity theorem* [126, 153]. With notation from Figure 3.8, reciprocity means that the fluence rate at a detector location \mathbf{r}_d due to a source in \mathbf{r} is identical to the case when the source and detector positions are switched. An example where this fact can be employed is in Monte Carlo simulations of fluorescence exitance. Here the fluorescence light is simulated as it originated from the surface instead of the true location within the medium. With a corresponding, normal, excitation light simulation the fluorescence exiting the boundary can be retrieved by convolution of the two photon distributions, incorporating some additional scaling factors [153, 179]. Another example is the effective calculation of the system matrix used for diffuse optical tomography as will be further explored in Chapters 4, 5 and 6.

ESTIMATING TISSUE PROPERTIES

The essence of medical imaging of scattering media, employing visible and near infrared light, is the quantification of optical properties. As discussed in Chapter 2 these properties can reflect the tissue condition providing means for disease diagnosis. In this chapter the methodologies for estimating tissue optical properties are introduced. The discussion herein is confined to schemes and techniques with the purpose to assess optical properties in a reasonably large medium. This accommodate the use of any of the forward models discussed in Chapter 3.

The contents of present chapter is given by Figure 4.1.

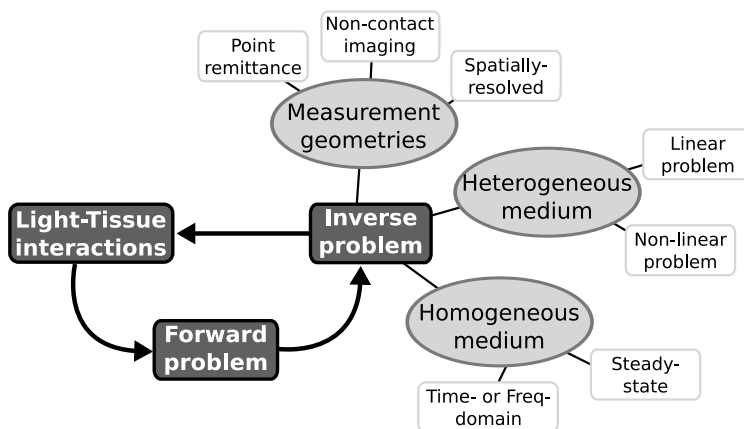


Figure 4.1. Graphical representation of the contents of present chapter.

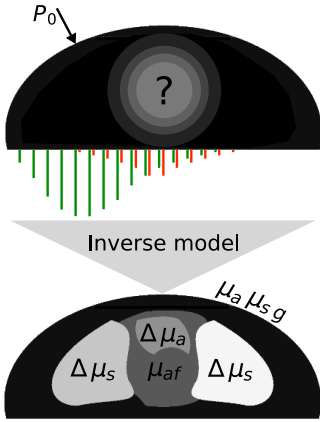


Figure 4.2. The inverse problem.

4.1 The inverse problem

A measurement of the light exiting the boundary of a scattering object can reflect the attributes of the properties throughout the medium. The *inverse problem* constitutes the procedure where these attributes are sought given a set of exitance measurements. The *inverse model* then constitutes the mathematical formalism of the problem at hand, see Figure 4.2. Within the scope of this thesis model-based inversion schemes are considered. Essentially this means that the problem is to find the optical properties where the residual between the measurements and the forward model is minimized.

The measurements, or any transformation of the same, are described by the *measurable*¹, denoted \mathbf{y} . The forward model is given by

$$G(\mathbf{x}) = \mathcal{M}[\Phi(\mathbf{x})] \quad (4.1)$$

where the measurement operator, \mathcal{M} , is dependent on the detector model as discussed in Section 3.3.3. The vector \mathbf{x} represents the unknown tissue property that is sought, e.g. μ_a , D or η .

Within the least squares framework the objective function to minimize is given by²

$$\Omega = \|\mathbf{y} - G(\mathbf{x})\|^2. \quad (4.2)$$

A solution is retrieved by finding the optimal \mathbf{x} where Equation (4.2) is minimized.

4.2 Measurement geometries

The light escaping the boundary of a medium can be collected in several ways. In Figure 4.3 the general geometries are summarized. Here *remittance* refers to light that have propagated inside the medium and returns on the same side as the incident light source. Conversely the *transmittance* travels through the tissue and escapes on any opposing side relative the source. Omitted in Figure 4.3 is the *specular reflectance*, i.e. direct reflection of the incident light on the boundary, since this light macroscopically never enters the medium.

a) Point remittance

With a single fiber, or fiber-bundle, the aim is to assess the tissue properties within a small volume beneath the fiber-tip. Typical

¹In Chapter 3 the exitance, i.e. the measured intensity, was defined by Γ . The measurable is introduced in order to generalize the formal treatment.

²The Euclidean norm, i.e. $\|\mathbf{y} - G(\mathbf{x})\|^2 = \sum_{i=1}^M [y_i - G(\mathbf{x})]^2$ where M is the number of measurements.

applications are within endoscopic investigations where the optical measurement acts as guidance for e.g. a biopsy [43, 180]. Due to the small distances involved (light is delivered and collected by essentially the same fiber) detailed analysis of the probed volume is required [181]. Here Monte Carlo methods form the gold-standard [182–184]. Studies trying to limit the need for forward modelling exist. One example is the scattering-independent geometry where the measurement is effectively insensitive to the tissue scattering properties if the source and detector is placed at a certain distance [185]. Conversely there exist techniques trying to utilize the elastic scattering for tissue diagnostics [24]. Fluorescence point spectroscopy can also be adapted to the point remittance geometry. For instance in applications where atherosclerotic plaques [42, 186] or cancerous tissues [187, 188] are to be diagnosed.

b-d) Spatially resolved remittance/transmittance

When assessing larger tissue volumes the optical fibers need to be separated in space [141]. Dependent on the source-detector distances proper forward models can be exploited for evaluation of the measurement signals. In particular the DE can be adopted if the measurements are acquired far from the source within a medium of sufficiently high scattering, see Chapter 3 [173, 175]. The mathematical aspects will be further discussed in Section 4.3.

e-f) Non-contact remittance/transmittance

A valuable tool in diffuse optical imaging is non-contact measurements. Using e.g. a CCD-camera an image of the region-of-interest is retrieved where every pixel can be treated as a small detector. Normally spectral filters are employed so that images in different spectral bands can be collected [189–193]. The ample amount of data available can be used for spectral image processing where delineation of malignant tissue is the problem at hand [194, 195]. The result of such a survey is a contrast image where spectral anomalies are visualized. Employing a forward model to describe the image contrast provide means for rendering images of the interior distribution of e.g. a fluorophore. This will be rigorously discussed in Section 4.4.

4.3 Homogeneous optical properties

When the spatial extent of the optical properties is neglected the medium is defined as homogeneous. This approximation is useful in numerous occasions. Measurement geometries such as those shown in Figure 4.3a-d are typically applied. All of the schemes de-

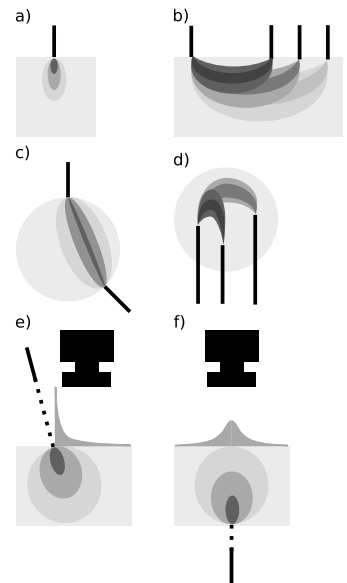


Figure 4.3. a) Point remittance, b) Spatially resolved remittance, c) Spatially resolved transmittance, d) Interstitial spatially resolved transmittance, e) Non-contact remittance, f) Non-contact transmittance.

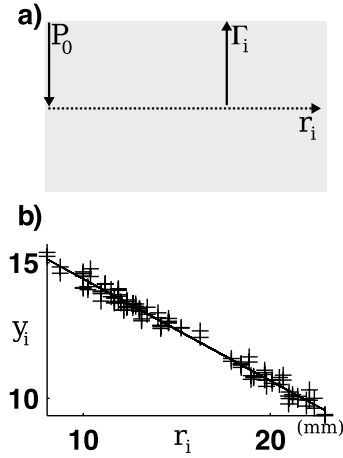


Figure 4.4. a) Spatially resolved measurement geometry, b) Experimental data (+) and the LLS fit (-).

scribed below can easily be extended to multispectral analysis thus motivating the family name diffuse optical spectroscopy (DOS).

4.3.1 Spatially resolved spectroscopy

Consider a case where the absorption and reduced scattering coefficients are to be evaluated using spatially resolved spectroscopy. The measurement setup seen in Figure 4.4a, can be employed where an interstitially placed source fiber delivers a constant and continuous power P_0 into the tissue. The exitance is dependent on the radial distance from the source as described by the Green's function to the DE, see Equation (3.26). This fact can be exploited in order to assess the optical attenuation of the medium. The exitance measured at source-detector distance r_i is given by Γ_i . M spatially-resolved measurements are performed whereas the analytical Green's function is adopted as the forward model.

The measurement operator is here assumed to impose a calibration constant on the measurements, so that $G(\mathbf{x}) = C\Phi(\mathbf{r}_i)$. Since the Green's function is non-linear with respect to the sought parameters the transformation $y_i = \ln(r_i\Gamma_i)$ is useful to render a linear equation system of the form

$$\mathbf{y} = \begin{bmatrix} y_1 \\ y_2 \\ \vdots \\ y_M \end{bmatrix} = \begin{bmatrix} 1 & -r_1 \\ 1 & -r_2 \\ \vdots & \vdots \\ 1 & -r_M \end{bmatrix} \begin{bmatrix} x_1 \\ x_2 \end{bmatrix} = \mathbf{J}\mathbf{x} \quad (4.3)$$

where $x_1 = \ln\left(\frac{CP_0}{4\pi D}\right)$ and $x_2 = \mu_{\text{eff}}$ [131]. The solution that minimizes the residual between the forward model and the measurements, in the least squares sense, is given by the Linear Least Squares (LLS) normal equations [196]

$$\mathbf{J}^T \mathbf{J} \mathbf{x} = \mathbf{J}^T \mathbf{y}. \quad (4.4)$$

An example of the fit is shown in Figure 4.4b. The calibration constant C accounts for instrument dependent constants and includes factors such as collection efficiency and detection quantum yield. In addition, C transforms fluence rate to exitance as discussed in Section 3.3.3. If the calibration constant is explicitly known both D and μ_{eff} are retrieved from x_1 and x_2 . Subsequently μ_a and μ'_s can be calculated from μ_{eff} and D [197, 198]. Without absolute calibration only the effective attenuation coefficient is retrieved. Although the linear transformation adopted in Equation (4.3) is advantageous, non-linear least squares could be applied leading to an iterative scheme. This is a special case of the scheme to be described in Section 4.4. Spatially resolved steady-state measurements are easily implemented with relatively limited requirements on instrumentation.

4.3.2 Time- and frequency-domain spectroscopy

Conversely to the steady-state instrumentation more sophisticated measurement methods exist that utilize time-resolved or intensity-modulated optical signals. In time-domain the source attributes a short light pulse. When the burst of light travels through the tissue the photons are randomly scattered. When the photons reach the detector position they will have propagated different path-lengths through the medium. This means that a short pulse will be broadened in time as a result of the different times required to reach the detector for different photons. Collection of the photons at a certain distance from the source with e.g. photon-counting instrumentation yields a photon histogram similar to Figure 4.5a [134, 199, 200]. The inverse problem comprise the procedure to fit the measurements to a forward model. One alternative of forward model is to utilize the time-domain Green's function Equation (3.28) although higher accuracy has been reported when a Monte Carlo scheme is adopted [140, 199, 201]. An important feature of the time-resolved technique is that both μ_a and μ'_s can be separated, even at one fixed source-detector distance. This aspect arise from the fact that higher scattering will cause the photons to arrive later in time, meaning that the dispersion curve in Figure 4.5a is translated to the right (although with decreased exitance). The absorption imposes a different effect since it will change the asymptotic slope in logarithmic scale of the dispersion curve. This is also verified by the asymptotic behaviour of Equation (3.28) since its temporal dependence is $\sim \exp(-\mu_a ct)$.

The frequency-domain technique utilizes an intensity-modulated laser instead of a pulsed laser. When irradiating the tissue with sinusoidal varying source-power the light collected by the detector will also be sinusoidal although with a phase-shift (ϕ) due to the propagation through the tissue, see Figure 4.5b. In addition the amplitude is diminished relative the source amplitude, commonly referred to as demodulation. In Figure 4.5b the demodulation is calculated from the signal amplitude as $(c/d)/(a/b)$. The phase and amplitude is practically retrieved using frequency-mixing where an explicitly known signal is mixed with the detected signal in order to extract the phase difference and amplitude [202]. The frequency-domain technique also has the capability to separate absorption and scattering. The quest is to fit the phase lag and demodulation to e.g. the Green's function to the frequency-domain DE [131, 202]. Although one frequency is in theory enough for complete separation normally several frequencies are utilized within the range of 10-500 MHz.

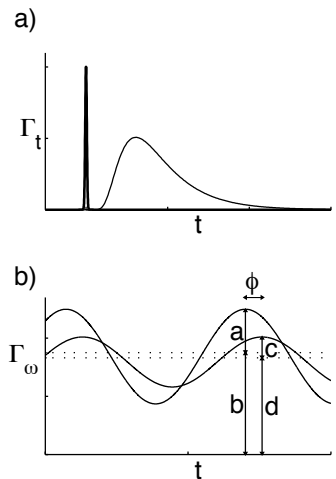


Figure 4.5. a) Time-resolved exitance (the source light pulse is shown for reference), b) Intensity-modulated exitance.

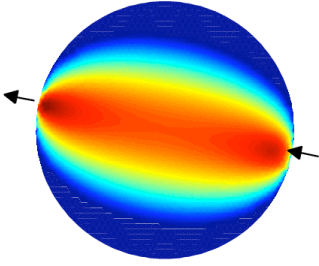


Figure 4.6. *The light propagation between a source and a detector, referred to as a projection. It can also be interpreted as a sensitivity map between source and detector where regions with high value (red) will affect the measurement to a higher extent.*

4.3.3 Fluorescence spectroscopy

In fluorescence spectroscopy one or several homogeneously distributed fluorophores are to be assessed. The typical approach is to apply a fiber optic probe [174, 176, 203]. When point-remittance geometries are employed the use of forward models can be avoided in the evaluation by adapting empirical schemes. Such approaches require calibration and probe configuration in order to quantify the fluorophore [204, 205]. Without pre-calibration only relative evaluation can be performed, as was done in Paper V. Another approach is to fit Monte Carlo simulations to the probe measurements [167]. For longer source-detector distances the DE can be applied. By fitting Equation (3.38) to the fluorescence, as well as reflectance measurements, the fluorophore concentration can be retrieved [172, 173]. The fluorescence from a homogeneous medium will mainly be induced close to the source. In high absorbing media, i.e. shorter excitation wavelengths, fluorescence can be treated as if it originated from a point source. At longer wavelengths the excitation light distribution might extend over a larger volume hence the spatial extent of the fluorophore must be incorporated.

4.4 Heterogeneous optical properties

The method to estimate heterogeneous optical properties is commonly referred to as diffuse optical tomography (DOT). Here a spatial map of the optical properties within the medium is sought. The medium is then discretized into a (large) number of voxels where the problem is to find the optical properties in every element. Evidently there is a similarity between X-ray computer tomography (CT) and DOT since both schemes render maps of the interior distribution of the imaging target. With this in mind the name diffuse optical tomography is motivated. On the other hand the techniques are completely different since X-rays propagates with little diffraction through the body owing to the high energy of the photons. Within the visible and the near infrared wavelengths regions the scattering imposes a limit to the achievable image quality. Another difference is the imaging contrast that in X-ray CT is produced by attenuation. As described in Chapter 2 the use of light present possibilities to choose the imaging target among absorbing chromophores, scattering structures as well as fluorophores. Due to the flexibility of imaging agent there exist a wide variety of applications. In Chapters 5 and 6 DOT with the aim to localize and quantify fluorophores will be further explored. Here the framework for reconstruction of the spatial distribution of the optical properties is given.

Consider a measurement setup consisting of several sources and detectors distributed over the surface, or in the interior, of an object. Each combination of one source and one detector is called

a *projection*, depicted in Figure 4.6. A total of M projections are acquired while the object domain is discretized into N voxels. Due to the scattering, light does not travel in a straight path between the source and detector but instead the whole volume is probed. Essentially this means that a small perturbation placed inside the object will affect all detected signals [206].

4.4.1 Perturbation approach

Let's assume that the initial optical properties, denoted \mathbf{x}_0 , give rise to the measurements $\mathbf{y}_0 = G(\mathbf{x}_0)$. A small perturbation $\Delta\mathbf{x}$ will alter the measurements and the new measurements are denoted \mathbf{y} . The perturbed solution is retrieved through a Taylor expansion of Equation (4.1) around \mathbf{x}_0 given by

$$\mathbf{y} = G(\mathbf{x}_0) + \frac{\partial G}{\partial \mathbf{x}}(\mathbf{x} - \mathbf{x}_0) + \dots \quad (4.5)$$

Defining $\Delta\mathbf{y} = \mathbf{y} - \mathbf{y}_0$, $\Delta\mathbf{x} = \mathbf{x} - \mathbf{x}_0$ in addition to the *Jacobian* matrix $\mathbf{J} = \frac{\partial G}{\partial \mathbf{x}}$, the perturbation can be retrieved by solving

$$\Delta\mathbf{y} = \mathbf{J}\Delta\mathbf{x}. \quad (4.6)$$

When applying Equation (4.6) to absolute intensity measurements the problem is commonly referred to as the *Born approximation* [207]. The perturbation approach can be adopted for example when hemodynamics are to be studied [208]. Typically two datasets are acquired; before and after a specific event has occurred. The relative change of the optical properties is then reconstructed. The main problem is that the optical properties in the initial state must be known. Initial efforts in DOT applied the perturbation approach due to solution methods adopted from X-ray CT can be applied. Typically Algebraic reconstruction technique (ART), and derivatives of the same, are used to invert Equation (4.6) [209, 210]. Due to the fundamental ill-posedness of the problem, as described above, perturbation models have limited applicability to general problems [211]. Instead a more general scheme can be adopted.

4.4.2 Formulation of the general problem

As stated earlier the high scattering within biological tissues causes the photons to propagate throughout the entire volume of the medium under study. This aspect renders the problem of finding the N unknowns to become an *ill-posed*³ problem [214]. In

³In general terms a problem is termed ill-posed if the solution is non-unique or if the solution is not a continuous function of the parameters. In practice non-uniqueness means that there exist not only one distribution of optical properties that yield the same exitance. Non-continuity on the other hand states that if a small perturbation of the data can cause a large perturbation of the solution [212, 213].

addition the number of unknowns typically exceeds the number of measurements making this an under-determined problem. A consequence of the ill-posedness and under-determination is that the inversion process, given by the minimization of Equation (4.2), is unstable. The common way to solve such problems is through *regularization*. Adapting Tikhonov regularization the objective function now becomes [215]

$$\Omega = \|\mathbf{y} - G(\mathbf{x})\|^2 + \lambda \|\mathbf{L}(\mathbf{x} - \mathbf{x}_0)\|^2. \quad (4.7)$$

Here λ is called regularization parameter, \mathbf{L} is a regularization matrix while \mathbf{x}_0 is an initial guess of the unknown parameter. Equation (4.7) constitutes a combination of two objective functions; one where the residual should be minimized and one where the solution norm should be minimized. The latter means that the solution should not fluctuate too much [213, 214]. The selection of λ and \mathbf{L} is intricate and will be further discussed in Sections 4.4.4 and 4.4.5. A general solution to Equation (4.7) can be formed as an iterative scheme where the solution \mathbf{x} is sequentially updated until convergence. The solution, detailed in Appendix B, is given by

$$\mathbf{x}_{k+1} = \mathbf{x}_k + [\mathbf{J}^T \mathbf{J} + \lambda \mathbf{L}^T \mathbf{L}]^{-1} [\mathbf{J}^T \Delta \mathbf{y}_k - \lambda \mathbf{L}^T \mathbf{L}(\mathbf{x}_k - \mathbf{x}_0)] \quad (4.8)$$

where $\Delta \mathbf{y} = \mathbf{y} - G(\mathbf{x}_k)$. A prerequisite for convergence is that the initial guess \mathbf{x}_0 is sufficiently close to the solution. This is in practice achieved by performing a homogeneous fit according to Section 4.3 prior to execution of the iteration scheme [216]. Equation (4.8) is applied whenever the forward model, $G(\mathbf{x})$, has non-linear dependence on the parameters, \mathbf{x} . Typically this is the case when the bulk optical properties, i.e. μ_a and μ'_s , are to be reconstructed.

A linear reconstruction scheme is retrieved when aborting the iteration in Equation (4.8) after one iteration, so that

$$\Delta \mathbf{x} = [\mathbf{J}^T \mathbf{J} + \lambda \mathbf{L}^T \mathbf{L}]^{-1} [\mathbf{J}^T \Delta \mathbf{y}]. \quad (4.9)$$

The linear scheme in Equation (4.9) can be applied in fluorescence DOT, i.e. when the unknown parameter is μ_{af} . This is appropriate since the fluorescence forward model has, intrinsically, linear dependence on the fluorophore concentration in its standard form.

4.4.3 The sensitivity matrix

The Jacobian, introduced in Equation (4.6), can be referred to as a sensitivity matrix. This matrix holds information about how large effect a small perturbation, of the optical properties, will have on the measurements. For example if fluorescence intensity measurements are acquired in a setup according to Figure 4.6 a

small fluorescent inclusion positioned far from the projection is hardly excited thus it has limited effect on the measurements. On the other hand when the inclusion is placed in front of the source or detector the presence of the fluorophore will become evident. By visualizing one row in the Jacobian matrix, seen in Figure 4.6, the spatial sensitivity of each source-detector combination can be analyzed.

The explicit formation of the Jacobian is effectively achieved through the *adjoint formulation* where the reciprocity theorem is exploited, see Section 3.6 [217, 218]. Consider a setup where M fluorescence measurements (Γ_m) are performed in a volume discretized into N elements, each with the volume ΔV . The forward model for the j :th measurement, denoted with superscript (j) below, is retrieved through discretization of e.g. Equation (3.36). With $\Gamma_m = \mathcal{M}[\Phi_m] = C\Phi_m$ the forward model is given by

$$\Gamma_m^{(j)} = C \sum_{i=1}^N \Delta V \Phi_x(\mathbf{r}_s^{(j)}, \mathbf{r}_i) \eta(\mathbf{r}_i) \tilde{g}_m(\mathbf{r}_i, \mathbf{r}_d^{(j)}). \quad (4.10)$$

The reciprocity theorem is now applied meaning that $\tilde{g}_m(\mathbf{r}_i, \mathbf{r}_d) = \tilde{g}_m^+(\mathbf{r}_d, \mathbf{r}_i)$ where $+$ indicate the adjoint form. The advantage of the adjoint form is due to the reduction in computational cost. Without the adjoint formulation the example above would require N calculations of $\tilde{g}_m(\mathbf{r}_i, \mathbf{r}_d)$. The adjoint form yields the same result through one calculation of $\tilde{g}_m^+(\mathbf{r}_d, \mathbf{r}_i)$.

Including all measurements, Equation (4.10) forms a linear equation system given by $\mathbf{y} = C\mathbf{J}\mathbf{x}$ where

$$\begin{aligned} \mathbf{y} &= [\Gamma_m^{(1)}, \Gamma_m^{(2)}, \dots, \Gamma_m^{(M)}]^T, \\ \mathbf{x} &= [\eta(\mathbf{r}_1), \eta(\mathbf{r}_2), \dots, \eta(\mathbf{r}_N)]^T, \\ \mathbf{J} &= \begin{bmatrix} J_{1,1} & \dots & J_{1,N} \\ \vdots & J_{j,i} & \vdots \\ J_{M,1} & \dots & J_{M,N} \end{bmatrix}, \\ J_{j,i} &= \Delta V \Phi_x(\mathbf{r}_s^{(j)}, \mathbf{r}_i) \tilde{g}_m^+(\mathbf{r}_d^{(j)}, \mathbf{r}_i). \end{aligned}$$

The formation of the Jacobian presented above adheres to the inverse problem when a fluorophore is to be reconstructed using absolute intensity measurements. Measurement transformations and normalization lead to modification of the sensitivity matrix.

A common approach to avoid absolute intensity measurements is to use the *normalized Born approximation* [219]. Here the fluorescence intensity measurements are scaled with the transmitted excitation light. The measurable then becomes

$$\mathbf{y} = \frac{\Gamma_m}{\Gamma_x}. \quad (4.11)$$

The Jacobian matrix must then be updated accordingly. The sensitivity matrix for the normalized Born measurable is here denoted $\mathbf{J}^{(\text{NB})}$, whereas \mathbf{J} is the Jacobian defined above.

$$\mathbf{J}^{(\text{NB})} = \frac{1}{\Phi_x(\mathbf{r}_s, \mathbf{r}_d)} \mathbf{J}. \quad (4.12)$$

The normalized Born measurable has shown certain robustness towards heterogeneous optical properties. Hence homogeneous representation of the bulk optical properties is commonly employed when the Jacobian is formed [220].

Another approach is to adopt the logarithm of the fluorescence intensity so that the measurable is defined by

$$\mathbf{y} = \log \Gamma_m. \quad (4.13)$$

The updated Jacobian, denoted $\mathbf{J}^{(\log)}$, is given by [221, 222]

$$\mathbf{J}^{(\log)} = \frac{1}{\Phi_m(\mathbf{r}_s, \mathbf{r}_d)} \mathbf{J}. \quad (4.14)$$

Here Φ_m is the forward model for the fluorescent light propagation which depends on the distribution of the fluorophore. This means that in each iteration of Equation (4.8), the Jacobian must be updated according to the current solution.

In addition to the fluorophore reconstruction, utilizing any of the Jacobian matrices presented above, the bulk optical properties, i.e. μ_a and D , can be estimated. In analogy to the discussion and notation above the Jacobian elements are [217, 218]

\mathbf{x}	\mathbf{y}	$J_{j,i}$
μ_a	Γ	$\Phi(\mathbf{r}_s^{(j)}, \mathbf{r}_i) \tilde{g}^+(\mathbf{r}_d^{(j)}, \mathbf{r}_i)$
D	Γ	$\nabla \Phi(\mathbf{r}_s^{(j)}, \mathbf{r}_i) \nabla \tilde{g}^+(\mathbf{r}_d^{(j)}, \mathbf{r}_i)$

The discussion above considers one spectral band for the Jacobian. When multispectral measurements are applied the Jacobian should be expanded. The rationale is essentially to stack several matrices into one large system matrix. Examples of multispectral sensitivity matrices, with the intent to reconstruct spectrally resolved absorption and scattering coefficients, can be found in [142, 223, 224]. A Jacobian matrix for spectrally resolved luminescence is presented in [225] whereas reconstruction of fluorophores with different lifetimes can utilize a system matrix reported in [226]. In Paper II a multispectral Jacobian matrix is presented for multiple fluorophore reconstruction. This will be further discussed in Chapter 5.

4.4.4 Regularization parameter

As stated before the problem is ill-posed and the Jacobian is typically ill-conditioned⁴. In order to alleviate this problem the reg-

⁴An ill-conditioned matrix has a large condition number. When such a matrix is inverted small errors in the measurements can cause large errors in

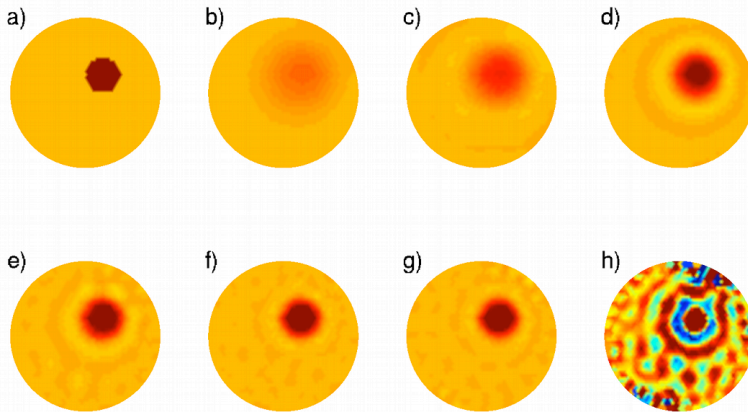


Figure 4.7. The influence of regularization parameter on the inverse problem. The reconstruction target is an absorbing inclusion seen in a). The reconstructions using Equation (4.8) are shown in b)-h) where λ is given by b) 100, c) 10, d) 0.1, e) 10^{-2} , f) 10^{-3} , g) 10^{-4} and h) 10^{-5} .

ularization parameter λ and regularization matrix \mathbf{L} were introduced in Equation (4.7). The interpretation of the regularization parameter is that it balances how much trust that should be given to the residual norm relative the solution norm, in Equation (4.7). If λ is large the solution will favor a small solution norm leading to a smooth solution with little variation within the medium. Conversely a small λ allows a large solution norm while the residual norm is kept small. In this case the optical properties will vary with a high spatial frequency throughout the geometry. Hence the regularization parameter can be interpreted as a filter factor that controls the dampening of higher spatial frequency components in the inversion process.

The linear system in Equation (4.9), with $\mathbf{L} = \mathbf{I}$, can be analyzed by singular-value-decomposition (SVD) of the Jacobian. It can be shown that the filtering is actuated when $\lambda > \sigma_i$ where σ_i is the i :th singular value [214]. This explains the stabilizing features of the regularization since too low singular-values, due to a ill-conditioned matrix, are filtered out. The effect of λ , when $\mathbf{L} = \mathbf{I}$, is demonstrated in Figure 4.7.

In many cases the regularization is found with empirical means [142, 228]. Typically the regularization parameter is set to a high value initially and then decreased throughout the iteration process. The iteration stops when the relative residual norm, between two iterations, changes less than a predefined number. A potentially more intuitive tool is the L-curve method [229]. Here

the solution [227]

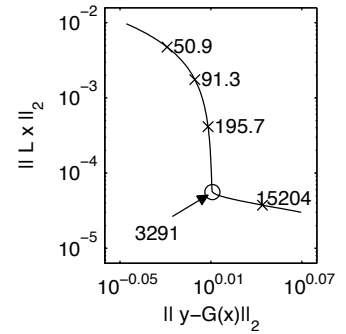


Figure 4.8. Result retrieved from the L-curve method where the corner (circle) indicates a good balance between solution norm and residual norm.

the solution norm and the residual norm are compared for different values of the regularization parameter. The comparison is represented by a graph ideally with the shape of the letter "L" where the regularization parameter that yields the best balance between the residual norm and the solution norm is given by the corner, seen in Figure 4.8.

Due to its graphical representation the L-curve method is applied in many branches of inverse theory. In addition to DOT [210, 230] and Paper **VIII** some examples are in dose optimization problems for external beam radiation therapy (EBRT) [231] as well as electron impedance tomography (EIT) [232]. In order to retrieve the graph the inversion needs to be done for several regularization parameters. Due to the inherited computational cost, this is an evident disadvantage. Using SVD this problem can be slightly alleviated [214].

4.4.5 A-priori information

In the discussion above the regularization matrix \mathbf{L} was set equal to the identity matrix \mathbf{I} . In this case the diagonal of $\mathbf{J}^T\mathbf{J}$ is made more dominant through the addition of $\lambda\mathbf{I}$. This effectively stabilizes the solution, i.e. the ill-conditioning is reduced. The regularization matrix can take other forms as well [233]. Typically \mathbf{L} is adapted according to some *a-priori* information.

One implication in DOT is that all voxels within a medium are not equally sensitive to an alteration of the optical properties as discussed previously and seen in Figure 4.6 [234–236]. One approach to balance the decreased sensitivity at larger depths is to modify $\lambda\mathbf{I}$. In spherical symmetry, e.g. DOT of breast tissue, a radially dependent regularization parameter can be imposed [234]. This will increase the achievable resolution at larger depths. A similar approach was applied in Paper **I** for a slab-shaped geometry utilizing multispectral fluorescence measurements to guide the regularization parameter.

Another approach is to impose prior information retrieved from an additional imaging modality, e.g. MRI or ultra-sound. Different tissue types are segmented from the complementary imaging setup and the segmented images then act as a constraint to the DOT reconstruction [237, 238]. The approach relies on the assumption that voxels within the same tissue region should have comparable optical properties, i.e. vary smoothly. A common approach is to define the elements in the regularization matrix according to [233, 239]

$$L_{j,i} = \begin{cases} 0 & \text{if } i \text{ and } j \text{ are not in the same region} \\ -1/N & \text{if } i \text{ and } j \text{ are in the same region} \\ 1 & \text{if } i=j \end{cases} \quad (4.15)$$

Subscripts i and j are column and row index respectively whereas N is the number of nodes within the given region.

4.4.6 Alternative inverse models

Alternatives to the DOT rationale described in preceding sections exist. The least squares objective function in Equation (4.7) is essentially a special case of the *Generalized Least Squares* (GLS) objective function [196]. Within this approach a weight matrix is imposed onto the residual norm in addition to the regularization matrix for the solution norm. The weight matrices are found through a prior estimate of the covariance matrices. For extensive information the reader is referred to [196, 240, 241]. The weight matrices in the GLS approach allows prior knowledge about the measurement characteristics as well as the optical property distribution to be incorporated in the inversion.

Another, rigorous, alternative is the *Bayesian framework*. A measurement model and prior constraints on the optical properties are included as probability density functions. The parameters of these models are iteratively updated in order to find the maximum *a posteriori* estimate of the optical properties, i.e. the most likely solution given the prior probability density functions [242–244]. The use of prior models that describe the optical property distribution provide a direct way to incorporate e.g. tissue-type regions, segmented from other imaging modalities [245, 246].

Several factors can cause the Jacobian to grow in size. For instance, high nodal density of the solution geometry, many sources and detectors and multispectral measurements all cause the matrix to become large. The computer memory then poses a limit. Creation of the Hessian matrix can be avoided using *Krylov methods* [247]. When the explicit matrices are formed the solution can be retrieved directly whereas utilizing Krylov methods the linear system in Equation (4.9) is solved using an iterative scheme. In brief such methods implicitly form the matrix-vector product "on-the-fly" as the iteration proceeds [248–250]. In Paper II a Krylov method was used and the implementation will be further discussed in Chapter 5.

Iterative gradient-based optimization schemes can also be implemented for DOT [126, 251]. The general DOT, in Section 4.4.2 scheme linearize the objective function in order to retrieve an update solution during the iteration process. In gradient-based schemes the linearization is omitted and the gradient of the objective function is calculated using numerical means [252]. The gradient is then used for a line-search in order to find to optimal optical properties for each iteration. The advantage of these methods is that the inversion of the Hessian matrix is avoided.

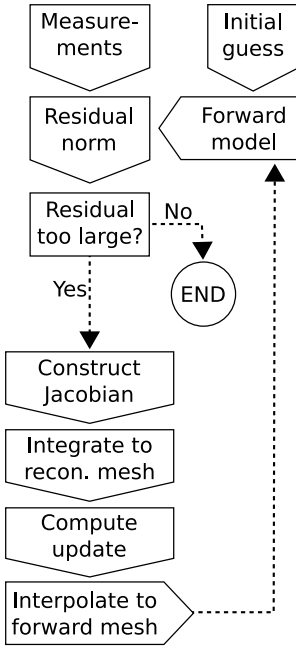


Figure 4.9. A schematic flowchart of the implementation of the reconstruction of optical properties.

4.4.7 Practical implementation

The previous sections have introduced the theoretical framework for retrieval of heterogeneously distributed optical properties. Within this thesis the practical implementation of this theory essentially follows the flow-chart depicted in Figure 4.9. The steps involved are briefly described below.

- (i) The first step is to assign an initial guess of the optical properties where the iteration will start. The homogeneous models in Section 4.3 can be applied for this purpose.
- (ii) A forward model, discussed in Chapter 3, describing the measurement setup and geometry is executed utilizing the initial guess. The model is computed on a forward mesh, or grid, defined by the geometry.
- (iii) The residual between measurements and forward modelled data is calculated.
- (iv) The governing system matrix, i.e. the Jacobian, is formed. In general this is a computer intense process owing to the large matrix size. The total number of source-detector pairs in addition to the number of nodes in the forward mesh defines the size of the Jacobian. In Chapter 5 the Jacobian for fluorescence DOT will be further discussed.
- (v) In order to reduce the matrix size in the inversion the Jacobian is integrated onto a regular grid with coarser nodal density. To some extent this leads to a reduction of the ill-posedness. The main advantage though is the reduction of the computational cost.
- (vi) The optical properties are updated according to Equation (4.8) or (4.9).
- (vii) The updated solution is mapped, or interpolated, onto the forward mesh. In practice this step governs additional smoothing of the solution.
- (viii) The forward model, employing the new optical properties, is executed again and the iteration proceeds until the residual is smaller than a predefined convergence criterion.

FLUORESCENCE IMAGING

As cancer evolves, cells will undergo mutations causing the tissue physiology to change. In addition each evolutionary step is preceded by cellular processes that promote, or inhibit, tumor growth [4], schematically depicted in Figure 5.1. In this chapter the role of fluorescence imaging to i) localize cancer and ii) image cellular processes, will be discussed.

Clinical diagnosis using fluorescence as a source of contrast is the focus of Section 5.1. Furthermore the field of molecular imaging, where targeted imaging of biological events is performed, will be described in Section 5.2. The intended use of multispectral fluorescence measurements in three-dimensional imaging of diffuse media is introduced in Section 5.3. The use of upconverting nanocrystals as means for autofluorescence-free imaging is discussed in Section 5.4.

5.1 Clinical photodiagnosis

A diagnostic method should optimally be able to distinguish malignant cells, from normal, in the initial phase of cell mutation. It is believed that the probability for successful treatment is increased when therapeutic modalities are mobilized at an early stage of cancer progression [2].

Fluorescence imaging provides versatile diagnostic means that can be applied in clinic with reasonable cost, for real-time examination of tissue. In general fluorescence imaging is performed using surface illumination and a camera equipped with spectral filters [192], see Figure 5.2. This modality is referred to as *planar fluorescence imaging* since it renders planar 2D images of the target region. During the past two decades a wide variety of multispectral imaging instruments have been developed for external diagnostics [189, 254] as well as endoscope applications [194, 255].

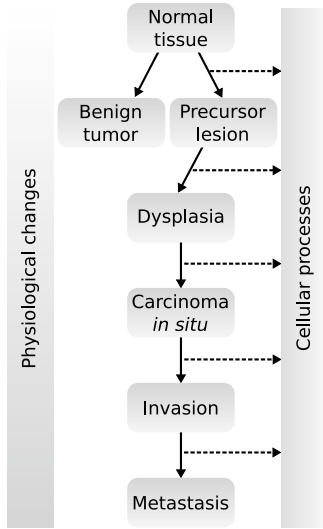


Figure 5.1. A schematic picture of the progression of cancer, from normal tissue to invasive tumor and metastasis. Adapted from [253].

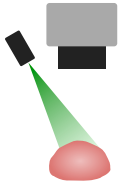


Figure 5.2. Planar fluorescence imaging.

Planar imaging with endogenous fluorophores

As mentioned in Section 2.3.1 the endogenous fluorophores are affected by changes in biochemistry, e.g. due to alterations in cell metabolism, within the tissue. These changes cause spectral differences, of the fluorescence emission, between (pre-)malignant and normal tissue [256]. By detecting planar images of autofluorescence, after excitation with blue light, investigations of cervical cancer [257], early gastric cancer [255], oral cavity [258], aero-digestive tract [259] and esophagus [260] have been performed. The general conclusion from these studies is that autofluorescence imaging renders increased sensitivity, i.e. more malignancies are diagnosed, compared to traditional white light examination. On the other hand the investigations are commonly affected by many false-positives, i.e. where benign tissue is characterized as malignant. The main reason behind the low specificity is variation of the optical properties within the bulk tissue [259]. In order to remedy this, fundamental, problem efforts are now applied to the development of miniature fiber-optic confocal microscopes as well as optical coherence tomography systems [258, 259, 261]. In this way, more detailed studies of the tissue structure can be performed potentially leading to increased specificity.

Planar imaging with exogenous fluorophores

Fluorescence imaging where exogenous fluorophores are applied rely on selective accumulation, or retention, in malignant lesions. Within the clinical context, photosensitizers are widely used since some of these have shown affinity to target cancer cells. The most widely used agent is the prodrug ALA, forming the photoactive agent PpIX, see Section 2.3.2. Improved specificity, due to differential uptake, has been demonstrated in applications such as bladder cancer [262], aero-digestive tract [259] and malignant skin lesions [187, 263]. In Paper V a liposomal formulation of mTHPC was administered to patients with basal cell carcinoma or squamous cell carcinoma and subsequently imaged in order to delineate the lesion.

Another important application of fluorescence imaging with exogenous fluorophores is as guidance during tumor resection. It was shown, recently, that the use of ALA enhanced the capability to remove all malignant cells, due to malignant glioma, as compared to white light inspection [72]. Currently the same approach is investigated within a clinical trial for prostatectomy [264].

Tomographic fluorescence imaging

All of the above mentioned studies use blue light for excitation. When malignancies deeper within the tissue are to be diagnosed, excitation light at a longer wavelength is required. The photons

will propagate through the entire target volume, as opposed to the superficially penetrating blue light, and consequently be affected by the bulk optical properties. Care must then be taken when interpreting the planar images from a fluorescence investigation since it is not possible to discriminate between a large lesion at shallow depth and a small lesion at larger depth, see Figure 5.3. This effect can be termed the fundamental non-uniqueness of deep-tissue fluorescence imaging.

The problem can be solved using a model-based approach, as discussed in Section 4.4. Then additional measurements, i.e. from multiple source-detector pairs, are adopted in the inverse model. It is then possible to localize, and potentially also quantify, a fluorophore within the tissue.

The instrumentation for *three-dimensional tomographic fluorescence imaging* (FDOT) can take many forms. Typically a large number of point-sources and point-detectors render datasets with numerous source-detector pairs. The sensitivity then spans the whole target volume allowing reconstruction of embedded fluorophores.

Efforts within the clinical arena have mainly focused on the development of schemes for breast cancer diagnosis. In a pilot study, Corlu et al. imaged three patients with ductal carcinoma using the systemic fluorophore ICG [265], see Section 2.3.2. The hybrid system utilize frequency-domain fiber-based remittance measurements, see Section 4.2, to reconstruct the bulk optical properties [230]. Several wavelengths within the NIR-interval are employed, hence oxygen saturation, total hemoglobin concentration and scattering properties can be assessed throughout the volume. Fluorescence measurements were performed in transmission mode, see Figure 5.4. The results demonstrated an increased fluorophore contrast, within the breast, at locations that correlated well with radiology examinations.

Davis et al. presented a method aiming to image localized accumulation of the photosensitizer Lutex [222]. The rationale incorporated a fiber-based system where sources and detectors are positioned around the perimeter of the breast, schematically depicted in Figure 5.5. In this phantom study the optical fibers were aligned inside a MRI-system rendering means for co-registration of important physiological and anatomical parameters. This multimodality approach allows incorporation of *a priori* information, discussed in Section 4.4.5.

Tomographic fluorescence imaging has also been investigated with a system utilizing measurements performed in remittance mode only. Here frequency-domain measurements, from a CCD-camera [266] and recently a handheld probe [267], was used in order to reconstruct inclusions made of ICG within optical phantoms. Although the feasibility of this setup was concluded the results indicate that this measurement geometry has a limit with

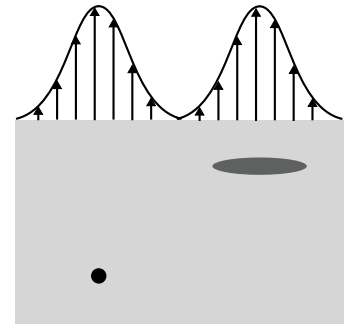


Figure 5.3. Schematic representation of the non-uniqueness in fluorescence imaging. Two fluorophores of unequal size will render the same surface exitance.



Figure 5.4. Single projection fluorescence tomographic imaging in non-contact mode.

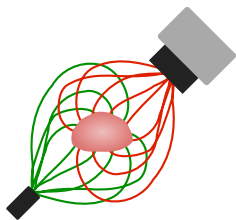


Figure 5.5. Fiber-based multi-projection fluorescence tomographic imaging.



Figure 5.6. Mouse during planar fluorescence imaging.

respect to inclusion depth. This is particularly evident when the inclusion is small and/or has low fluorescent contrast.

A pre-requisite for model-based fluorescence imaging is the knowledge of the intrinsic optical properties, i.e. absorption and scattering, prior to reconstruction. All of the systems, mentioned above, have this feature. Furthermore the transmission measurements are normally multispectral allowing derivation of the hemodynamics, and scattering properties throughout the volume under study. Changes in these parameters can, in addition to the fluorescent contrast, form important means for disease diagnosis. Examples of applications where non-fluorescent tomographic imaging systems have been clinically employed are breast imaging [268, 269] and functional brain imaging [270, 271].

5.2 Molecular imaging

When cancer progress from normal tissue to malignant, numerous cellular processes occur. For instance, activation of oncogenes or tumor-suppressor genes and regulation of transcription factors affect the tumor behavior. Imaging the cellular processes *in vivo* will provide means for increased understanding of the complexity of cancer. Furthermore by identifying tumor specific targets the specificity of therapy and imaging can potentially be improved. An example of a tumor-specific target is the epidermal growth factor receptor (EGFr). Another important aim in cancer research is to investigate whether a treatment modality is effective. This can be done in longitudinal studies where imaging agents are tracked *in vivo* over time. All of the above mentioned aspects form the motivation for research within the field *molecular imaging* (MI).

A large area of focus within MI is the development of new imaging agents, holding the ability to specifically mark a cellular target, see Section 2.3.2. As the use of such agents in humans require regulatory approvals investigations are performed pre-clinically on animal models [61]. This fact has given rise to the equally frequent name; small animal imaging (SAI). The intention is to translate the imaging probes and instrumentation to the clinic. So far no targeting probes have reached approval [272].

Many of the clinically available imaging modalities are also used within the field of molecular imaging. In addition to fluorescence imaging; MRI, PET, SPECT, CT and Ultrasound can be directly translated to SAI. Furthermore there exist some modalities that are specific to animal studies. Intravital microscopy is a valuable tool where a window is surgically implanted on the rodent skin. As opposed to traditional microscopy methods, this scheme allows imaging of tissues *in vivo*. Bioluminescence imaging (BLI) is governed by the use of transgenic animal models where a reporter gene can express the enzyme luciferase. Luciferin is admin-

istered to the animal and, following the enzyme reaction between the two compounds, light is emitted within the spectral range 500–580 nm [273]. Recently opto-acoustic imaging of small animals was demonstrated [274]. Here fluorophores are used as absorbers that, upon excitation, emits a pressure-wave which is collected at the surface by an ultrasonic detector. This rationale showed improved resolution of the rodent mouse brain. Summaries of present molecular imaging modalities are found in e.g. [61, 272, 275–277].

The use of fluorescence imaging instrumentation for SAI is partly motivated by the ample amount of different fluorophores, discussed in Section 2.3.2. In addition, optical techniques provide higher sensitivity when compared to other techniques. Due to the relatively short lifetime, in the order of ns, fluorophores can be repeatedly excited since the fluorophore returns to ground state after emission of a fluorescent photon. This leads to a high number of photons emitted each second, hence low fluorophore concentrations can be imaged [276, 278]. In addition the higher sensitivity allows real-time imaging [279]. Factors such as photobleaching and autofluorescence will, on the other hand, limit the achievable sensitivity [278].

Tomographic fluorescence imaging

The evolution of instrumentation for SAI with the intent to tomographically reconstruct deeply embedded fluorophores started in the beginning of present decade. Ntziachristos et al. investigated the feasibility, and subsequently, the performance of a tomograph comprising a cylindrical target chamber. Measurements were performed using fiber optics, similar to Figure 5.5, with the animal submerged in an index-matching liquid [219, 280]. In order to increase the number of detectors a CCD-camera was introduced in the setup. The high number of source-detector pairs governed the capability to resolve embedded fluorophores separated by less than 1 mm when inclusions were placed at a depth of approximately 7 mm [281].

Using the system above Zacharakis et al. showed that the progression of lung cancer in a mouse could be tracked quantitatively (number of cells) over 20 days [282]. GFP-expressing cancer cells were implanted into the murine lung and the fluorescence emission indicated the tumor growth.

Another study, performed by Ntziachristos et al. intended to investigate the capability to image cathepsin B expressing tumors in the brain of an animal model [283]. Overexpression of this compound is related to many forms of cancers. An activatable fluorescence probe was employed, sensitive to the presence of cathepsin B, see Section 2.3.2. Correlation between MRI and FDOT verified the capability to tomographically reconstruct protease activity *in vivo*.

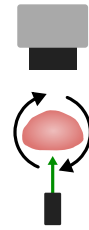


Figure 5.7. *Non-contact multi-projection fluorescence tomographic imaging.*

In order to avoid the need for index-matching liquids, non-contact tomographic imaging setups were proposed [284, 285], schematically depicted in Figure 5.4. Here the animal is placed on a target plate where a laser spot is translated in two dimensions on one side. In this way the number of sources can be increased arbitrarily. Thus the setup provides larger datasets that reduce the ill-posedness of the inverse problem to some extent. Another advantage is that the non-contact scheme provides slightly better image quality than fiber-based setups using a corresponding number of source-detector pairs [286]. A drawback is that the non-contact imaging setup requires accurate reconstruction of the surface shape of the animal so that the inverse problem is solved within the representative geometry. Another version of the non-contact setup is the fully rotational modality, seen in Figure 5.7. Opposed to the non-contact scheme above, where the sources irradiate one side of the animal (single-projection), here the mouse is rotated so that full angular coverage is retrieved (multi-projection) [287, 288].

All of the above mentioned systems employ steady-state fluorescence measurements but recently time-resolved tomographic fluorescence imaging was demonstrated using targeting NIR fluorophores [289] and fluorescent proteins [290]. Although more sophisticated instrumentation is required, the great advantage is that the fluorescence lifetime can be retrieved. Fluorescence lifetime imaging provides a complementary source of contrast to the integrated intensity.

A current trend in instrumentation development is the use of multimodal rationales. Here fluorescence and complementary measurements are co-registered. Such approaches include the combination of CT and FDOT for non-contact imaging of glioma [291]. Here the fluorescent agent PpIX, induced by ALA, was imaged using a setup resembling Figure 5.7. The intention of using CT was to delineate the animal shape although, as the authors state, it can also be used for demarcation of the cranium. Although no interaction between the two imaging modalities was employed the feasibility to accurately reconstruct the photosensitizer was concluded when fusing the post-processed images together.

In a similar CT-FDOT setup neurodegenerative disease was imaged where different tissue types was retrieved from CT and imposed as prior information in the FDOT reconstruction [292]. A NIR fluorophore targeting amyloid- β plaques was employed. Different regularization parameters were assigned to the tissue types leading to good agreement between *in vivo* reconstructions and *ex vivo* investigations.

Simultaneous imaging using MRI and FDOT was very recently demonstrated in the investigation of a NIR fluorophore, targeting EGFr on implanted pancreatic cancer cells in a small animal model [293]. The organs, segmented from MRI, were included as prior information in the optical reconstruction, see discussion in

Section 4.4.5. The results indicated that the level of fluorophore in each organ, and tumor, could be tracked using MRI-FDOT. Using this approach the EGFr bearing cells could potentially be studied over long time. This is important since response after therapy, that targets EGFr, can be studied *in vivo*.

5.3 Multispectral tomographic imaging

Several reports propose the use of multi-labeling, meaning that several cellular targets are imaged simultaneously using different fluorescent probes [272, 282, 292]. In order to separate the spectrally-encoded inclusions multispectral measurements are required.

When multiple fluorophores are imaged the emission spectra can overlap hence images acquired in each spectral band will have contributions from all fluorescent agents. Several image processing schemes to distinguish the imaging probe have been proposed. For instance Andersson-Engels et al. constructed a system with the capability to simultaneously collect images in three spectral bands [189]. The images were then used to form a contrast function that could be used to distinguish regions with high photosensitizer levels. When more spectral bands are available a method, normally referred to as *spectral unmixing*, can be applied [294]. Reference spectra for the relevant fluorophores, i.e. those present in the tissue under study, are then fitted to the spectrally resolved intensities for each pixel. In this way the multispectral dataset is decomposed into maps detailing the distribution of each fluorophore. Recently spectral unmixing was demonstrated when quantum-dots, positioned superficially on a mouse, were imaged [67]. It was shown that the image-processing algorithm could separate each dot from the autofluorescence background [295].

The rationale for spectral unmixing can be extended to tomographic imaging of multiple fluorophores. As an example, consider two fluorophores, C_1 and C_2 , with emission spectra according to Figure 5.8a. The sensitivity matrix for the n :th spectral band is denoted $\mathbf{J}^{(n)}$ and defined in Section 4.4.3. Furthermore the extinction coefficient for C_1 or C_2 is given by ε_1 and ε_2 respectively. The spectral characteristics are described by the yield, see Section 2.3. The probability that the k :th fluorophore will emit light within the n :th spectral band is denoted $\gamma_k^{(n)}$. The multispectral Jacobian then becomes

$$\mathbf{J}^{(\text{MS})} = \begin{bmatrix} \gamma_1^{(1)} \varepsilon_1 \mathbf{J}^{(1)} & \gamma_2^{(1)} \varepsilon_2 \mathbf{J}^{(1)} \\ \gamma_1^{(2)} \varepsilon_1 \mathbf{J}^{(2)} & \gamma_2^{(2)} \varepsilon_2 \mathbf{J}^{(2)} \\ \vdots & \vdots \\ \gamma_1^{(M)} \varepsilon_1 \mathbf{J}^{(M)} & \gamma_2^{(M)} \varepsilon_2 \mathbf{J}^{(M)} \end{bmatrix}. \quad (5.1)$$

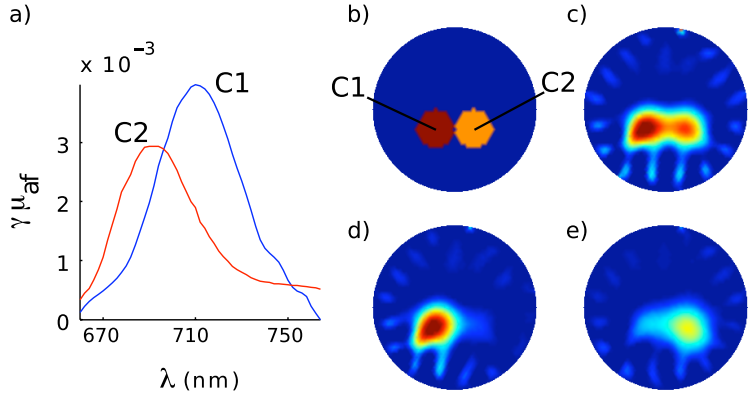


Figure 5.8. FDOT with two fluorophores (C1 and C2) with different spectral characteristics. In a) the spectra for inclusion C1 and C2, b) the simulated geometry, c) monospectral reconstruction ($\lambda_m = 700$ nm), and d-e) multispectral reconstruction ($\lambda_m = 670, 680, \dots, 750$ nm) for C1 and C2 respectively. Color scale is identical in all panels.

In order to elucidate the capability of multispectral reconstruction a simulation case of the geometry seen in Figure 5.8b was performed. Excitation wavelength $\lambda_x = 660$ nm and emission wavelengths $\lambda_m = 670, 680, \dots, 750$ nm were used. Reconstruction of the dataset, employing only one spectral band at $\lambda_m = 700$ nm results in Figure 5.8c. The multispectral reconstruction is shown, for C1 and C2, in Figure 5.8d-e. The ability to differentiate between the fluorophores is clearly seen when compared to Figure 5.8c. Some cross-talk between the fluorophores is evident, most pronounced in Figure 5.8e. This is an effect of overlapping fluorescence spectra, for the two fluorophores. This problem can be alleviated by optimizing the choice of spectral bands [296, 297]. Another factor, that potentially can cause cross-talk, is the relative balance between the measurements in different spectral bands. If signal in one band is strong and the others are weak the reconstruction will mostly be affected by the strong spectral band. One approach is presented in Paper II. In the example above, no scaling is applied.

Apart from spectral unmixing of multi-labelled datasets, multispectral reconstruction also renders reduced ill-posedness of the inverse problem [296, 298]. This is a consequence of varying bulk optical properties that affect each spectral bands differently, effectively adding independent information to the system. Another way of stating this fact is that the inclusion depth is encoded in the fluorescent spectrum [299]. Chaudhari et al. reported on image improvements when expanding the acquisition to multispectral

excitation, in addition to multispectral emission, which could be explained by a reduction of the ill-posedness [300]. The spectral encoding of the depth was exploited in Paper **I** in a somewhat different manner. Instead of performing a multispectral reconstruction the depth encoding was introduced in the regularization parameter, hence guiding the solution to a prior estimate of the location.

Several factors cause the multispectral system matrix, in Equation (5.1), to grow in size. Assume a scenario with multispectral non-contact imaging in transmission mode where a laser-spot is translated on one side. With 100×100 pixels, 10 spectral bins, 10×10 sources and a reconstruction grid of 10 000 nodes the Jacobian matrix will have the size $10\,000\,000 \times 10\,000$. This would require approximately 800 GB of memory. Fortunately, the problem with large datasets can be alleviated in several ways.

Parallel programming followed by execution of the inverse problem on a computer cluster is one alternative [301]. Unfortunately this leads to ample requirements on hardware not available for all. Another approach is to only include subsets of the measurements that cause a reasonable contribution to the inversion [302]. Here subsets of source-detector pairs are selected based on their projection error, i.e. the error between measurements and forward calculation. Only those subsets with large projection errors are included in the inversion effectively reducing the size of the system matrix. Effective inversion has also been reported using an analytical approach where the forward model is given by the Green's function to the DE in a slab-shaped geometry [303, 304]. Briefly this approach relies on formation of a singular value decomposition of Equation (3.36). The result is then used to form the pseudoinverse of the system matrix. Further details can be found in [305].

A *Krylov*-method, that avoids the explicit formation of the Jacobian matrix, was used in Paper **II** in order to reduce the computational cost. This is an iterative method implemented in common solvers for linear problems, such as the Generalized Minimum RESidual (GMRES) algorithm. The problem to be solved is given by Equation (4.9), and stated here again,

$$[\mathbf{J}^T \mathbf{y}] = [\mathbf{J}^T \mathbf{J} + \lambda \mathbf{L}^T \mathbf{L}] \mathbf{x} \Rightarrow \mathbf{z} = \mathbf{H} \mathbf{x}. \quad (5.2)$$

At iteration k the GMRES solver forms an approximate solution \mathbf{x}_k as a linear combination of the vectors spanning the Krylov subspace. These vectors are given by

$$\{\mathbf{z}, \mathbf{H}\mathbf{z}, \dots, \mathbf{H}^{k-1}\mathbf{z}\} \quad (5.3)$$

It is noted above that the matrix \mathbf{H} is only accessed as a matrix-vector product. Hence by introducing a subroutine that returns the matrix-vector product at each iteration, Equation (5.2) can be solved without the need to store the system matrix. The outline

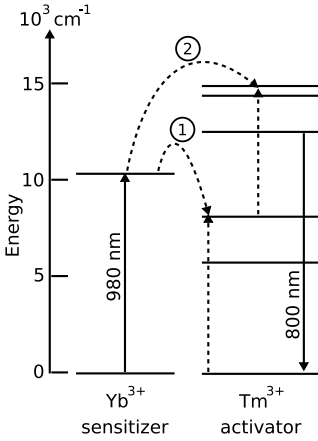


Figure 5.9. Energy level diagram of the upconverting process. Numbers indicate the 1- or 2-photon process while non-radiative decays are omitted.

of this subroutine is given in Appendix C, adopted from Paper **II**. A more detailed presentation is found in [250]. A comparison between a regular solver, where the matrix is formed and stored, and the Krylov-method above was performed in Paper **II**. This comparison verified a substantial reduction in computational cost both in terms of time and memory allocation. Further information about Krylov methods in general can be found in [247, 306] and in a recent review within the field of inverse problems for diffuse optics [307].

5.4 Nanoparticle-mediated imaging

In the section above spectral unmixing was discussed as a tool to unravel the autofluorescence from the measurements. Since this method relies on the knowledge of intrinsic fluorophore spectra, these must be explicitly determined. The acquisition of base-spectra is not always possible and relying on spectral libraries might induce erroneous results [308]. Hence, there is a need for autofluorescence-free imaging.

For this purpose upconverting nanocrystals were investigated in Papers **III** and **IV**. These compounds have a unique feature in that they emit anti-Stokes shifted emission, i.e. at a shorter wavelength than the excitation light. Upconversion can occur through several processes. In 1959 it was proposed by Bloembergen that infrared photons could be counted through detection of visible light arising from a material, doped with ions, after sequential absorption [309]. This process, called Excited-State Absorption (ESA), has low probability to occur since it is highly unlikely that two incoherent photons will simultaneously excite a single ion. Using coherent laser sources it is possible observe the ESA-process [310]. Another process, called Energy Transfer Upconversion (ETU), was proposed by Auzel in 1966 where he suggested that upconversion was mediated by an energy transfer between two rare-earth ions [310]. The key point, made by Auzel, is that the energy transfer occur between excited states in both ions. ETU is efficient even when excitation is performed with incoherent light, hence it is deemed to be the most dominant upconverting process. Other processes can occur and a detailed discussion about these is given in [310].

Upconverted emission has been observed in many materials but the fluoride crystal NaYF_4 is probably the most efficient [311]. ETU can be achieved when doping the host crystal with the ion-pairs $\text{Yb}^{3+}/\text{Er}^{3+}$ or $\text{Yb}^{3+}/\text{Tm}^{3+}$. The upconversion process for the latter ion-pair is depicted schematically in Figure 5.9. Yb^{3+} is called a *sensitizer* and absorbs the excitation light. Energy is then transferred, non-radiatively, to Tm^{3+} which is called an *activator*. In Figure 5.9, 1- and 2-photon energy transfer is indicated where the

latter govern emission at 800 nm. This emission band was exploited in Papers **III** and **IV**. The efficiency of the upconversion process is highly dependent on how the particles are produced. For instance impurities, crystal structure and improper annealing temperature can cause lower levels of emission [312, 313]. Furthermore the relative concentration of the two rare-earth ions play an important role when aiming for higher efficiencies [311].

In order to use the nanocrystals for biomedical imaging, the hydrophobic particles need to be made biocompatible. The common rationale is to coat the particles so that hydrophilic properties are achieved. Chatterjee et al. reported on the use of polyethyleneimine (PEI) [68]. PEI holds amino groups that make the compound water soluble. In addition the amino groups provide means for conjugation of targeting molecules, discussed in Section 2.3.2. The study comprised investigations of cell viability and tissue distribution of the agent in a murine animal. It was concluded that the agent was non-toxic. Furthermore the authors demonstrated targeted microscopic imaging of cancer cells holding high levels of folate receptors. The nanoparticles were conjugated with a folic acid effectively attaching to the surface of the cancer cells. The agent was also administered subcutaneously rendering a tissue distribution of the nanoparticles to depths of 10 mm. Despite the relatively large depth planar imaging in reflectance mode was capable of detecting the fluorescence.

In another demonstration Jiang et al. produced silica-coated nanocrystals conjugated with folic acid or Anti-HER2 antibody [314]. In addition they attached a siRNA molecule to the compound in order to investigate gene silencing in cells. This, microscopy, study verified the feasibility of targeted imaging using upconverting nanoparticles.

The capability for autofluorescence-free imaging was demonstrated in Paper **III** where a planar imaging setup was employed, in transillumination mode. Based on phantom measurements, it was verified that the signal-to-background was superior when compared to a regular fluorophore, irrespective of background fluorescence. The same was found by Vinegoni et al. who placed nanoparticles in glass capillary tubes inserted in the esophagus of a mouse, post-mortem [70]. The pilot study comprised particles coated with polyethylene glycol (PEG) polymers.

In Paper **IV**, the feasibility of tomographic imaging of upconverting nanoparticles was investigated. Since the upconverting process is a two-photon process whereas a regular fluorophore is excited by one photon the forward model must be modified. In Paper **III** the fluorescence intensity was measured as a function of excitation power and it was concluded that the dependence is indeed non-linear. The source term for the fluorescent DE, see Equation (3.33), is adapted by incorporating the parameter κ so

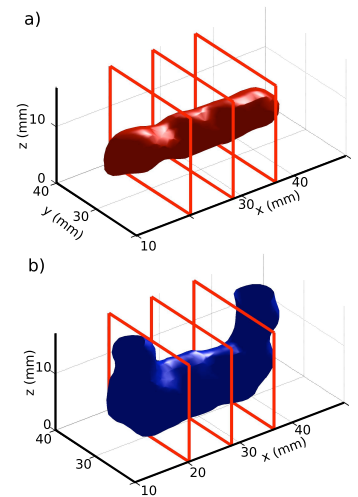


Figure 5.10. Reconstruction of a rod inside a slab-shaped optical phantom using a) upconverting nanocrystals b) regular fluorophore.

that

$$q_m(\mathbf{r}) = C\Phi_x^\kappa(\mathbf{r})\eta(\mathbf{r}). \quad (5.4)$$

For a regular fluorophore $\kappa = 1$ whereas $\kappa = 2$ holds for the up-converting particles used here. C is a constant accounting for the efficiency and $\eta(\mathbf{r})$ is the unknown parameter to solve for. The reconstruction results for upconverting particles and a regular fluorophore (Rhodamine 6G) are shown in Figure 5.10a and b, respectively. It is seen that the non-linear fluorophore is slightly more confined and affected by less artifacts than compared to the linear fluorophore. The improved reconstruction results are believed to arise mainly from the fact that no autofluorescence affect the measurements. Another cause is that the quadratic source has a more narrow sensitivity profile. Referring to the sensitivity profile in Figure 4.6, the sensitivity map for a non-linear reconstruction will have a slightly more narrow shape, close to the source. In practice this is seen when translating the source. Strong fluorescence will mainly be emitted when the source is close to the non-linear fluorophore. Hence the fluorescence measurements are more sensitive to the position of the fluorophore. This increased, spatial, sensitivity then renders the improved confinement of the inclusion.

Autofluorescence-free imaging has great potential in rendering means for sensitive tissue imaging. Linear fluorophores are limited by the signal-to-background, where the background is defined by the autofluorescence. Upconverting nanocrystals, on the other hand, are limited by signal-to-noise in the detection setup. A higher sensitivity of the imaging modality will render the possibility to investigate inclusions formed by a lower number of fluorescent compounds. In order to improve the sensitivity further the efficiency should be increased. One way of doing so is to employ higher excitation power using a scheme where a pulsed laser is used. This rationale would provide high peak power for efficient upconversion while keeping the average power moderate. Optimization of the excitation scheme in this way is of ample importance when considering the intended use, i.e. small animal imaging. With a moderate average power, side-effects such as tissue coagulation can be avoided.

PHOTODYNAMIC THERAPY

Photodynamic therapy (PDT) relies on the photodynamic action, introduced in Section 2.4, where light, oxygen and a photosensitizer interact, optimally resulting in tumor regression. Table 6.1 summarizes indications for which PDT has been approved within EU, Japan and the US. In addition some clinical trials and pre-clinical studies where active research is performed are mentioned therein. It is not the intent to fully summarize PDT in the clinical arena, instead the short summary included here will enlighten the importance of dosimetry in clinically applied PDT.

The first malignant indications to be investigated in larger scale, by Dougherty et al. in 1978, were cutaneous tumors and metastases where spot-illumination governed the activation of HpD [19]. The authors elucidated the need for dosimetry due to two reasons. First, thick tumors failed to respond completely to the treatment and second, healthy skin was destroyed when too long treatment times were employed. In order to avoid the long skin photosensitization following HpD-PDT, Kennedy et al. administered the pro-drug ALA topically to invasive squamous cell carcinoma on the skin [85]. Complete response was retrieved in most tumors except cases where the tumor was thick.

PDT of superficial malignancies inside cavities have been extensively studied. Using optical fibers guided by endoscopes, Photofrin-PDT has been shown to be an effective palliative treatment option for unresectable lung cancers [315]. The same rationale can be adopted to treatment of papillary bladder cancer, i.e. tumors residing in the bladder wall [316]. Here the need for *in-situ* dosimetry was concluded by Star et al. who showed that the fluence rate within the tissue can be manifold larger than expected due to the scattering properties of the tissue [317].

In order to ascertain that the whole target volume received a pre-defined light dose, theoretical forward models based on the diffusion equation were developed [332, 333]. The intended use of

Drug	Approvals	Investigations/Trials
Photofrin	Esophageal, Lung, Endobronchial, Gastric Papillary bladder and Cervical cancer [318]	
ALA-PpIX	Actinic keratoses [85] Basal cell carcinoma [320]	Brain [319]
BPD	Age-related macular degeneration [321]	Pancreas* [90]
mTHPC	Head and neck [322–324]	Prostate Paper VII Pancreas [325]
WST09		Prostate [326, 327]
Lutex		Prostate [328] Lung cancer* [329]

Table 6.1: Selected photosensitizers in use for clinical applications as well as clinical and pre-clinical investigations. Current status of clinical PDT is reviewed in e.g. [105, 330, 331]. *indicate pre-clinical studies.

these models was to determine the treatment time so that healthy tissue was left unharmed. Another, more practical approach, is to tailor the light applicator to a custom design. A recent example is the treatment of nasopharyngeal carcinoma, i.e. upper throat, where a custom-made silicone light guide delivers therapeutic light. In addition the applicator measures the fluence rate for *in situ* light dosimetry assessment [334].

Progress towards the treatment of solid tumors was enabled through the development of photosensitizers activated at longer wavelengths, such as BPD, mTHPC, Tookad and Lutex. Furthermore deep-seated tumors can be treated when applying interstitially placed optical fibers [19]. It is then of ample importance that the fibers are guided to the intended location. Beck et al. applied ALA-PDT to eradicate brain tumors where the optical fibres were placed stereotactically inside the tumor [319]. No evident side-effects, following the treatment, rendered the conclusion that ALA-PDT of recurrent and nonresectable malignant glioma is a safe therapeutic option. The approach considered a fixed treatment time and normal tissue destruction was avoided through selective photosensitizer retention [72].

Recently, endoscopically applied interstitial PDT, guided by CT and ultra-sound, was shown to efficiently induce necrosis of tumors in the pancreas [325] and malignancies in the biliary tract [335]. Both reports apply a fixed light irradiation scheme. Furthermore they indicate a significant risk of complications due to sensitive organs-at-risk surrounding the target region.

The potential of using interstitial mTHPC-PDT as a treatment option for recurrent head and neck cancers has been investigated where ultra-sound imaging governs the guiding of treatment fibers [322]. Here an empirical dosimetry approach was taken since the fibers were placed based on the prior investigations of necrosis radius due to a fiber. Consequently, as the authors conclude, the treatment response varies between patients.

As PDT progress towards deep-seated solid tumors it is evident, based on the selected studies above, that more detailed dosimetric considerations must be adopted. Firstly the proper light and drug dose must be ensured throughout the whole target volume. Secondly the dose outside the target region must be limited in order to avoid normal tissue destruction. Here the use of photosensitizers with higher affinity to selectively accumulate in malignant tissues, e.g. ALA-induced PpIX, can be considered. On the other hand, the activation of this agent at 635 nm might be ineffective when targeting larger volumes due to limited penetration depth. Thirdly, patient-specific dosimetry should be applied in order to limit patient-to-patient variability of treatment response [336].

In order to proceed towards individualized PDT dosimetry a thorough understanding of the factors affecting PDT efficacy is needed, which is given in Section 6.1. Following this section the theoretical framework of how to achieve an effective treatment response is discussed in Section 6.2. The use of interstitial PDT for prostate cancer will be reviewed in Section 6.3 followed by a discussion, in Section 6.4, about the PDT-rationale in Lund. Lastly the approach to include tomographic fluorescence imaging for dosimetry within prostate-PDT is presented in Section 6.5.

6.1 Factors affecting PDT efficacy

The route to tumor regression following PDT is affected by a number of factors such as choice of photosensitizer, concentration of the photosensitizer, time between administration and irradiation, light fluence dose, light fluence rate and oxygen availability. All of these parameters can in addition affect each other, schematically depicted in Figure 6.1 and further explained below.

Light dose, or fluence, is determined by integrating the fluence rate over the treatment time.

- The mode of cell-death is dependent on the total light dose. In general, studies show that a low light dose leads to apoptotic cell death whereas a high light dose results in direct necrosis [108, 109]. Since the fluence rate decreases with distance from light source, this leads to a spatial variation of cell-death mechanism ranging from necrosis near the source to apoptosis at longer distances.

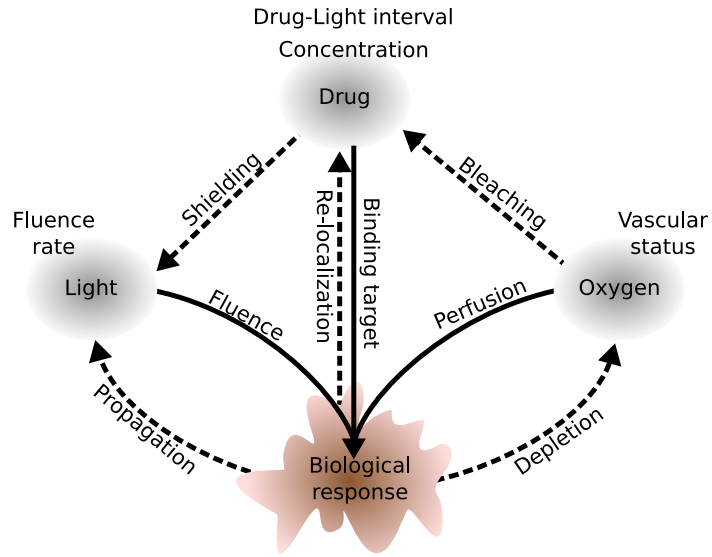


Figure 6.1. Factors that promote (full lines) or impede (dashed lines) PDT efficacy.

- The fluence rate has another important role since several reports conclude that a lower fluence rate render decreased probability for cell survival while keeping the total fluence constant [109, 337–340]. Using a higher fluence rate the oxygen consumption increases and there is a predominant risk for PDT-induced hypoxia [341, 342]. With a lower fluence rate the oxygen consumption is kept relatively modest although the treatment time is prolonged so that the corresponding light dose is reached. In order to avoid oxygen depletion, at high fluence rates, fractionating the treatment light has been shown to slightly improve the treatment outcome. Here dark intervals, in the order of minutes, are included allowing re-oxygenation of the tissue [343, 344].
- The light propagation can be affected by altered optical properties due to the biological response. For instance the treatment light attenuation can increase dependent on temporal changes of oxy- and deoxy-hemoglobin concentration [345, 346]. In practice higher therapeutic light attenuation leads to a smaller treatment volume.

Drug distribution and concentration, following administration to the body, is highly dependent on what type of photosensitizer and what type of delivery vehicle is used.

- The binding sites for the photosensitizers, see Table 2.1 in Section 2.4.2, determine the biological response. Drugs bound to intra-cellular components will induce direct tumor cytotoxicity, when localized to a malignant cell. Conversely, photosensitizers that stay in in the blood vessels render vascular destruction. In addition the photosensitizer can relocate after light delivery has commenced, effectively altering the cellular PDT target [347]. The selectivity can be improved when altering the drug formulation to e.g. a liposomal delivery vehicle administered systemically [348]. In this case the intent is to increase the LDL-receptor targeting by encapsulating the drug into liposomes [349].
- The drug-light interval (DLI), i.e. the time between administration of the drug and light delivery, plays a central role in PDT. In general a long DLI will allow the drug to diffuse out from the vasculature and potentially localize in cells. At shorter DLI the drug still remains in the vasculature leading to a vascular response [91, 350, 351]. Pharmacokinetic studies on mTHPC administered intravenously in animals have shown that the drug level in tumorous tissue increase while normal tissue level remain constant over a period of 1-3 days [352, 353]. The differential uptake has spawned the rationale to deliver light at longer DLI, typically 2-4 days. On the other hand more recent studies report that the long-term PDT outcome can be improved while using shorter DLI, within 3-5 hours [354, 355].
- The photosensitizer concentration available for mediating PDT-reactions can be reduced through photobleaching. mTHPC is proposed to mediate a Type II-reaction hence singlet oxygen is responsible for cell damage [93]. The bleaching of the drug occurs when the singlet oxygen reacts with the photosensitizer. Hence a higher local singlet oxygen concentration would induce increased photobleaching rate, for a given light dose. In analogy with the discussion above the photobleaching of mTHPC has been shown to depend on the fluence rate where a lower fluence rate leads to faster bleaching [356, 357].
- Drug distribution can affect the light propagation. A high drug concentration will increase the absorption coefficient of the medium and in worst case diminish the treatment volume, referred to as shielding [358].

Oxygen is supplied to the tissue via re-perfusion from the blood vessels.

- Following a vascular response to PDT, ischemia can occur. As mentioned above the long-term treatment efficacy is improved through vascular damage [359].
- Oxygen is transported by oxy-hemoglobin and since oxygen is consumed during PDT the ratio between oxy- and deoxy-hemoglobin can change. This can lead to alterations in the absorption within the medium hence affecting the light propagation [346].

With the interdependent relations between the factors above, it is clear that rendering a therapeutic response to PDT is intricate and care must be taken when optimizing treatment parameters. A remedy to the complexity is retrieved through the threshold dose concept. Discoveries were made of a marked boundary between necrotic and healthy tissue following light irradiation, in the presence of photosensitizer and oxygen [360]. In order to describe this effect the *threshold dose* was introduced [361]. This dose defines the minimum level of reactive oxygen species that will induce direct cell death [358]. As will be discussed in the following section the threshold dose forms the fundamental assumption in several PDT-dosimetry models.

6.2 Dosimetry models

A dosimetry model should be able to predict the biological response to therapy. Generally, a dose metric is defined that optimally correlates to the response.

In treatment planning for ionizing radiation therapy (IRT), the dose metric is given by the absorbed radiation dose in the tissue volume. Here, dose-response curves can be defined that states the probability for tumor control following therapy when using a specific dose [8]. At the same time care must be taken so that healthy tissue is spared [362].

In PDT, the same approach is taken when relying on the threshold dose concept. The target tissue should receive a dose above threshold, while healthy tissue should be exposed to a lower dose. The complexity of PDT dosimetry arise when the dose metric is to be defined. It is evident from the previous section that the route to malignant cell death is affected by numerous factors. In order to handle this complexity, various assumptions are made in the dose models that will be presented hereafter.

In general, the necrosis is assumed to be mediated by direct cell death hence apoptotic and immunological responses are omitted. Furthermore, the cell death is mediated by the direct effect of the threshold dose, i.e. not by any secondary responses due to cell death in other parts of the tissue. Microscopic properties, such as binding target and re-localization of the drug are also omitted.

6.2.1 Dosimetry through biological response

As opposed to many other treatment modalities, in PDT the initial tissue response occurs promptly, making it possible to observe readily during treatment [346, 359, 363–366].

Bold-MRI has for instance been applied during vascular targeted PDT using Tookad [367]. It was shown that the MR-contrast decreased upon light irradiation of an animal model indicating a rapid deoxygenation of the tissue.

The blood flow can be monitored using Doppler-ultrasound imaging [368] or optical techniques such as diffuse correlation spectroscopy [368] and interstitial Doppler optical coherence tomography [369]. A reduction of blood flow is expected following a vascular response to PDT.

In a recent pre-clinical study the feasibility of monitoring the vascular destruction following ALA-PDT was shown using optoacoustic imaging [370].

More delayed tissue response is investigated days after treatment using MRI [371]. A decreased contrast enhancement then indicate necrotic regions that potentially can be used for correlation to the threshold dose. Although a great potential arise in biological response monitoring a dose-metric capable of predicting the tumor outcome is yet to be defined.

6.2.2 Direct dosimetry

The principal mediator for PDT is singlet oxygen [73]. Within the direct dosimetry model, this compound is monitored directly. A dose metric can then be defined by

$$D_{\text{oxy}} = \int_0^T \frac{[{}^1O_2](\mathbf{r}, t)}{\tau_{\Delta}} dt \quad (6.1)$$

where τ_{Δ} is the singlet oxygen lifetime, before it reacts with a substrate, and T is the treatment time.

Singlet oxygen can dissipate its energy by emission of photons at 1270 nm, called luminescence. Hence, integrating the luminescence signal yields a direct measure of the singlet oxygen quantity [372, 373]. The probability for emission of a luminescent photon is small hence the signal will be weak. In addition, the lifetime of the transition is short due to the rapid interaction between singlet oxygen and tissue substrates. Hence quite sophisticated instrumentation is required. Typically, a pulsed laser emitting a short laser pulse excites the singlet oxygen whereas a sensitive NIR-photomultiplier tube (PMT) detects the signal after spectral filtering [374]. The measurements are performed using fiber optics although images can be achieved through raster scanning the point source and detector [375]. Recently the direct dosimetry

model was demonstrated to correlate with erythema and edema in healthy volunteers following ALA-PDT [376].

6.2.3 Implicit dosimetry

Instead of detecting the singlet oxygen directly, measurements can be performed where the measurable is affected by singlet oxygen. In the case of Type II-reactions the singlet oxygen will oxidize the photosensitizer in addition to the target tissue. The effect is called photobleaching, where the concentration of the photosensitizer decreases. Ample amount of work has been devoted to the development of models describing the bleaching kinetics, both mediated by singlet oxygen and photosensitizer triplet state [377]. The experimental work is mainly performed on cell spheroids [339], but pre-clinical animal studies have also been reported [378, 379].

Photofrin has been shown to undergo two kinetic mechanisms, one mediated by singlet oxygen and one mediated by triplet state reactions with tissue cells. The former is more pronounced at higher concentrations whereas the latter occurs in case of low concentration [378, 380].

ALA-induced PpIX-bleaching depends on the concentration in an intriguing way [381]. It was suggested, that the drug would localize to different targets when concentration was altered. In addition when bleaching is mediated by singlet oxygen, PpIX form photoproducts [382]. These are photodynamically active hence will contribute to the PDT outcome in a non-predictable way. Hence it is questionable if ALA-PpIX is an appropriate candidate for implicit dosimetry [383].

It has been reported that mTHPC is mainly bleached by singlet oxygen [93]. Hence, the response may be predicted using a dose metric based on bleaching kinetics [384]. In order to provide a theoretical model of the interaction between light, drug and oxygen, describing the bleaching process, ideally the kinetic rate equations should be considered. These equations model the rate of energy-transfer between photosensitizer ground state, excited state, triplet state, oxygen levels and tissue target. A rigorous derivation is given in e.g. [378].

A simplified case is reached when omitting photobleaching due to photosensitizer triplet state reactions. Thus, only bleaching kinetics mediated by singlet oxygen is described. The temporal change of the photosensitizer concentration, $[S_0]$, is then given by [377]

$$\frac{d[S_0](\mathbf{r}, t)}{dt} = -k_{os}[S_0](\mathbf{r}, t)[^1O_2](\mathbf{r}, t). \quad (6.2)$$

k_{os} is the rate of interaction between singlet oxygen and the photosensitizer. Through rearrangement and integrating over the treat-

ment time, the implicit dose metric is defined by

$$D_{\text{ps}} = \int_0^T \frac{[{}^1\text{O}_2](\mathbf{r}, t)}{\tau_{\Delta}} dt = -\frac{1}{\tau_{\Delta} k_{os}} \int_{[S_0](0)}^{[S_0](T)} \frac{d[S_0](\mathbf{r}, t)}{[S_0](\mathbf{r}, t)}. \quad (6.3)$$

Integration of the equation above yields

$$D_{\text{ps}} = \frac{1}{\tau_{\Delta} k_{os}} \ln \left(\frac{[S_0](\mathbf{r}, 0)}{[S_0](\mathbf{r}, T)} \right). \quad (6.4)$$

Dysart et al. proposed that an effective minimum concentration should be included in Equation (6.4) [384]. The reasoning behind this was that bleaching may be independent of photosensitizer concentration when the drug level is low. Singlet oxygen is generated close to the photosensitizer molecule and subsequently diffuse to the site where the oxidation of a substrate, or drug molecule occurs. The diffusion length is short, in the order of tens to hundreds of nm [385]. When the photosensitizer concentration is low, the distance between drug molecules might be longer than the diffusion length. Hence, when a singlet oxygen molecule is generated there is only one photosensitizer molecule, i.e. the parent molecule, within the diffusion range. This effect is pronounced for drug concentrations below the effective minimum concentration, denoted δ [380]. The implicit dose metric for the case of low photosensitizer concentration then becomes [384]

$$D_{\text{ps}} = \frac{1}{\tau_{\Delta} k_{os}} \ln \left(\frac{[S_0](\mathbf{r}, 0) + \delta}{[S_0](\mathbf{r}, T) + \delta} \right). \quad (6.5)$$

Equations (6.2)-(6.5) render a theoretical framework for the calculation of the singlet oxygen dose even when the oxygenation and the light fluence rate change during therapy [386].

6.2.4 Explicit dosimetry

The most common approach is to use explicit dosimetry [76]. The model relies on explicit assessments of the three components responsible for inducing the photodynamic action, i.e. fluence rate, photosensitizer and tissue oxygenation.

The ability to control the irradiation and the drug quantity administered to the patient motivates the definition of a dose metric according to Equation (6.6). Considering a volume element, positioned at \mathbf{r} within a medium, the *PDT-dose* is given by

$$D_{\text{pdt}}(\mathbf{r}) = \int_0^T \varepsilon_{S_0} [S_0](\mathbf{r}, t) \Phi_x(\mathbf{r}, t) dt. \quad (6.6)$$

As before the spatially dependent drug concentration and treatment light fluence rate are denoted $[S_0](\mathbf{r}, t)$ and $\Phi_x(\mathbf{r}, t)$ respectively. ε_{S_0} is the extinction coefficient at the treatment wavelength for the photosensitizer. This dose metric assumes non-limiting oxygen availability.

If variation of the photosensitizer concentration is neglected, both spatially and temporally, a dose metric can be defined that only relies on the light fluence. The *Fluence-dose* is given by

$$D_{\text{flu}}(\mathbf{r}) = \int_0^T \Phi_x(\mathbf{r}, t) dt. \quad (6.7)$$

This dose metric also assumes non-limiting oxygen availability.

Within the explicit dosimetry model, the threshold dose is given by the PDT- or Fluence-dose required to induce the minimal amount of singlet oxygen leading to cell necrosis. In order to assess if the threshold dose is reached several alternatives exist that estimate the light fluence, photosensitizer concentration and oxygenation of the tissue.

Fluence-rate assessment can be made using calibrated optical probes where the signal, integrated over treatment time, yields the Fluence-dose [387, 388]. Such point-measurements are valuable for yielding representative values of the delivered light dose in one location. In order to render a spatial map of the fluence rate throughout the entire target volume, model-based approaches must be considered. The procedure is then to quantify the optical properties followed by calculation of a forward model.

Within the scope of interstitial PDT, the optical properties are typically evaluated through steady-state spatially resolved protocols [389–391] and Paper VI. Here a homogeneous distribution of μ_a and μ'_s is assumed. In recent years heterogeneous models have been reported utilizing tomographic schemes similar to the discussion presented in Section 4.4. Wang et al. adopted a translatable detector fiber within the prostate collecting light at different distances from a steady-state light source [392]. Several reports have been published where the optical fibers delivering and collecting light are placed transrectally. Reconstruction of the optical properties are then made using prior structural information from ultra-sound [393, 394] or MRI [395]. Due to the risk of rectal wall damage, using fibers for transrectal PDT treatment is not an option, but approaches such as these could render interesting means for monitoring treatment progression with minimal invasiveness. The capability is still to be verified *in vivo*.

Following the evaluation of optical properties, the forward model yields the fluence rate throughout the medium. Within interstitial PDT dosimetry development of a wide variety of forward models have been reported. For example; accelerated Monte-Carlo

methods [156], higher order approximations to the RTE [396, 397], FEM-models [398] and semi-homogeneous models of the diffusion equation [399] and Paper **VI**.

The calculation of fluence-rate in every location within the target volume is inherently connected to *pre-treatment planning*. The problem at hand is to tailor the light distribution so that the whole target volume receives a Fluence-dose above threshold. In addition to the treatment time the parameters to optimize are positions, shape and power for the light sources [398, 400–402]. The pre-treatment, as well as real-time, dosimetry adopted within the work of this thesis will be further discussed in Section 6.4.

Photosensitizer assessment can be achieved either through absorption [389] or fluorescence [101] measurements. The drug uptake in the target volume can vary between individuals as well as within each individual. In order to compensate for differences in photosensitizer accumulation, Zhou et al. compensated the light delivery time based on pre-treatment point measurements of photosensitizer fluorescence [88]. This approach rendered less variation of PDT-response between individuals relative Fluence-dose only.

In addition to the pre-treatment dosimetry, the photosensitizer can be quantified during the treatment. Since the drug is often subject to photobleaching the drug concentration, available for inducing photodynamic action, dynamically decreases [356]. Sheng et al. reported on improved treatment prediction following ALA-PDT when relying on the calculation of an "effective dose". Here the PDT-dose was calculated only within time windows when rapid photobleaching was present [379].

Pursuing a model-based approach the photosensitizer needs to be quantified throughout the target volume as function of treatment time. In Paper **VIII** a scheme for three-dimensional drug reconstruction is presented and will be further discussed in Section 6.5.

Tissue oxygenation refers to the molecular oxygen present in the tissue. It can be assessed through the oxygen partial pressure (P_{O_2}) using electrodes [403]. The P_{O_2} is related to the oxygen carried by hemoglobin through the oxygen-hemoglobin dissociation curve [58]. As presented in Section 2.2 the absorption spectra for oxy- and deoxy-hemoglobin are different, hence oxygen saturation can be assessed with optical techniques [345]. The oxygenation level is of ample importance to monitor during treatment since hypoxia will limit therapeutic outcome [404].

As seen in Equations (6.6)-(6.7), the oxygenation is not explicitly incorporated in any of the dose metrics. A theoretical model describing the oxygen consumption during PDT and the oxygen re-perfusion from a blood vessel has been presented [343, 405].

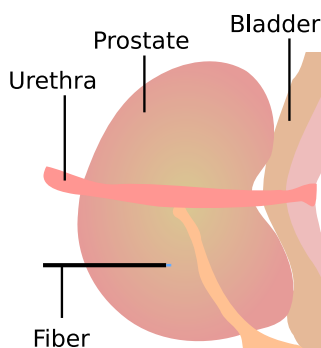


Figure 6.2. Schematic picture of the prostate anatomy.

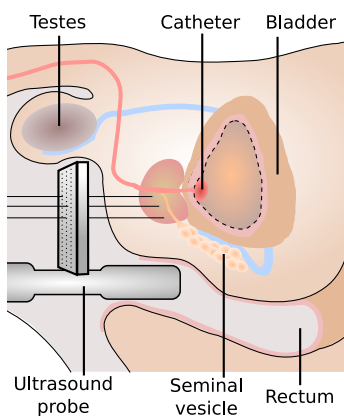


Figure 6.3. Schematic picture of the transperineal treatment route.

Although this rigorous mathematical model provide means to analyze the inter-dependencies in the photodynamic pathway it relies on the knowledge of vascular density which potentially is hard to assess *in vivo* [405].

6.3 PDT for prostate cancer

Photodynamic therapy of the prostate was first reported by Windahl et al., in 1990, who successfully treated two patients with localized tumors using Photofrin [406]. More than a decade later the safety and feasibility was investigated for prostate-PDT governed by ALA-induced PpIX [407]. 14 patients underwent transurethral or transperineal IPDT, see Figure 6.3. The treatment did not target the whole gland but, despite this, lowered PSA values were evident at follow-up 6 weeks post-treatment.

Nathan et al., at University College London, was the first to report on mTHPC-mediated PDT of the prostate [408]. 14 prostate cancer patients with local recurrence after radiotherapy (biopsy proven) were treated three days after administration of the drug. The treatment was performed transperineally using bare-end optical fibers that was translated to multiple sites. In 9 patients PSA levels decreased compared to pre-treatment. Contrast-enhanced MRI, within the first week post-treatment, showed that 91% of the prostate cross-sections were necrotic. Side-effects included incontinence and impaired sexual function.

Moore et al., also at University College London, later continued the work on mTHPC-PDT now applied to untreated local prostate cancer in 6 patients [409]. A total of 10 treatments were performed using the same approach as above. 8 out of 10 treatments resulted in PSA reduction ranging from 14-67% relative pre-treatment level. MR investigations showed patchy areas of reduced enhancement in some patients. Others had more distinct features of devascularization, potentially indicating necrosis. Due to oedema and inflammation the prostate volume increased by approximately 30%, assessed within the first week. The volume then decreased, 2-3 months post-treatment, to about 30% relative base-line volume. Complications following PDT were irritative voiding symptoms that resolved after 4 months. Furthermore the skin photosensitivity after therapy, caused by prolonged retention of mTHPC, rendered a requirement to limit light exposure to the skin within the first week. Since this was a trial study no efforts were made to ablate the whole prostate and consequently all patients had viable tumor cells in biopsies after treatment. The authors conclude the safety and capability, of mTHPC-PDT, to induce necrosis but also enlighten the need for dosimetry in order to destroy all glandular tissue.

Du et. al. and Verigos et al., at University of Pennsylvania, presented a study where Lutex was administered to patients with

localized recurrent prostate cancer after radiotherapy [328, 410]. The primary goal of the trial was to assess the maximally tolerated dose of Lutex-PDT using 732 nm treatment light. Time between drug administration and treatment commencement varied between 3 and 24 hours. In addition a vast arsenal of investigations were employed including measurements of optical properties [390], fluorescence spectroscopy of photosensitizer [101] and optical assessment of tissue oxygenation [404]. The measurements were performed by translatable spherical diffuser fibers where the light fluence rate could be measured directly. 16 patients underwent PDT using cylindrical fibers implanted transperineally. With the highest PDT dose, PSA levels increased shortly after therapy although returning to base-line within 1-2 months. At lower PDT doses no impact on PSA was evident. The only complications reported were that some patients experienced temporary urinary retention after the procedure. After two years all patients had increased PSA levels. The optical measurements performed pre-, during and post- treatment all indicated substantial heterogeneity of optical properties and photosensitizer accumulation. Tissue oxygenation was relatively constant for each patient but the total hemoglobin concentration decreased during treatment. The conclusion of the study was that even though the mild and transient complications render an attractive alternative to prostate cancer therapy, the optical heterogeneity of the prostate must be taken into account for proper light delivery.

In a subsequent report, from the same group, Patel et. al reported on short and long term effect on PSA levels relative the PDT dose [411]. This dose was defined as the product of the photosensitizer concentration, measured pre-treatment *ex vivo*, and the *in situ* measured light dose. Patients receiving high-dose PDT experienced a delay (82 days) to the time-after-treatment when the PSA levels began to irreversibly increase relative low-dose PDT patients (43 days).

This group has also developed a pre-treatment dosimetry software intended to optimize parameters such as cylindrical-fiber positions and lengths as well as irradiation power in order to tailor the emitted treatment light according to a predefined doseplan [400].

Trachtenberg et. al. reported on vascular targeted photodynamic therapy (VTP), using escalating drug-doses of the photosensitizer WST09 [326, 327]. Within this trial 28 patients with recurrent prostate cancer after external beam radiation were treated. Cylindrical fibers were used for light delivery to the whole gland 20 min after drug administration. Spherical isotropic probes for fluence rate measurements at selected sites [389]. Complete response was achieved in 60% of the patients who received high-dose PDT, based on one-week post-PDT MR investigation that showed avascular areas [371]. Biopsies from these patients showed no viable cancer after 6 months. Complications such as rectourethral

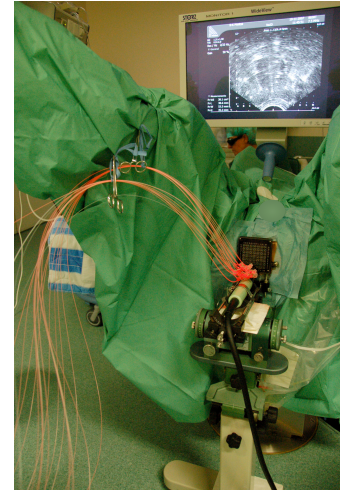


Figure 6.4. Patient positioned in lithotomy position during PDT.



Figure 6.5. Instrument for prostate-PDT.

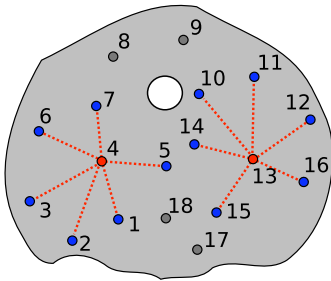


Figure 6.6. Schematic picture showing a transversal slice of the prostate. The dots are fibers within two monitoring regions where red dots are sources and blue dots are detector fibers.

fistulae, in two patients, and decreased urinary function in patients with a response to PDT were reported. The evaluation employed a dosimetry planning software described in [398]. The interpatient variability of the photosensitizer pharmacokinetics, i.e. photosensitizer distribution as a function of time, and variability in tissue sensitivity to WST09-VTP were postulated as potential causes for incomplete response in patients receiving high-dose PDT.

6.4 Rationale for prostate-PDT

The current instrumentation and procedures for interstitial photodynamic therapy in Lund is presented within this section. The instrument has evolved over the last decade and previously published reports on the progress can be found in [412–414].

6.4.1 Instrumentation

The instrument, seen in Figure 6.5, operates in either of two modes; *light delivery* or *monitoring*. A maximum of 18 external optical fibers can be employed to deliver and collect light from the patient tissue. These sterile fibers are referred to as *patient fibers*. Light delivery is governed by 18 fiber-coupled diode lasers calibrated to emit 150 mW at 652 nm. Switching between the two modes is accomplished by a mechanical switch. In monitoring mode light is delivered through one patient-fiber while six neighbouring fibers can collect the photons propagating within the tissue. The collected light is then routed to six spectrometers, one per detector-fiber. When in monitoring mode the switch is turned sequentially so that all fibers can act as sources, thus different fibers will take the role as detectors, see Figure 6.6. The monitoring is performed using three light sources; a similar diode laser as used in treatment mode, a light emitting diode (LED) emitting NIR-light in the interval 750–850 nm and lastly a blue LED at 410 nm. Following the discussion in Section 6.2.4 about explicit dosimetry it should be clear that the intent is to monitor fluence rate at the treatment wavelength, oxygenation through spectroscopic measurements and fluorescence from the photosensitizer. The blue LED measurement is only performed before treatment where a single fiber delivers and collects the light [415]. In the case of mTHPC the fluorescence measurements and fluence rate measurements are performed simultaneously since mTHPC emits fluorescence around 710 nm when excited by 652 nm, seen in Figure 2.3.

6.4.2 Procedure

When the instrument is applied in clinic the procedure shown in Figure 6.7 is followed. The scheme is adopted from brachytherapy where radioactive seeds are placed inside the prostate. A brief

overview will be given here based on Paper VI. The protocol enables control of light delivery time during the treatment and was given the name Interactive DOSimetry by Sequential Evaluation, hence the acronym IDOSE.

(i) *Ultrasound*

The patient is positioned in lithotomy position, seen in Figure 6.4 and a transrectal ultrasound (US) investigation is done. Here transversal images are acquired starting at the deepest position and subsequently stepping the US-probe outwards. In each image slice the prostate, urethra, rectum, cavernous nerve bundles and sphincters are delineated by the urologist.

(ii) *Render 3D-model*

The US-images, typically 8-10 slices, are used to render a 3D-model of the anatomy. A cube of size $60 \times 60 \times 60$ voxels is created where each voxel (1 mm^3) is given a number indicating tissue type.

(iii) *Calculate fiber-positions*

The 3D-model is used as input for an algorithm that renders relevant positions for the patient fibers. In order to deliver light to the whole target volume it is of ample importance that the fibers are positioned to enable this. A random-search algorithm, described in [414], that repeatedly samples new fiber positions is executed. The algorithm uses default homogeneous optical properties when it tries to maximize the fluence rate delivered to the target volume while minimizing the fluence rate to surrounding organs-at-risk. Briefly every voxel is given a weight that is positive for the target voxels otherwise negative. For every randomized fiber configuration the analytical Green's function, Equation (3.26), yields the fluence rate throughout the volume. Summation of the voxels with lowest fluence rate within the target volume and the voxels outside the target volume with the highest fluence rate will optimally yield a high "fitness-value" when incorporating the weights. The algorithm is given about 10 minutes to find a fiber configuration with the highest fitness-value.

(iv) *Insert fibers*

The fibers are put in place by the urologist through thin needles. Since the fiber positions can deviate from the theoretically retrieved, the positions are updated in the dose-planning software. This is done through a transrectal US-investigation. The fibers are positioned so that number 1-9 is placed at positions in one lobe of the prostate while number 10-18 is placed in the other lobe, indicated in Figure 6.6.

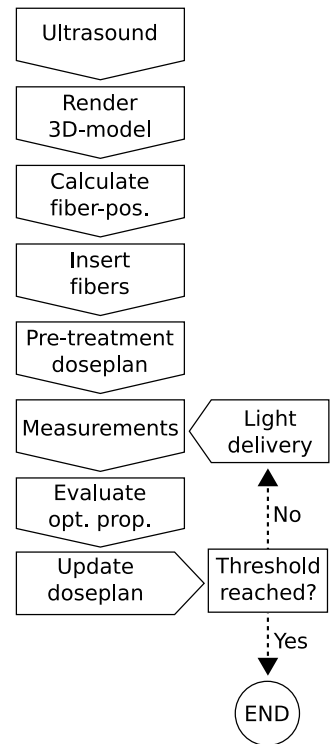


Figure 6.7. A flowchart depicting the treatment procedure.

(v) *Pre-treatment doseplan*

The doseplan states how long time every fiber should deliver light. The algorithm is based on the explicit light fluence dose, seen in Equation (6.7), and presented in Paper VI. Briefly the scheme optimizes the light delivery time, t_i , for each fiber, i , so that

$$L_j \leq \sum_{i=1}^{18} t_i \Phi(\mathbf{r}_i, \mathbf{r}_j) \leq U_j \quad (6.8)$$

where $\Phi(\mathbf{r}_i, \mathbf{r}_j)$ is the fluence rate in voxel j due to a source positioned at \mathbf{r}_i . L_j and U_j denote lower and upper bounds of the light dose relevant for voxel j . The bounds are specific for each tissue type. For the target tissue the lower bound is the threshold dose whereas the upper bound is infinite. Furthermore the surrounding organs are assigned zero as lower bound and the threshold dose as upper bound. In addition each tissue type is assigned a weight that characterize the specific sensitivity to the light dose. In practice a higher weight renders higher sensitivity leading to diminished light dose to the organs. The effect of changing the weight parameters on delivered dose was investigated for the rectum in Paper VI. The optimization is performed by iteratively updating each t_i until Equation (6.8) is satisfied or a predefined maximum number of iterations is reached [416].

The algorithm requires the calculation of the fluence rate when executed. Since one aim in Paper VI was to present a method that was capable of on-line dosimetry, i.e. executed during treatment, the computational time had to be restrained. The analytical solution to the diffusion equation, see Equation (3.26) was adopted. When executed before treatment default optical properties are used given by $\mu_a = 0.05 \text{ mm}^{-1}$ and $\mu'_s = 0.87 \text{ mm}^{-1}$, adopted from [199].

(vi) *Measurements*

Measurements are performed sequentially as described above for laser light and NIR-LED. When fiber i acts as source the measurements are performed using fibers $i \pm 1, i \pm 2, i \pm 3$. In reference to the discussion about sensitivity, in Section 4.4.3, the photons will predominantly probe the volume around source and detector fibers, here called a *measurement domain*.

(vii) *Evaluate optical properties*

In each measurement domain the optical properties are assumed homogeneous. Utilizing the spatially resolved scheme, presented in Section 4.3.1, the effective attenuation coefficient can be assessed and assigned to each source fiber. This

approach yields a semi-heterogeneous representation of the medium. The source-detector distances within a domain are typically 10-35 mm (for prostate volumes smaller than 40 mm³). Measurement signals are omitted when the signal-to-noise ratio (SNR) falls below a predefined threshold. In the case where too many measurements are subject to low SNR, measurements from neighbouring domains are included in the evaluation. In order to calculate μ_a and μ'_s from μ_{eff} a default value for the reduced scattering coefficient is used.

(viii) *Update doseplan*

The treatment time is updated based on the evaluated optical properties using the same algorithm as in *Pre-treatment doseplan*.

(ix) *Light delivery*

The instrument is switched to light delivery mode and the patient fibers emit light into the target volume. The irradiation is halted at 2, 4, 9, 14, 19, 29 (and every 10:th minute after that) in order to perform measurements. This scheme allows on-line tracking of parameters that might change during treatment. The closer intervals in the beginning of the session was chosen in order to track rapid bleaching kinetics.

(x) *Repeat until done*

The loop continues until the threshold dose is reached.

Threshold dose

A threshold dose for mTHPC-mediated prostate-PDT was estimated based on a previous study by Moore et al. [409]. Relying on their data a spherically shaped volume of necrosis was assumed around each fiber. The radius of necrosis was assessed to be 7 mm on average. The fluence rate was calculated using optical properties, of $\mu_a = 0.06 \text{ mm}^{-1}$ and $\mu'_s = 1 \text{ mm}^{-1}$ adopted from [199] employing the analytical solution to the diffusion equation, see Equation (3.26). With an averaged treatment time of 5 min per fiber the calculated threshold dose was 8.5 J/cm². A conservative approach was chosen so the threshold dose used for subsequent studies were set to $D_{\text{threshold}} = 5 \text{ J/cm}^2$.

System validation

A phantom study was performed, presented in Paper VII, with the aim to investigate the instrument's capability to evaluate optical properties and subsequently deliver a predefined dose to a target volume. The optical phantoms, seen in Figure 6.8a, were made of liquid Intralipid[®] (Fresenius Kabi), ink (Pelican fount) and water, hence yielding homogeneous optical properties. The

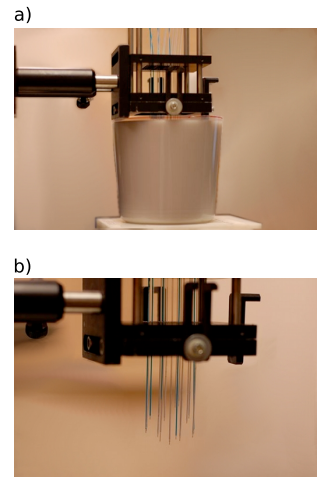


Figure 6.8. a) The optical phantom setup. b) The fiber configuration.

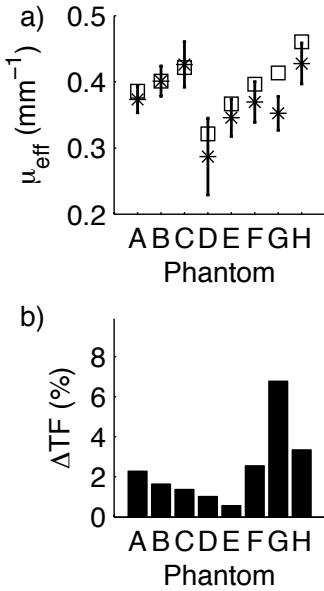


Figure 6.9. a) The averaged effective attenuation coefficient assessed with IPDT-instrument (*) and Time-of-Flight instrument (\square) for each phantom A-H. The errorbars depict ± 1 standard deviation. b) The resulting effect on delivered dose when comparing IPDT- and TOF-evaluated optical properties.

ink and intralipid content of the phantoms was altered in order to render different scattering and absorption properties. The fiber configuration, seen in Figure 6.8b, was based on a prostate geometry from a previous US investigation. As reference the optical properties were assessed using a time-of-flight spectroscopy system (TOF) [199].

The evaluated effective attenuation coefficient for each phantom is shown in Figure 6.9a for the time-of-flight system and the IDOSE scheme. The slight underestimation will cause an alteration of the volume that receives the threshold dose, referred to as the treatment fraction. The relative change of the treatment volume, denoted ΔTF , between TOF- and IDOSE- evaluations is shown in Figure 6.9b where it is seen that the treatment fraction changes with less than 10%. In addition the treatment fraction is above 90% of the target volume, in all cases, implying that the underestimation of the optical properties, seen in Figure 6.9a is not critical. This also adheres to the discussion in Paper VI where it was concluded that the dosimetry algorithm is quite insensitive to changes in optical properties and mainly influenced by the volume of the target tissue, fiber configuration and distance to organs-at-risk.

It should be mentioned that the TOF-evaluated optical properties used in this analysis was evaluated using a protocol based on the diffusion equation. Since then the protocol has been refined where the instrument response function is estimated more correctly and the evaluation is based on a Monte Carlo scheme instead [140, 417]. It was reported that using the former TOF-scheme the optical properties were slightly overestimated. Hence the accuracy might be slightly better than what is indicated in Figure 6.9.

The robustness against inaccurately positioned fiber positions was also investigated in Paper VI. The analysis was based on simulated data where fiber positions, as well as optical properties, were allowed to vary. The dosimetry scheme was executed with the simulated data as input and the resulting effect on delivered dose was determined. When the fiber position deviations were sampled from a normal distribution of zero mean and 2 mm standard deviation the effect was at most 7% change of the treatment fraction.

6.4.3 Clinical study

The clinical study, summarized in Paper VII, included patients with histologically proven, untreated, organ confined prostate cancer (stage T1c, Gleason score <7 , PSA <10 ng/ml). The treatments were performed at Malmö University Hospital, Sweden and Karolinska University Hospital, Stockholm, Sweden. Patients were sensitized with mTHPC (Biolitec Pharma) according to the EMEA approved protocol for head and neck cancer, i.e. 0.15 mg/kg given

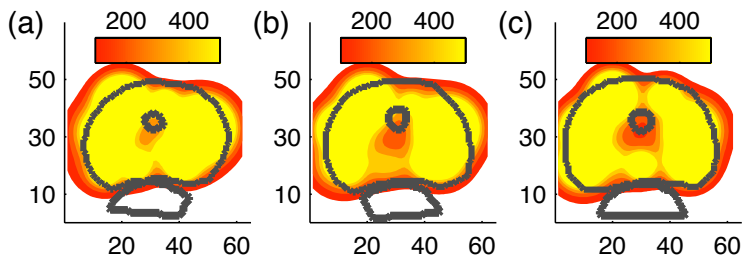


Figure 6.10. Calculated final dose for Patient 2 shown in percentage of threshold dose (5 J/cm^2), for cross-sections a) 15 mm, b) 20 mm and c) 25 mm.

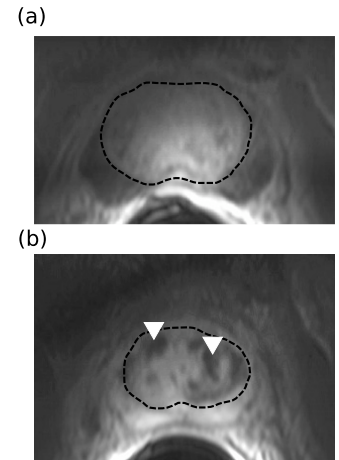


Figure 6.11. MR-images from Patient 2 in a) pre-treatment and b) two weeks post-treatment. The arrows mark zones of reduced enhancement indicated treatment response.

intravenously, and the drug-light interval was 4 days. The intent was to ablate the whole prostate gland by tailoring the light fluence dose using the rationale discussed above.

The post-treatment dose maps, seen for one patient in Figure 6.10a-c, show that the light fluence dose is well above the threshold dose within the prostate volume. In fact a slight overtreatment of the normal tissue close to the prostate gland perimeter is evident. This result arise when the dosimetry algorithm must limit treatment times for fibers close to sensitive organs such as the rectum making other, more distant fibers irradiate longer. In Figure 6.10 it is also seen that the rectum receives a small dose.

Despite the high dose, relative the threshold dose, clinical assessments indicated undertreatment which was also confirmed by viable cancer cells in biopsies, from 3 of 4 patients, taken at a 6-month follow-up. MRI investigations performed before PDT and two weeks after treatment indicated tissue response since a volume decrease of approximately 30% was apparent. Conversely only localized regions of decreased enhancement were seen. This indicate undertreatment. Pre- and post-treatment MR images are shown for one patient in Figure 6.11a and b respectively.

In Paper VII it was concluded that the reasons for undertreatment were due to a too low threshold dose and heterogeneities that attenuate the output power from the treatment lasers, reducing the delivered light dose. A detailed discussion about these factors are included hereafter.

Investigation of the threshold dose

The determination of the threshold dose, discussed in Section 6.4.2, relied on several assumptions about the optical properties and the necrosis radius from previous studies. A too low threshold dose

implies that the assumed value for the absorption coefficient is too high (data not shown) whereas the assumed value for the scattering coefficient seems to have little effect on the threshold dose determination (data not shown). Evidently, a more detailed threshold dose analysis should be performed where the necrosis and optical properties are assessed from the same individual.

An animal study, comprising healthy male beagles, was performed in collaboration with Department of Clinical Sciences, Swedish University of Agricultural Sciences, Uppsala. The objective was to evaluate the tissue response after interstitial PDT of the prostate in a light-dose escalation study. The animals, aged 15-33 months and weighing 14-20 kg, were divided into 3 groups (3 dogs in each group). The first group underwent interstitial PDT where each fiber delivered a fixed dose of 63 J, thus omitting feedback dosimetry. The other two groups were subject to treatment feedback with predefined threshold doses of 10 and 20 J/cm². The instrument was adapted to the canine prostate where only seven light delivery fibers were deemed sufficient to irradiate the whole glandular volume. mTHPC was administered intravenously (0.15 mg/kg) 72 hours before treatment.

Treatment assessments, performed on prostate as well as adjacent tissues, included MRI seven days after PDT as well as pathology and histological examinations. Blood sampling, for determination of the plasma levels of mTHPC, was performed at several times after drug administration.

The post-treatment results from group 1 (fixed light dose) showed changes that were scattered often extending outside the prostate gland. Hemorrhages were in some cases present in the rectum, bladder as well as connective tissue surrounding the prostate. This was also confirmed by MRI where regions with signal void, indicating treatment response, were irregular and diffuse throughout the prostatic capsule. Isodose plots, of the calculated light fluence, were compared with the diameters of the necrotic lesions to establish the dose level that caused necrosis. This analysis rendered an estimated threshold dose level of 20 to 30 J/cm².

The response in dogs within group 2 (10 J/cm²) were more focused to the prostate, compared to group 1. No changes were seen in rectum or bladder. In the prostate there were several foci of necrosis with sizes ranging from a few mm to 8 mm. MRI confirmed signal void in irregular regions within the prostate. Dose calculations again indicated a threshold dose between 20 to 30 J/cm².

Two dogs in group 3 (20 J/cm²) had extensive necrotic lesions that covered the entire gland in the central slices. Haemorrhages and ulcerations was seen in urethra, rectum and bladder. In the prostate there were marked changes. In the central slices there were necrotic lesions ranging from several mm to almost total necrosis in one slice. MRI showed multiple areas of signal void in

the prostatic tissue. The sizes of the necrotic lesions, covering the entire gland in the central slices, were consistent with a threshold dose of 20-30 J/cm². The third dog evidenced minor necrotic lesions in the prostate. This dog had a substantially smaller prostate compared to the other subjects.

No changes were seen in a control dog that was subject to mTHPC administration and needle placement, i.e. no light.

It should be noted that the necrotic changes are irregular in shape most likely owing to physiological changes in the tissue. In addition the correlation between the US-guided light fluence calculations and pathology, or MRI, is complex due to lack of distinct landmarks. There is always a large zone of haemorrhaging and inflammation surrounding the necrosis. It not clear how these changes develop over longer time. Further studies with longer follow-up time are needed to address this.

In conclusion the canine study verified that the IDOSE rationale renders confinement of the treatment to the prostate gland. Furthermore, the threshold dose in healthy canines is estimated to be within 20-30 J/cm².

Investigation of attenuating heterogeneities

The other, presumed, reason for undertreatment is heterogeneities perturbing the fiber output power. These include local blood absorbers in front of the fibers as well as tissue regions with heterogeneous optical properties. The resulting effect is that the fluence rate will be diminished hence lowering the delivered dose to the target volume. In addition, when adopting optical measurements, heterogeneities also perturb the evaluated optical properties.

A simulation study was performed, in order to assess the effect on treated volume, where the fiber-specific attenuation was assumed to be spherical and centered at the fiber-tip, further discussed in Appendix D.1. The results show that the simulated local absorbers at the fiber tips render a 5-50% decrease in the treated volume. The delivered light fluence is well above threshold within the prostate, as seen in Figure 6.10, which alleviates the effect of local absorbers to some extent. On the other hand the treatment fraction does not take local changes into account. Evidently a fiber with high attenuation will not contribute to the total dose resulting in local undertreatment. Hence, heterogeneities should be assessed in addition to the optical properties to enable local control of the dosimetry.

One approach towards this goal is discussed in Appendix D.1. The conclusion of this discussion is that steady-state measurements, in one spectral band, might be a too simple tool to estimate optical properties at the same time as local absorbers in front of the fibers and heterogeneities. Instead a scheme including multispectral measurements is proposed to remedy the problem.

6.5 Towards photosensitizer dosimetry

The dosimetry rationale above adopts the explicit light fluence dose, defined by Equation (6.7), where the photosensitizer distribution is assumed to be temporally and spatially invariant. As discussed before a better approach would be to incorporate the drug concentration. When interstitial PDT is employed the quantification of the drug is required in every voxel of the volume under study.

Paper **VIII** presents an approach for tomographic photosensitizer reconstruction based on measurements from the IPDT-instrument described before. The inverse model is based on the the scheme presented in Section 4.4 with the normalized Born measurable, Section 4.4.3. By scaling the fluorescence emission with the excitation light the measurable effectively becomes insensitive to local absorbers in front of the fibers. In addition the Born ratio has been shown to render feasible reconstruction results in optically heterogeneous media despite the use of a homogeneous forward model [220]. In the implementation in Paper **VIII** the background optical properties were based on the treatment measurements and averaged throughout the entire prostate volume.

The positioning of the fibers inside the probed volume increases the ill-posedness of the problem since singular values arise close to the fiber-tips, inherited from the calculation of the diffusion equation. In order to alleviate this problem a Monte Carlo-scheme has been implemented that simulates the photon migration more accurately close to each fiber [152]. The MC-simulation results are then interpolated into the FEM-solution of the DE. In addition the regularization matrix in Section 4.4.5 is used, practically confining the solution to the prostate. Furthermore the use of a reconstruction basis that is coarse, as compared to the mesh for the forward model, also limits the ill-posedness. On the other hand both the regularization matrix and the coarser reconstruction basis render spatial smoothing of the reconstructed solution, hence the expected spatial resolution is moderate.

6.5.1 Explicit photosensitizer reconstruction

The feasibility of interstitial fluorescence tomographic imaging was investigated in a liquid phantom study, further discussed in Paper **VIII**. The intent was to investigate whether it was possible to reconstruct a spatially varying fluorophore distribution employing the interstitial setup as used in the clinical study. Liquid phantoms were used where a container, outlined in Figure 6.12a-b, was inserted. The fluorophore concentration of both the bulk and container was changed in order to mimic fluorophore bleaching (although linear variation was adopted). The true fluorophore absorption coefficient is seen for each measurement run in Fig-

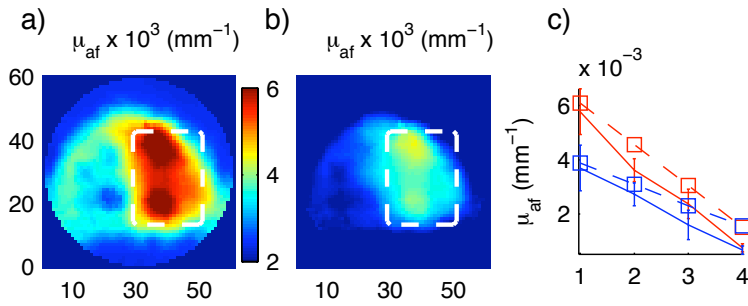


Figure 6.12. The reconstructed fluorophore coefficient from a phantom experiment for a) first measurement run and b) second measurement run. In c) the reconstruction results from all four measurement runs where μ_{af} is averaged within each compartment. \square denote true fluorophore absorption coefficient for the small compartment (red) and the bulk compartment (blue)

ure 6.12c. The reconstructed results for measurement run 1 and 2 are seen in Figure 6.12a and b, respectively. In Figure 6.12c the average values for bulk and container are seen for all measurement runs.

The reconstruction scheme has evolved during the last year and the main difference between the rationale used to render the results presented in Figure 6.12 and Paper **VIII** are summarized below.

- (i) A Monte-Carlo simulated source representation is used.
- (ii) A regularization matrix spanning only the prostate tissue, as opposed to the matrix used in Paper **VIII** where parts of the normal tissue also were included. The confinement to the prostate is what renders the prostate shaped appearance in Figure 6.12a-b.
- (iii) The FEM-mesh holds a higher nodal density hence a slightly more accurate solution to the forward model is retrieved.
- (iv) The spectral band for fluorescence was 710 nm, instead of 690 nm used in Paper **VIII**. This rendered less influence from the intralipid autofluorescence.
- (v) The optical properties, assessed using IDOSE, are interpolated into the FEM-model. In this way a slightly heterogeneous representation of the tissue can be retrieved as opposed to Paper **VIII** where homogeneous optical properties were used. The effect of this alteration is believed to be small when applying the normalized Born measurable [220].

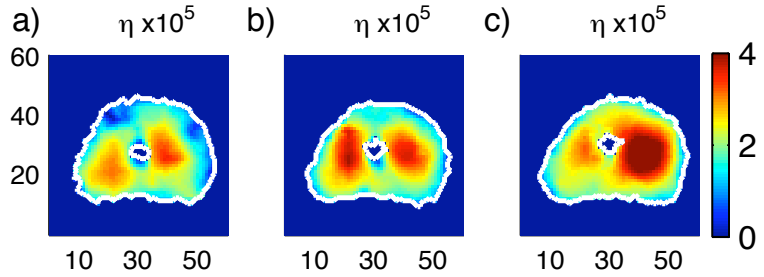


Figure 6.13. The reconstructed fluorophore yield in the prostate of patient 3, shown for cross-sectional slices at a) 15 mm, b) 20 mm and c) 25 mm.

The correspondence between reconstructed values and the true values is improved, as compared to Paper **VIII**. This verifies the feasibility of interstitial tomographic imaging.

In Figure 6.12c the temporal decrease in reconstructed fluorophore is seen for the compartment and the bulk medium. These are averaged values within the assumed prostate region for the compartment as well as the bulk. The fluorophore concentration was changed differently in the compartment relative the bulk medium, indicated in Figure 6.12c. It is seen that the reconstructed values are underestimated by approximately 10-15%. On the other hand, the reconstructed and true μ_{af} follows approximately the same relative variation. The reconstruction method was also applied to measurements performed within the clinical trial. Reconstructions from pre-treatment measurements are seen for three cross-sectional slices, from patient 3, in Figure 6.13a-c. The average fluorescent yield, at pre-treatment monitoring, for patients 1-3 is seen in Figure 6.14. The averaged values are calculated for all voxels within the prostate.

It is seen in Figures 6.13-6.14 that the fluorescent yield in the prostate of is varying. The same findings was reported by Finlay et al.. They estimated heterogeneous appearance of Lutex distribution in the human prostate, using point probe setup [101]. Despite this analogy, Lutex and mTHPC have different binding targets within the cells meaning that a direct comparison might not be feasible. A comment on the higher averaged value for patient 3, in Figure 6.14, is that in this patient the treatment was deemed successful, based on biopsies.

Within the explicit dosimetry model, a dose-metric is formed by including the reconstructions in the calculation of Equation (6.6). This calculation relies on the absolute value of the photosensitizer concentration as well as the explicit light dose. The perturba-

tions, described in Section 6.4.3, are postulated to alter the delivered light dose. They might also play a role in the tomographic imaging of the photosensitizer. Hence, an analysis of the effect of the perturbations on the interstitial tomographic images is given below.

6.5.2 Analysis of reconstruction perturbations

Heterogeneous regions, due to e.g. blood accumulation, will attenuate the excitation and the fluorescence emission. Furthermore, inaccurate fiber positioning can potentially affect the reconstructed results. In order to assess these effects several simulation studies were performed, presented in Appendix D.2 and further discussed below.

When assuming that a local absorber, in front of a detector, is caused by accumulation of blood, the spectral dependence of the transmission through the blood might influence the excitation and fluorescence differently. Excitation will be more attenuated than compared to the emission when transmitted by the local absorber in front of the detector fiber. This difference is a constant and it is independent of occlusion size. The effect is that the absolute quantity will be affected but the detector perturbation will have limited effect on the spatial distribution. Local absorbers in front of sources will have no effect [220].

The analysis shows that a heterogeneous absorption inclusion will cause alterations in measured bulk optical properties. This will in turn cause a decrease in reconstructed fluorophore absorption coefficient. In the simulated setup this error was relatively moderate. Despite this an increase of the error was seen when the absorption coefficient of the heterogeneity was increased. On the other hand the heterogeneity did not affect the spatial distribution of the fluorophore. The main reason behind this result is the normalized Born measurable. Since both excitation and emission are affected by the inclusion the resulting error of the spatial distribution is small. Similar results have been reported in the case of small animal imaging [220].

The model geometry, incorporating one absorption inclusion and one fluorescent inclusion, is evidently simplification of what is expected in reality. Despite this, it allows a comprehensible analysis of the effect, due to one absorbing inclusion, on the photosensitizer reconstruction. Even though one inclusion might seem insufficient, it has a large effect on the measurements of the bulk optical properties. The measurement domains, see Section 6.4, extend throughout a substantial part of the prostate volume. Thus, several domains will experience the perturbation, at least to some extent.

Another case, where the fiber positions were allowed to vary, mimicking inaccurate placement of the fibers, was tested. Here it

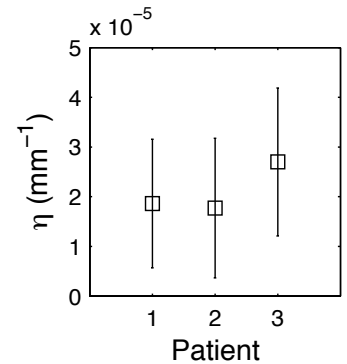


Figure 6.14. Averaged reconstructed η within the prostate for patients 1-3. Error bars mark ± 1 SD of the reconstructed values.

was seen that the spatial distribution was slightly affected. Deviations were approximately within $\pm 10\%$ from the true value. Since the fiber positions are fixed during the treatment, it is expected that the reconstruction of the relative change in photosensitizer concentration is less affected.

In conclusion, local absorbers will cause an effect on the absolute values of the reconstruction while, limited perturbation will occur spatially. Heterogeneous tissue will cause a relatively modest error of the absolute value of the photosensitizer reconstruction but will have negligible effect on the spatial distribution. In addition, inaccurate fiber positions will perturb the spatial distribution slightly.

In order to improve the reconstruction of the absolute photosensitizer concentration, the perturbing effects should be assessed. The key to solving this problem is to assess the heterogeneous bulk optical properties throughout the medium as well as local absorbers. Tomographic imaging of absorption and scattering follows the same approach as presented here, see Section 4.4. Frequency- or time-domain measurements could be implemented, providing means for assessment of both absorption and scattering. Although, this would require major alterations of the instrument. Another setup, that potentially could render information about heterogeneous tissue properties, is steady-state multi-spectral transmission measurements. Utilizing more transmission wavelengths, the simultaneous reconstruction of both absorption and scattering has been shown to be feasible [297]. This would require minor alterations of the instrument. Even though a NIR-LED is incorporated in the instrument today, the measurements are unfortunately subject to low signal-to-noise ratios. A NIR source with higher intensity is then required.

A tomographic scheme will unfortunately prolong the evaluation of the optical properties substantially. Hence, realtime evaluation will be hard to achieve using standard computer equipment. A proposed remedy to this problem could be to use a matrix-free method, such as the one presented in Paper **II**, for the inverse problem. Such an approach would optimally decrease the computational burden both in terms of memory requirements and reconstruction time.

The temporal change of the photosensitizer level was also investigated when the absorption inclusion was present. The simulations intended to reflect a case where the photosensitizer concentration varies during the treatment, correspondingly to bleaching. It was seen, in Appendix D.2, that the absorptive inclusion had a relatively minor effect on the reconstruction of relative changes. Hence, it is motivated to investigate the implicit dosimetry model, see Section 6.2.3, using the previously described reconstruction scheme.

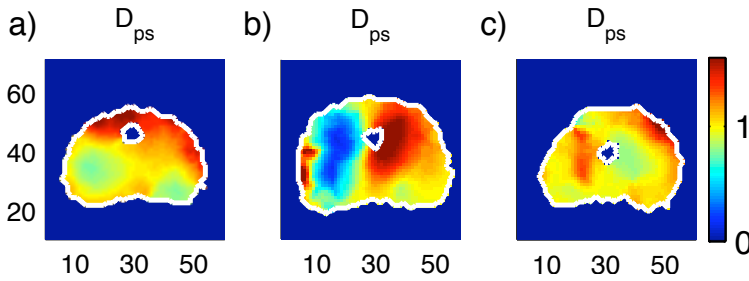


Figure 6.15. The reconstructed implicit dose-metric, shown for transverse plane at depth 21 mm of the prostate, from a) patient 1, b) patient 2 and c) patient 3. The colorbar is in arb. units.

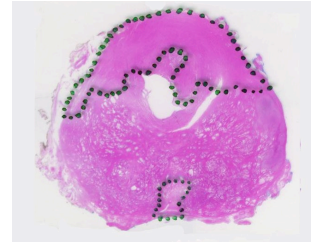


Figure 6.16. A cross-sectional slice from the prostate of patient 1, 12 months post-treatment. Fibromuscular stroma is marked.

6.5.3 Implicit photosensitizer reconstruction

The sequential measurements, performed during treatment, allow tracking of photosensitizer level as well as potential alterations of treatment light transmission. As discussed in Section 6.2.3 the implicit dose model provides a tool for calculation of singlet oxygen concentration based on photobleaching kinetics. Here some initial investigations are presented, where interstitial tomographic imaging governs the implicit dose metric.

In a first approximation, the kinetic rate constants and the effective minimum concentration, defined in the formulation of the the implicit dose metric, are neglected. This means that an approximate solution to Equation (6.4) can be retrieved from the reconstruction results. Tomographic images based on measurements from pre-treatment and post-treatment measurements are employed in Equation (6.4). Performing this calculation for patients 1-3 renders the results, shown for one cross-sectional slice, in Figure 6.15a-c.

Patient 1 underwent prostatectomy 12 months post treatment due to viable cancer cells still present in biopsy. An excised cross-section is shown in Figure 6.16 where fibromuscular stroma is marked, potentially indicating treatment response. The transversal plane of Figure 6.16 and Figure 6.15a are approximately at the same depth. Although it is hard to correlate these two images directly a qualitative analysis can be performed. Both slices show a pronounced treatment effect at the ventral part of the prostate (upper part in the image). This might be due to lower fluence rate at distal parts, leading to more effective oxygen consumption. On the other hand substantial healing has occurred after 12 months rendering limited means to conclude about the feasibility of the implicit dose metric, based on this patient.

For patient 2, the implicit dose metric is shown in Fig-

ure 6.15b. The transverse position of this slice corresponds to the cross-sectional slice from MRI, in Figure 6.11b, two weeks post-treatment. The left lobe (right part from the reader's perspective) in the MRI-slice show reduced enhancement, indicating treatment response. The corresponding region in Figure 6.15b show substantially higher implicit dose as compared to the right lobe of the prostate. This means that the photosensitizer in the left lobe has bleached more rapidly. In these two regions the light dose is approximately the same. Then, the lower dose in the right lobe could be a result of lower oxygen availability, i.e. hypoxia.

The result from patient 3 shows a more uniform bleaching than compared to the other two. The level of the implicit dose metric is approximately the same as patient 1. A higher dose is seen in the peripheral parts of the cross-section.

The dose-metric used here, i.e. Equation (6.4), reveals the relative decrease of photosensitizer between the first and last monitoring session. In the perturbation analysis, see Section 6.5.2, it was deemed that relative reconstructions were less affected by heterogeneities, fiber-specific absorbers as well as inaccurate fiber-positions. Hence there is a certain robustness against perturbations inherited in this method.

The results from patient 1 should be analyzed with care. The prostate was excised 12 months post-PDT, which means that secondary effects such as healing and inflammation have most certainly occurred. As mentioned in the beginning of Section 6.2 such secondary effects cannot be predicted by current dose models. With that said, there is also reason to believe that direct cell death can cause the tissue response seen in Figure 6.16. Such long-term effects is subject for further study.

The implicit dose metric can potentially reveal more information about the treatment since the bleaching kinetics can render valuable means for analysis of oxygen availability. Potentially, this is the case in patient 2. For a deeper understanding of the oxygen-dependent bleaching it would have been desirable to correlate the implicit dose-metric for patient 2 with tissue oxygenation measurements. With an improved NIR source in the instrument, means for such investigations will arise.

The implicit dose metric, applied here, neglected the kinetic rate constants as well as the effective minimum concentration. This renders the fact that quantification of the singlet oxygen deposition is not possible. On the other hand, if the constants are homogeneous within the prostate the spatial variation of the singlet oxygen is retrieved. Furthermore the photosensitizer concentration is assumed to be larger than the effective minimum concentration. For future studies, it is important to define these constants in order to retrieve the absolute values of the dose metric.

In the formulation of the implicit dose metric, in Section 6.2.3, photobleaching was assumed to be mediated by singlet oxygen

only. In the case of PDT utilizing mTHPC it has been shown, in cell spheroid, that this assumption holds [93, 384]. If a more general approach is to be developed, i.e. application of photosensitizers that bleaches through triplet-state reactions in addition to singlet oxygen, a more rigorous theoretical background should be exploited. Such frameworks has been reported, e.g. [378], but so far such schemes have not been applied to the clinical arena.

As bleaching kinetics are inherently complex, much work are yet to be done. The results presented herein, enlighten interesting features of dosimetry based on photobleaching. Thus, future investigations of the implicit dose model aiming towards an implicit rationale for interstitial PDT is indeed motivated.

THE FINITE ELEMENT METHOD

When applying the Finite Element Method (FEM) to solve a partial differential equation in a complex shaped geometry the volume first needs to be discretized. The discretized geometry is called a *mesh* and it is built up by *elements*. The elements, in a three dimensional problem, can take the form of e.g. cubes or tetrahedrons with the common property that the element vertices are defined by *nodes*. The key feature of the FEM analysis is that the problem is considered for each element instead of the whole geometry at once. A complex problem can in this way be reduced to a series of simplified problems. In a discretized geometry with N nodes and E elements the solution to the DE can be approximated by

$$\Phi(\mathbf{r}) \approx \Phi^h(\mathbf{r}) = \sum_{j=1}^N \Phi_j u_j(\mathbf{r}). \quad (\text{A.1})$$

Here $u_j(\mathbf{r})$ is an *interpolation function* for node j . The interpolation function is in the simplest case a piecewise linear function. The piecewise linear interpolation function, for a one-dimensional case, is shown in Figure A.1. These functions have limited support meaning that only nodes connected to the same element are non-zero. Effectively Equation (A.1) means that the continuous solution is approximated by a linear combination of the discrete nodal values within the mesh [127, 160]. The problem at hand is now to find the unknown nodal values Φ_j . In order to retrieve the nodal values it is first noted that if Φ^h is a solution to the DE then it should also satisfy the *weak form* which is formed by multiplying the DE with a test function $v(\mathbf{r})$ and integrate over the entire volume (V), i.e.

$$\int_V v(\mathbf{r}) [-\nabla D(\mathbf{r})\nabla + \mu_a(\mathbf{r})] \Phi^h(\mathbf{r}) dV = \int_V v(\mathbf{r}) q_0(\mathbf{r}) dV. \quad (\text{A.2})$$

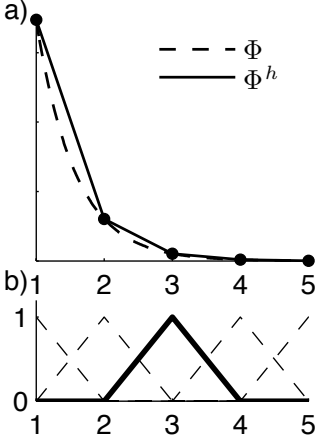


Figure A.1. a) A function $\Phi(x)$ and its discrete approximation $\Phi^h(x)$. b) The interpolation functions where $u_3(x)$ is emphasized.

The leftmost term on the left hand side can be *integrated by parts* and the weak form becomes (the spatial variable notation is here omitted)

$$-\oint_S v D \nabla \Phi^h \hat{n} dS + \int_V D \nabla \Phi^h \nabla v + v \mu_a \Phi^h dV = \int_V v q_0 dV. \quad (\text{A.3})$$

According to Galerkin's method the test function is chosen to be identical to the interpolation function [158, 196]. This means that $v(\mathbf{r}) = u_i(\mathbf{r})$ for node i . In addition substitution of Equation (3.14) in the surface integral yields the FEM formulation for node i ,

$$\sum_{j=1}^N \left(\int_V D \nabla u_j \nabla u_i dV + \int_V \mu_a u_j u_i dV + \frac{1}{2A} \oint_S u_j u_i dS \right) \Phi_j = \int_V q_0 u_i dV. \quad (\text{A.4})$$

The unknown in Equation (A.4) is the nodal values of the fluence rate Φ_j . Taking all nodes into account a matrix equation can be formed according to

$$\left[\mathbf{K}(D) + \mathbf{C}(\mu_a) + \frac{1}{2A} \mathbf{F} \right] \Phi = \mathbf{A} \Phi = \mathbf{Q}. \quad (\text{A.5})$$

The matrix elements are identified in Equation (A.4) and defined by

$$\begin{aligned} \mathbf{K}_{ij} &= \int_V D(\mathbf{r}) \nabla u_j \nabla u_i dV \\ \mathbf{C}_{ij} &= \int_V \mu_a u_j u_i dV \\ \mathbf{F}_{ij} &= \oint_S u_j u_i dS \\ \mathbf{Q}_i &= \int_V q_0(\mathbf{r}) u_i dV \\ \Phi &= \{\Phi_1, \Phi_2, \dots, \Phi_N\}^T. \end{aligned} \quad (\text{A.6})$$

In order to retrieve the fluence rate Φ the matrix system is solved utilizing efficient computation schemes such as Conjugate gradient method or Cholesky decomposition. The $N \times N$ -matrix \mathbf{A} is sparse due to the limited support of the interpolation functions. This means a row i in the matrix will only have non-zero values at nodes connected to the same elements as node i [142]. When the system matrix \mathbf{A} in Equation (A.5) is created it is done in two steps.

First the element matrices \mathbf{K}^e , \mathbf{C}^e and \mathbf{F}^e are constructed. The integration is performed numerically for each element. Secondly all element matrices are *assembled* to form the system matrix. Since every element is treated separately this renders a convenient way of representing heterogeneous tissue optical properties. The source term in the FEM formulation is in practice implemented as an isotropic point source defined on some interior nodes. Alternatively the source can have a spatial distribution according to a Gaussian function [142]. Above the Robin-type boundary condition was inserted without further discussion. It should be mentioned that the surface integral is only defined on the boundary hence only nodes positioned on the boundary are to be included in this integration [418]. Although most FEM schemes adapted to diffuse light propagation follows the formalism described above the inclusion of the boundary condition can be made differently when the source term is described as a boundary flux [127].

LEAST SQUARES MINIMIZATION WITH TIKHONOV REGULARIZATION

The measurements are constructed as a column-vector \mathbf{y}^m . The forward model is given by $\mathbf{y}^c = G(\mathbf{x})$. Adopting Tikhonov regularization, the objective function to minimize with respect to \mathbf{x} is defined by

$$\Omega = \|\mathbf{y}^m - G(\mathbf{x})\|^2 + \lambda \|\mathbf{L}(\mathbf{x} - \mathbf{x}_0)\|^2. \quad (\text{B.1})$$

λ is a regularization parameter, L is a regularization matrix and \mathbf{x}_0 is an initial estimate of \mathbf{x} . Equation (B.1) is minimized, with respect to \mathbf{x} , when $\frac{\partial \Omega}{\partial \mathbf{x}} = 0$ so that

$$\frac{\partial \Omega}{\partial \mathbf{x}} = -2 \left[\frac{\partial G}{\partial \mathbf{x}} \right]^T [\mathbf{y}^m - G(\mathbf{x})] + 2\lambda \mathbf{L}^T \mathbf{L}(\mathbf{x} - \mathbf{x}_0) = 0. \quad (\text{B.2})$$

An iterative approach is adopted, hence for iteration $k + 1$ Equation (B.2) becomes

$$\left[\frac{\partial G}{\partial \mathbf{x}} \right]^T [\mathbf{y}^m - G(\mathbf{x}_{k+1})] - \lambda \mathbf{L}^T \mathbf{L}(\mathbf{x}_{k+1} - \mathbf{x}_0) = 0. \quad (\text{B.3})$$

$G(\mathbf{x}_{k+1})$ is expanded in Taylor series around \mathbf{x}_k . This leads to

$$G(\mathbf{x}_{k+1}) = G(\mathbf{x}_k) + \frac{\partial G}{\partial \mathbf{x}}(\mathbf{x}_{k+1} - \mathbf{x}_k) + \dots \quad (\text{B.4})$$

Higher order terms are omitted in Equation (B.4), practically meaning that the forward model is linearized around \mathbf{x}_k . Insertion of Equation (B.4), the Jacobian $\mathbf{J} = \frac{\partial G}{\partial \mathbf{x}}$ and $\Delta \mathbf{y}_k = \mathbf{y}^m - G(\mathbf{x}_k)$ into Equation (B.3) yields

$$\mathbf{J}^T [\Delta \mathbf{y}_k - \mathbf{J}(\mathbf{x}_{k+1} - \mathbf{x}_k)] - \lambda \mathbf{L}^T \mathbf{L}(\mathbf{x}_k + \mathbf{x}_{k+1} - \mathbf{x}_k - \mathbf{x}_0) = 0 \quad (\text{B.5})$$

Rearrangement leads to the iteration scheme

$$\mathbf{x}_{k+1} = \mathbf{x}_k + [\mathbf{J}^T \mathbf{J} + \lambda \mathbf{L}^T \mathbf{L}]^{-1} [\mathbf{J}^T \Delta \mathbf{y}_k - \lambda \mathbf{L}^T \mathbf{L}(\mathbf{x}_k - \mathbf{x}_0)]. \quad (\text{B.6})$$

MATRIX FREE INVERSE SOLVER

The linear system

$$[\mathbf{J}^T \mathbf{y}] = [\mathbf{J}^T \mathbf{J} + \lambda \mathbf{L}^T \mathbf{L}] \mathbf{x} \Rightarrow \mathbf{z} = \mathbf{H} \mathbf{x} \quad (\text{C.1})$$

can be solved using a GMRES-solver. An outline of the implementation is presented below where the scheme only accounts for one spectral emission band. In addition Matlab-syntax is used, i.e. \backslash denote left matrix division.

- (i) **Calculate forward excitation field**

\mathbf{A}_x and \mathbf{q}_x is the FEM system matrix and source vector for the excitation light, respectively

$$\Phi_x = \mathbf{A}_x \backslash \mathbf{q}_x$$

- (ii) **Calculate adjoint solution**

\mathbf{A}_m is the FEM system matrix for the emission light

$$\Phi_f^+ = (\mathbf{A}_m \backslash \mathbf{y}^m)$$

- (iii) **Calculate \mathbf{z}**

\odot denote element-wise multiplication

$$\mathbf{z} = \Phi_x \odot \Phi_f^+$$

- (iv) **Subroutine executed at each GMRES-iteration \mathbf{k}**

Calculate fluorescent source

$$\mathbf{q}_m = \Phi_x \odot \mathbf{x}_k$$

Calculate forward fluorescence field

$$\Phi_f = \mathbf{A}_m \backslash \mathbf{q}_m$$

Calculate fluorescence measurable

$$\mathbf{y}^c = \mathcal{M}[\Phi_f]$$

Calculate adjoint solution

$$\Phi_f^+ = (\mathbf{A}_m \setminus \mathbf{y}^c)$$

Calculate \mathbf{Hx}

$$\mathbf{Hx} = \Phi_x \odot \Phi_f^+ + \lambda \mathbf{x}_k$$

Return \mathbf{Hx}

- (v) **Continue until projection error is below predefined tolerance**

ANALYSIS OF PERTURBATIONS

D.1 Perturbation of light-fluence dose

As mentioned in Section 6.4.3 heterogeneities and local absorbers in front of the fiber tips are most likely factors perturbing the dosimetry calculations. In order to assess the effect of heterogeneities that perturb the output power emitted from an interstitially placed optical fiber, a simulation study was performed. The main assumption was that the heterogeneity was governed by a spherical blood absorber in front of the fiber tip, see Figure D.1a.

A Monte Carlo model [152] was implemented, according to Figure D.1a where two compartments were assigned different optical properties. For the sphere; $\mu_a = 0.8 \text{ mm}^{-1}$, $\mu'_s = 2 \text{ mm}^{-1}$ and $g = 0.98$ [419] and for the bulk medium $\mu_a = 0.04 \text{ mm}^{-1}$, $\mu'_s = 0.8 \text{ mm}^{-1}$ and $g = 0.9$. The photon migration from the optical fiber, emitted within a numerical aperture of NA= 0.22, was simulated for different sphere radii and analysed at distances within 10-40 mm from the source.

Figure D.1b shows the attenuation for different absorber radii where I is the simulated fluence rate, I_0 is the fluence rate when source is unperturbed, i.e. no blood absorber. The data points in Figure D.1b represent results from Monte Carlo simulations analysed and 10, 20, 30 and 40 mm from source (each point in Figure D.1b is four coinciding points). The linear fit indicate that the attenuation can be described by the modified Beer-Lambert law [29]. Here the the source attenuation is empirically given by

$$T(x) = \frac{I(x)}{I_0} = \exp(-\alpha x) \quad (\text{D.1})$$

where $\alpha \approx 1.89$, rendered from the linear fit in Figure D.1b.

The effect on measured data was assessed by imposing Equation (D.1) on each fiber. The measurable between source s and

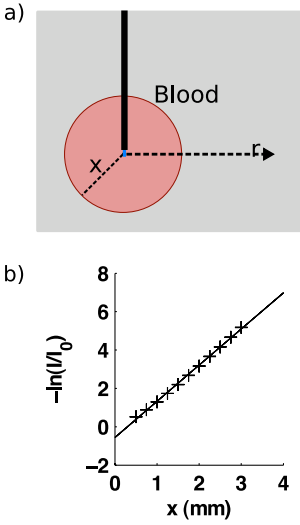


Figure D.1. a) A schematic picture of the modelled local absorber centered at the fiber-tip. b) The attenuation for different absorber radii as simulated using MC (+) and analytically fitted (-).

detector d is then given by

$$\Gamma_{sd} = \frac{P_s \exp(-\alpha x_s) \exp(-\alpha x_d)}{4\pi D |\mathbf{r}_s - \mathbf{r}_d|} \exp(-\mu_{\text{eff}} |\mathbf{r}_s - \mathbf{r}_d|). \quad (\text{D.2})$$

The effect on emitted fluence rate, when the instrument deliver light for treatment is given by

$$\Phi(\mathbf{r}_s, \mathbf{r}) = \frac{P_s \exp(-\alpha x_s)}{4\pi D |\mathbf{r}_s - \mathbf{r}|} \exp(-\mu_{\text{eff}} |\mathbf{r}_s - \mathbf{r}|). \quad (\text{D.3})$$

The simulation was performed according to the following scheme

- (i) Sphere radius was uniformly sampled between 0 and 4 mm for each fiber.
- (ii) The measurable was calculated using Equation (D.2) for each source detector pair.
- (iii) The IDOSE evaluation protocol was evaluated in order to retrieve μ_{eff} .
- (iv) The IDOSE protocol optimized the treatment time for each fiber based on evaluations in (iii) assuming non-perturbed fibers.
- (v) Treatment fraction was calculated assuming non-perturbed fibers, Equation (3.26), as well as perturbed fibers, Equation (D.3), for reference.

The procedure was repeated 100 times for each patient prostate model assuming homogeneous bulk optical properties; $\mu_a = 0.04 \text{ mm}^{-1}$ and $\mu'_s = 0.9 \text{ mm}^{-1}$. The results are given, in terms of treatment fraction, in Figure D.2. Here it is seen that the simulated local blood absorbers will cause a 5-50% decrease in the treated volume fraction.

Although this is alleviated to some extent by the overtreatment of the prostate, local undertreatment will occur. A fiber with high attenuation will not contribute to the expected total dose since the current dosimetry scheme does not account for the attenuation factors. It is then warranted to develop an inverse model that can assess the parameters x_s , see Equation (D.2), for all fibers.

A first approach towards this scheme was taken where Equation (D.2) was used instead of Equation (3.26) in the evaluation of optical properties. A non-linear fitting routine was applied, instead of the linear regression scheme in IDOSE, in order to estimate μ_{eff} and x_s for each fiber. Although successful on simulation results the inverse model could not completely describe the clinical measurements. A postulated reason is the attenuation model above, that might be too simple. Heterogeneous tissue and local fiber absorbers can cause the same effect on the measurements. When

applying Equation (D.2) all perturbations will be described by the fiber attenuation which in turn could lead to erroneous assessment of bulk optical properties when heterogeneous tissue is present. Another reason might be the assumption that local absorbers or heterogeneities cause the measured intensity to decrease. Varying scattering could also render the same effect. This non-uniqueness, enlightened in the discussion above, arise from the use of steady-state measurements.

The proposed remedy would be to improve the NIR-light sources so that multispectral measurements can be performed with sufficient signal-to-noise. With multispectral evaluation of the optical properties, the uniqueness will be increased as presented in e.g. [297]. In addition to the instrumentation improvements the evaluation protocol should be extended to adapt a heterogeneous evaluation of the absorption and scattering. The bulk tissue heterogeneities could then, potentially, be separated more reliably from the fiber specific absorbers. Time- or frequency domain measurements are also an alternative to solve the same problem, although more technically advanced instrumentation is then required. This might not always be clinically applicable.

D.2 Perturbation of photosensitizer reconstruction

When performing interstitial tomographic imaging of the photosensitizer some of the perturbations discussed in Section 6.4.3 can cause alterations of the results. In this section the effect on fluorophore reconstruction is assessed through simulations of light propagation in a prostate model. Before the simulations are introduced a discussion about how local absorbers affect fluorophore reconstructions is given.

D.2.1 Fiber-specific absorbers

The tomographic imaging scheme uses the normalized Born measurable where the fluorescence intensity is normalized with the excitation intensity for each source-detector pair. This is a relative measurement which is virtually unaffected by the source fiber attenuation. The robustness against source power alterations is identified to be one of the main advantages of this measurable [220]. An additional perturbation in the interstitial setup is that a local absorber might be present at the detector as well. When assuming that an absorber is caused by accumulation of blood, the spectral dependence of the transmission might influence the excitation and fluorescence differently. The spectral variation in attenuation is constant and could potentially be approximated through simulations, compare to the factor α in Equation (D.1). In the work

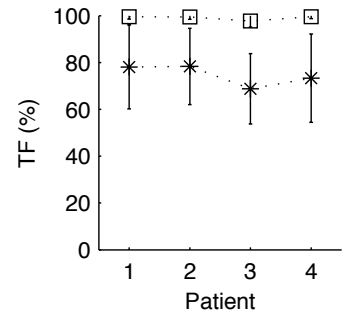


Figure D.2. The treatment fraction decrease, for each patient prostate model, due to simulated fiber-specific attenuation.

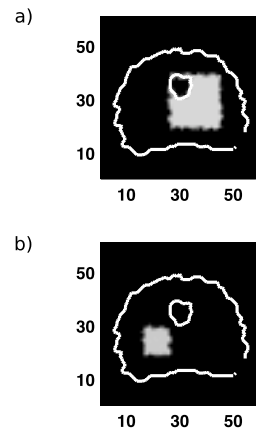


Figure D.3. Cross-section of the model with a) fluorophore b) absorption inclusion.

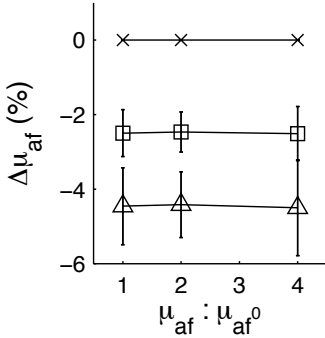


Figure D.4. The error on reconstructed μ_{af} due to a small absorbing heterogeneity. The errorbars depict ± 1 SD of the reconstructed values within the prostate. The absorption contrast is 1 (\times), 2 (\square) and 3 (\triangle) whereas the fluorophore contrast is denoted on the x-axis.

presented in this thesis the excitation and fluorescence is assumed to have the same transmission through potential blood absorbers. The difference in transmission will cause a decrease in the absolute level of the reconstruction results but since it is a constant it will be the same for all fibers, hence no spatial deviations will arise.

D.2.2 Absorbing heterogeneities

One potential cause of the undertreatment was postulated to be heterogeneous tissue. In practice the heterogeneity will affect the estimated μ_{eff} for each fiber. These are interpolated from the IDOSE evaluation to the reconstruction FEM-model. The simulation model is seen in Figure D.3, where panel a shows the fluorescent inclusion and b shows an absorption inclusion. The simulation procedure is presented below. Here the fluorophore contrast is referred to as the inclusion-to-bulk ratio ($\mu_{af} : \mu_{af}^0$) and analogously for the absorption inclusion.

- (i) Assign bulk optical properties ($\mu_a^0 = 0.03 \text{ mm}^{-1}$, $\mu_s^0 = 0.9 \text{ mm}^{-1}$ and $\mu_{af}^0 = 0.001 \text{ mm}^{-1}$) to the model geometry.
- (ii) Forward modeling of cases where the absorption inclusion contrast was [1, 2, 3] and the fluorophore contrast was [1, 2, 4].
- (iii) IDOSE evaluation and interpolation of the results into FEM-model.
- (iv) Fluorophore reconstructions
- (v) Calculate error relative absorption contrast [1], i.e. no inclusion.

The error estimate is defined by

$$\Delta\mu_{af} = \frac{\mu_{af}^* - \mu_{af}}{\mu_{af}^*} \quad (\text{D.4})$$

where μ_{af}^* is the reconstructed result at absorption contrast [1] for every fluorescent contrast case. All nodes within the prostate region are included in calculation of Equation (D.4). The result is seen in Figure D.4 where it is evident that a higher absorption of the inclusion causes underestimation of the fluorophore absorption. The perturbation will cause a slight increase in μ_{eff} for fibers close to the absorption inclusion. When interpolating the IDOSE evaluations the absorption will be smoothed throughout the volume. Hence, too low absorption is rendered compared to the true case. When the reconstruction is executed the lower optical properties results in higher fluence rates that will cause the reconstructed value to decrease. Since a relative measurable is adopted the effect is moderate.

It is also seen, in Figure D.4, that the deviation is constant irrespective of fluorophore contrast. This was further investigated in a similar simulation procedure. The fluorophore was here homogeneously distributed throughout the whole geometry. The results, shown in Figure D.5, indicate that the absorptive inclusion has negligible effect on the mimicked bleaching kinetics.

The spatial deviations were, indeed, very small hence images showing cross-sectional reconstructions are omitted here.

D.2.3 Fiber position inaccuracies

Inaccurate placement of the fibers is deemed to potentially cause errors. This was investigated for the case of light-fluence dosimetry in Paper VI. A corresponding simulation case was here applied in order to investigate how inaccurate fiber positions will affect the photosensitizer reconstruction.

The geometry included a fluorescent inclusion, according to Figure D.3a. The fiber positions was perturbed with randomized deviations in three dimensions. These were sampled from a uniform distribution allowing a maximum deviation of 2 mm. The simulations followed the procedure below.

- (i) Assign bulk optical properties ($\mu_a^0 = 0.03 \text{ mm}^{-1}$, $\mu_s^0 = 0.9 \text{ mm}^{-1}$ and $\mu_{af}^0 = 0.001 \text{ mm}^{-1}$) to the model geometry. Assign fluorescent contrast [2] to the inclusion.
- (ii) Forward modeling using accurate fiber positions.
- (iii) Random sample Δx , Δy , Δz .
- (iv) Forward modeling using inaccurate fiber positions.
- (v) Repeat from iii), 25 times.
- (vi) IDOSE evaluation and interpolation of the results into FEM-model.
- (vii) Fluorophore reconstructions using accurate fiber positions in all cases.
- (viii) Calculate error relative accurate fiber positions, analogously to Equation (D.4).

Even though 25 times is not enough to perform statistical analysis, the simulation results are taken as appropriate estimates of the expected deviations. The error due to inaccuracies in fiber position is shown in Figure D.6 where all voxels within the prostate are included in the calculation of Equation (D.4). The standard deviation is calculated based on 25 simulations for each voxel. It is seen that, on average, the errors are within $\pm 10\%$ although some voxels evidence large variations. A voxel placed close to a source,

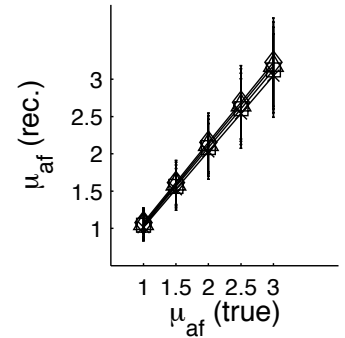


Figure D.5. The effect of absorption heterogeneity contrast in the temporal change of fluorophore yield.

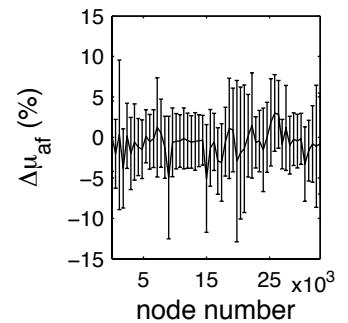


Figure D.6. The error due to inaccurate fiber positioning. The graph shows the average error ± 1 SD for every node within the prostate volume.

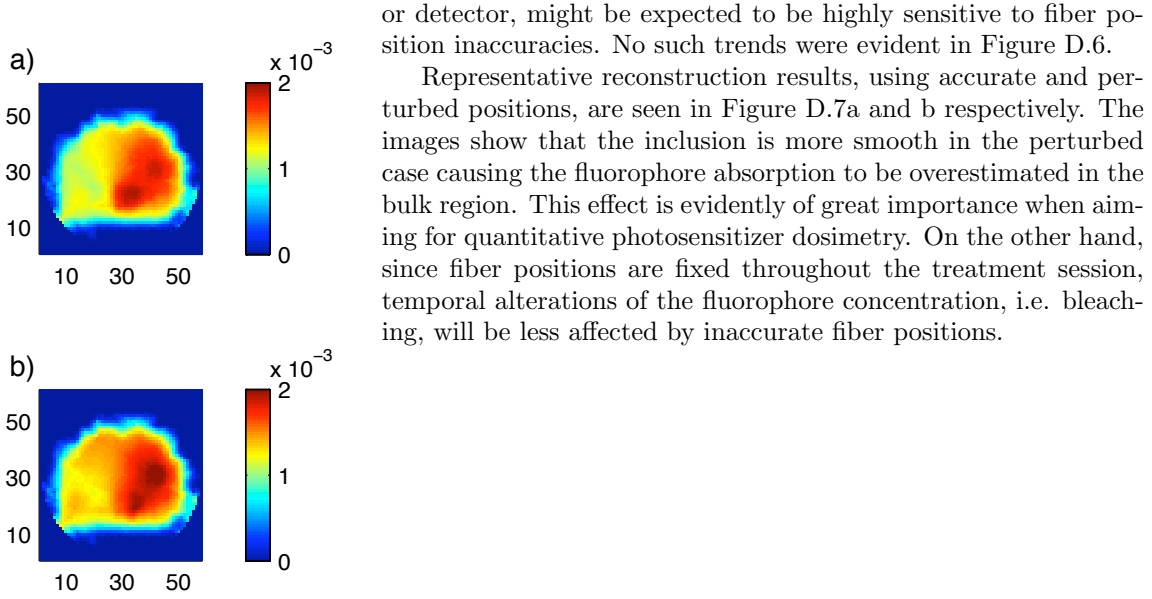


Figure D.7. Cross-sectional slice from the simulated geometry with a) accurate and b) perturbed fiber positions.

or detector, might be expected to be highly sensitive to fiber position inaccuracies. No such trends were evident in Figure D.6.

Representative reconstruction results, using accurate and perturbed positions, are seen in Figure D.7a and b respectively. The images show that the inclusion is more smooth in the perturbed case causing the fluorophore absorption to be overestimated in the bulk region. This effect is evidently of great importance when aiming for quantitative photosensitizer dosimetry. On the other hand, since fiber positions are fixed throughout the treatment session, temporal alterations of the fluorophore concentration, i.e. bleaching, will be less affected by inaccurate fiber positions.

COMMENTS ON THE PAPERS

I **Spatially varying regularization based on spectrally resolved fluorescence emission in fluorescence molecular tomography**

J. Axelsson, J. Svensson, S. Andersson-Engels

The paper presents a method for retrieval of a spatially varying regularization matrix based on fluorescence emission data. The scheme relies on the measurements acquired at two spectral bands as well as different positions on the tissue surface. Due to difference in attenuation of the two fluorescence bands a simple approach was developed in order to determine the most likely region for a fluorescent inclusion within a scattering medium. The use of this information was then imposed onto a reconstruction scheme as a constraint. In conclusion the use of prior information, based on fluorescence emission, showed slightly improved reconstruction results in terms of resolution.

I developed the evaluation scheme as well as the experimental setup. I prepared the manuscript.

II A matrix-free algorithm for multiple wavelength fluorescence tomography

A. Zacharopoulos, P. Svenmarker, J. Axelsson, M. Schweiger, S. Arridge, S. Andersson-Engels

The paper presents a reconstruction method that alleviates the need to construct large system matrices. In optical tomography numerous of source-detector pairs are applied in the measurement setup. In addition the measurements can be multispectral leading to even larger datasets. The problem that was targeted in this work was the need to produce a system matrix that is limited by the available computer memory. The scheme presented here avoid storage of the system matrix and instead iteratively find the solution. The method was tested on multispectral fluorescence tomography data, both simulated and experimental, and it was concluded that the rationale provide substantial benefits in computational time and memory requirement.

I took part in the algorithm development. I prepared parts of the manuscript.

III Autofluorescence insensitive imaging using upconverting nanocrystals in scattering media

C. Xu, N. Svensson, J. Axelsson, P. Svenmarker, G. Somesfalean, G. Chen, H. Liang, Z. Zhang, S. Andersson-Engels

In this paper so called up-converting nanocrystals are applied as fluorescent contrast markers in a liquid phantom study. The intent was to show the feasibility of this kind of nanoparticles, that emit anti-Stokes shifted fluorescence, for potential use in biomedicine. Since endogenous fluorophores yield Stokes shifted fluorescence the up-converted fluorescence will not be contaminated by autofluorescence. The feasibility was confirmed by exciting the fluorophore, within the scattering medium, at 978 nm and detecting the fluorescence at 800 nm. Irrespective of added background fluorophore, mimicking endogenous fluorophores, the contrast to background was relatively constant.

I took part in the instrument development and discussions concerning data evaluation.

IV Fluorescence diffuse optical tomography using upconverting nanoparticles

C. Xu, J. Axelsson, S. Andersson-Engels

The paper presents the first efforts to image the nanocrystals in Paper **III** in three dimensions when situated within a scattering liquid phantom. A reconstruction scheme for this purpose was developed with the ability to describe the two-photon excitation process. The experimental study verified that reconstructions using upconverting nanocrystals provide slightly higher resolution of the target than compared to linear, Stokes shifter fluorophores. I took part in the instrumentation development, algorithm development and data evaluation.

V Fluorescence monitoring of a topically applied liposomal Temoporfin formulation and photodynamic therapy of non-pigmented skin malignancies

N. Bendsoe, L. Persson, A. Johansson, J. Svensson, J. Axelsson, S. Andersson-Engels, S. Svanberg, K. Svanberg

In this clinical endeavour 35 skin lesions were treated at the Departments of Dermatology and Oncology, Lund University Hospital employing a liposomal formulation of mTHPC. In addition, the time between topical drug administration and light delivery was in the order of hours. Several instruments, i.e. fluorescence imaging/spectroscopy and absorption spectroscopy, were applied to investigate the selective accumulation of the photosensitizer compound. The conclusion of this study was that liposomal mTHPC, applied topically, rendered good tumor-normal tissue contrast.

I took part in the experimental work and data analysis. I also wrote minor parts of the manuscript.

VI Realtime light dosimetry software tools for interstitial photodynamic therapy of the human prostate

A. Johansson, J. Axelsson, J. Swartling, S. Andersson-Engels

In this paper a rationale for individualized and real-time treatment planning for interstitial photodynamic therapy of the prostate is presented and analyzed. The scheme relies on optical measurements before, during and after treatment that are used for calculation of the optical attenuation of the target volume. The optical properties are employed to iteratively find the fiber-specific treatment times that render a total delivered dose that meet the predefined threshold dose. The analysis was performed on simulated data from a realistic prostate model. In conclusion the scheme was successful in delivering the intended light dose to the whole prostate gland despite variations in optical attenuation and slight fiber position deviations.

I took part in the development of software routines and data analysis. Finally, I prepared parts of the manuscript.

VII System for interstitial photodynamic therapy with online dosimetry - first clinical experiences of prostate

J. Swartling, J. Axelsson, G. Ahlgren, K. Kalkner, S. Nilsson, S. Svanberg, K. Svanberg, S. Andersson-Engels

This manuscript presents the first results from a clinical study of photodynamic therapy of primary prostate cancer, employing mTHPC, and the online dosimetry scheme presented in Paper VI. The intent was to ablate the whole prostate while limiting the delivered light fluence dose to organs at risk, such as urethra and rectum. Based on post-treatment calculations of the delivered dose the system showed capabilities to meet the intended goal. Despite this fact 3 of 4 patients had viable cancer cells at the 6 month follow-up. MRI also confirmed potential undertreatment since only parts of the prostate volume had decreased enhancement when investigation was performed two weeks post-treatment. The reason for incomplete treatment outcome was postulated to be 1) a too low and conservatively set threshold dose and 2) fiber-specific fibre attenuation caused by heterogeneities such as blood occlusion.

I took part in the development of instrumentation and dosimetry software as well as data analysis. I prepared major parts of the manuscript.

VIII **In vivo photosensitizer tomography inside the human prostate**

J. Axelsson, J. Swartling, S. Andersson-Engels

In this paper the feasibility to reconstruct the photosensitizer distribution throughout a scattering volume, i.e. the prostate, was investigated. Data from the clinical study in Paper **VII** as well as a phantom study was utilized. Due to the ill-posedness of the fundamental problem the solution must be regularized leading to a smooth solution. The capability to reconstruct the absolute concentration of a fluorescent inclusion was assessed in a phantom study. The absolute value was within 15% from the true value although the appearance was more smooth.

I implemented the reconstruction scheme, took part in the instrument development, performed the data evaluation and prepared the manuscript.

ACKNOWLEDGEMENTS

I am deeply grateful to Prof. Stefan Andersson-Engels who has mentored me throughout this endeavor. Your guiding, encouragement and support have played an important role and will never be forgotten.

I would also like to express my gratitude to Prof. Katarina Svanberg. I have truly enjoyed your company and expertise, not at least during tough measurement campaigns.

My appreciation also goes to Prof. Sune Svanberg. Your enthusiasm is inspiring and contagious. For that, I am very thankful.

Furthermore, I thank my colleagues in the Biophotonics group; Erik Alerstam, Dmitry Khoptyar, Haichun Liu, Pontus Svenmarker, Tomas Svensson, Haiyan Xie, Can Xu and Mikkel Brydegaard Sørensen for providing the friendliest atmosphere anyone can imagine. It has been a blessing to have you all around.

I would also like to express a special thanks to Ann Johansson, Jenny Skans, Linda Persson, Niels Bendsoe and Christoffer Abrahamsson and Gabriel Somesfalean for good collaboration and equally important contributions to the friendly atmosphere.

Moreover, I thank past and present people at SpectraCure; Johannes Swartling, Stephan Dymling, Sara Pålsson, Rasmus Grönlund, Thomas Johansson and Johan Stensson for inspiring collaboration.

I also thank Susanna Gräfe and Tilmann Trebst at Biolitec for being such good hosts during the Jena-campaign.

Furthermore, my appreciation goes to Ilya Turchin and the people at the Biophotonics Laboratory, for interesting discussions in Nizhny Novgorod.

I am very grateful to Prof. Simon Arridge, Athanasios Zacharopoulos and Martin Schweiger, at University College London, for interesting and fruitful collaborative work.

Thanks also to all veterinaries and clinicians for your substantial contribution to this work; Odd Höglund, Kerstin Hansson and Anne-Sofie Lagerstedt at SLU, Uppsala, and Göran Ahlgren at Department of Urology, Malmö University Hospital as well as Karl Mikael Kälkner and Sten Nilsson at Department of Oncology, Radiumhemmet, Karolinska University Hospital.

I also thank past and present colleagues at the Atomic physics division for providing a friendly, exciting and stimulating environment.

From the bottom of my heart I extend the deepest gratitude to my friends and family for always being there.

I acknowledge financial support from Kgl. Fysiografiska Sällskapet, SpectraCure AB as well as EC integrated projects BRIGHT.EU and Molecular Imaging.

REFERENCES

- [1]. C.D. Mathers, C. Bernard, K.M. Iburg, M. Inoue, D. Ma Fat, K. Shibuya, C. Stein, N. Tomijima and H. Xu. *Global burden of disease in 2002: data sources, methods and results*. Geneva, Switzerland, WHO (2003).
- [2]. P. Boyle and B. Levin. *World cancer report 2008*. IARC Press (2008).
- [3]. J. Ferlay, F. Bray, P. Pisani and DM Parkin. *GLOBOCAN 2002: Cancer Incidence, Mortality and Prevalence Worldwide IARC Cancer Base No. 5. version 2.0*. Lyon: IARCPress (2004).
- [4]. D. Hanahan and R.A. Weinberg. *The hallmarks of cancer*. Cell **100**, 57–70 (2000).
- [5]. M. G. Pomper. *Molecular imaging: an overview*. Acad Radiol **8**, 1141–1153 (2001).
- [6]. Michael Stabin. *Nuclear medicine dosimetry*. Physics in Medicine and Biology **51**, R187–R202 (2006).
- [7]. Thomas Bortfeld. *IMRT: a review and preview*. Phys Med Biol **51**, R363–R379 (2006).
- [8]. P. Okunieff, D. Morgan, A. Niemierko and H.D. Suit. *Radiation dose-response of human tumors*. International Journal of Radiation Oncology* Biology* Physics **32**, 1227–1237 (1995).
- [9]. L. Xing, B. Thorndyke, E. Schreibmann, Y. Yang, T.F. Li, G.Y. Kim, G. Luxton and A. Koong. *Overview of image-guided radiation therapy*. Medical Dosimetry **31**, 91–112 (2006).
- [10]. W.N. Hait and T.W. Hambley. *Targeted cancer therapeutics*. Cancer Research **69**, 1263 (2009).
- [11]. O. Raab. *Über die wirkung fluoreszierender stoffe auf infusoria*. Z Biol **39**, 524 (1900).
- [12]. H. Tappeiner and A. Jodlbauer. *Die sensibilisierende Wirkung fluoreszierender Substanzen: gesammelte Untersuchungen über die photodynamische Erscheinung*. Vogel (1907).
- [13]. F. Meyer-Betz. *Untersuchungen über die biologische (photodynamische) Wirkung des Hamatoporphyrins und anderer Derivate des Blut- und Gallenfarbstoffs*. Dtsch Arch Klin Med **112**, 476–503 (1913).
- [14]. A. Policard. *Etude sur les aspects offerts par des tumeurs experimentales examinees a la lumiere de Wood*. CR Soc Biol **91**, 1423–1424 (1924).
- [15]. RL Lipson, EJ Baldes and AM Olsen. *The use of a derivative of hematoporphyrin in tumor detection*. Journal of the National Cancer Institute **26**, 1 (1961).
- [16]. R.L. Lipson, E.J. Baldes and A.M. Olsen. *Further evaluation of the use of hematoporphyrin derivative as a new aid for the endoscopic detection*

- of malignant disease. *Chest* **46**, 676 (1964).
- [17]. HB Gregorie Jr, EO Horger, JL Ward, JF Green, T. Richards, HC Robertson Jr and TB Stevenson. *Hematoporphyrin-derivative fluorescence in malignant neoplasms*. *Annals of Surgery* **167**, 820 (1968).
 - [18]. TJ Dougherty, GB Grindey, R. Fiel, KR Weishaupt and DG Boyle. *Photoradiation therapy. II. Cure of animal tumors with hematoporphyrin and light*. *Journal of the National Cancer Institute* **55**, 115 (1975).
 - [19]. T.J. Dougherty, J.E. Kaufman, A. Goldfarb, K.R. Weishaupt, D. Boyle and A. Mittleman. *Photoradiation therapy for the treatment of malignant tumors*. *Cancer Research* **38**, 2628–2635 (1978).
 - [20]. F. Stewart, P. Baas and W. Star. *What does photodynamic therapy have to offer radiation oncologists (or their cancer patients)?* *Radiothermal Oncology* **48**, 233–248 (1998).
 - [21]. H. Barr, CJ Tralau, PB Boulos, AJ MacRobert, R. Tilly and SG Bown. *The contrasting mechanisms of colonic collagen damage between photodynamic therapy and thermal injury*. *Photochemistry and photobiology* **46**, 795 (1987).
 - [22]. V. Ntziachristos. *Fluorescence molecular imaging*. *Annu Rev Biomed Eng* **8**, 1–33 (2006).
 - [23]. J.R. Mourant, T. Fuselier, J. Boyer, T.M. Johnson and I.J. Bigio. *Predictions and measurements of scattering and absorption over broad wavelength ranges in tissue phantoms*. *Applied Optics* **36**, 949–957 (1997).
 - [24]. I.J. Bigio and J.R. Mourant. *Ultraviolet and visible spectroscopies for tissue diagnostics: fluorescence spectroscopy and elastic-scattering spectroscopy*. *Physics in Medicine and Biology* **42**, 803–814 (1997).
 - [25]. X. Wang, B.W. Pogue, S. Jiang, X. Song, K.D. Paulsen, C. Kogel, S.P. Poplack and W.A. Wells. *Approximation of Mie scattering parameters in near-infrared tomography of normal breast tissue in vivo*. *Journal of Biomedical Optics* **10**, 051704 (2005).
 - [26]. C.F. Bohren and D.R. Huffman. *Absorption and Scattering of Light by Small Particles*. John Wiley & Sons Inc (1983).
 - [27]. H.J. van Staveren, C.J.M. Moes, J. van Marie, S.A. Prahl and M.J.C. van Gemert. *Light scattering in Intralipid-10% in the wavelength range of 400–1100 nm*. *Appl. Opt* **30**, 4507–4514 (1991).
 - [28]. R. Graaff, JG Aarnoudse, J.R. Zijp, PMA Sloot, FFM De Mul, J. Greve and MH Koelink. *Reduced light-scattering properties for mixtures of spherical particles: a simple approximation derived from Mie calculations*. *Applied Optics* **31**, 1370–1376 (1992).
 - [29]. Angelo Sassaroli and Sergio Fantini. *Comment on the modified Beer-Lambert law for scattering media*. *Physics in Medicine and Biology* **49**, N255–N257 (2004).
 - [30]. S.A. Prahl. *Optical absorption of hemoglobin*. URL <http://omlc.orgi.edu/spectra/hemoglobin/index.html> (2009).
 - [31]. G.M. Hale and M.R. Querry. *Optical constants of water in the 200-nm to 200- μ m wavelength region*. *Appl Opt* **12**, 555–563 (1973).
 - [32]. RLP Van Veen, H. Sterenborg, A. Pifferi, A. Torricelli and R. Cubeddu. *Determination of VIS-NIR absorption coefficients of mammalian fat, with time- and spatially resolved diffuse reflectance and transmission spectroscopy*. *Proceedings of Biomedical Topical Meetings* (2000).
 - [33]. S.J. Matcher and C.E. Cooper. *Absolute quantification of deoxyhaemoglobin concentration in tissue near infrared spectroscopy*. *Phys Med Biol* **39**, 1295–1312 (1994).
 - [34]. F. Bevilacqua, A. J. Berger, A. E. Cerussi, D. Jakubowski and B. J.

- Tromberg. *Broadband absorption spectroscopy in turbid media by combined frequency-domain and steady-state methods*. Appl Opt **39**, 6498–6507 (2000).
- [35]. Albert Cerussi, Natasha Shah, David Hsiang, Amanda Durkin, John Butler and Bruce J Tromberg. *In vivo absorption, scattering, and physiologic properties of 58 malignant breast tumors determined by broadband diffuse optical spectroscopy*. J Biomed Opt **11**, 044005 (2006).
- [36]. H. Fedorow, F. Tribl, G. Halliday, M. Gerlach, P. Riederer and KL Double. *Neuromelanin in human dopamine neurons: comparison with peripheral melanins and relevance to Parkinson's disease*. Progress in neurobiology **75**, 109–124 (2005).
- [37]. W J Bowen. *The absorption spectra and extinction coefficients of myoglobin*. J Biol Chem **179**, 235–245 (1949).
- [38]. R.S. Balaban, V.K. Mootha and A.E. Arai. *Spectroscopic determination of cytochrome c oxidase content in tissues containing myoglobin or hemoglobin*. Anal Biochem **237**, 274–278 (1996).
- [39]. B. Valeur. *Molecular fluorescence: Principles and Applications*. Wiley-VCH (2001).
- [40]. D.Y. Paithankar, A.U. Chen, B.W. Pogue, M.S. Patterson and E.M. Sevick-Muraca. *Imaging of fluorescent yield and lifetime from multiply scattered light reemitted from random media*. Appl Opt **36**, 2260–2272 (1997).
- [41]. J.R. Lakowicz. *Principles of Fluorescence Spectroscopy*. Springer Verlag (2006).
- [42]. S. Andersson-Engels, J. Johansson, U. Stenram, K. Svanberg and S. Svanberg. *Malignant tumor and atherosclerotic plaque diagnosis using laser-induced fluorescence*. IEEE Journal of Quantum Electronics **26**, 2207–2217 (1990).
- [43]. R. Richards-Kortum and E. Sevick-Muraca. *Quantitative optical spectroscopy for tissue diagnosis*. Annu Rev Phys Chem **47**, 555–606 (1996).
- [44]. M.A. Mycek and B.W. Pogue. *Handbook of biomedical fluorescence*. CRC (2003).
- [45]. I. Georgakoudi, B.C. Jacobson, M.G. Müller, E.E. Sheets, K. Badizadegan, D.L. Carr-Locke, C.P. Crum, C.W. Boone, R.R. Dasari, J. van Dam and M.S. Feld. *NAD(P)H and collagen as in vivo quantitative fluorescent biomarkers of epithelial precancerous changes*. Cancer Res **62**, 682–687 (2002).
- [46]. N. Billinton and A.W. Knight. *Seeing the wood through the trees: a review of techniques for distinguishing green fluorescent protein from endogenous autofluorescence*. Analytical Biochemistry **291**, 175–197 (2001).
- [47]. G.R. Cherrick, S.W. Stein, C.M. Leevy and C.S. Davidson. *Indocyanine green: observations on its physical properties, plasma decay, and hepatic extraction*. Journal of Clinical Investigation **39**, 592 (1960).
- [48]. V. Ntziachristos, A.G. Yodh, M. Schnall and B. Chance. *Concurrent MRI and diffuse optical tomography of breast after indocyanine green enhancement*. PNAS **97**, 2767–2772 (2000).
- [49]. J. Rao, A. Dragulescu-Andrasi and H. Yao. *Fluorescence imaging in vivo: recent advances*. Current opinion in biotechnology **18**, 17–25 (2007).
- [50]. D. Neri, B. Carnemolla, A. Nissim, A. Leprini, G. Querzè, E. Balza, A. Pini, L. Tarli, C. Halin, P. Neri et al. *Targeting by affinity-matured recombinant antibody fragments of an angiogenesis associated fibronectin isoform*. Nature biotechnology **15**, 1271–1275 (1997).
- [51]. S. Folli, P. Westermann, D. Braichotte, A. Pelegrin, G. Wagnieres,

- H. van den Bergh and J.P. Mach. *Antibody-iodocyanin conjugates for immunophotodetection of human squamous cell carcinoma in nude mice*. *Cancer Research* **54**, 2643–2649 (1994).
- [52]. S. Ke, X. Wen, M. Gurfinkel, C. Charnsangavej, S. Wallace, E.M. Sevick-Muraca and C. Li. *Near-Infrared Optical Imaging of Epidermal Growth Factor Receptor in Breast Cancer Xenografts*. *Cancer Research* **63**, 7870 (2003).
- [53]. W.T. Chen, U. Mahmood, R. Weissleder and C.H. Tung. *Arthritis imaging using a near-infrared fluorescence folate-targeted probe*. *Arthritis Res Ther* **7**, R310–R317 (2005).
- [54]. R.P. Haugland. *The Handbook—A Guide to Fluorescent Probes and Labeling Technologies, ; Molecular Probes*. Inc.: Eugene, OR (2006).
- [55]. R. Weissleder, C.-H. Tung, U. Mahmood and A. Bogdanov. *In vivo imaging of tumors with protease-activated near-infrared fluorescent probes*. *Nat Biotechnol* **17**, 375–378 (1999).
- [56]. G. Grynkiewicz, M. Poenie and RY Tsien. *A new generation of Ca²⁺ indicators with greatly improved fluorescence properties*. *Journal of Biological Chemistry* **260**, 3440–3450 (1985).
- [57]. I. Johnson. *Fluorescent probes for living cells*. *The Histochemical Journal* **30**, 123–140 (1998).
- [58]. E.P. Widmaier, H. Raff and K.T. Strang. *Vander's Human Physiology: The Mechanisms of Body Function*. McGraw-Hill 11 edition (2008).
- [59]. R.M. Hoffman. *The multiple uses of fluorescent proteins to visualize cancer in vivo*. *Nature Reviews Cancer* **5**, 796–806 (2005).
- [60]. M. Chalfie, Y. Tu, G. Euskirchen, WW Ward and DC Prasher. *Green fluorescent protein as a marker for gene expression*. *Science* **263**, 802–805 (1994).
- [61]. Scott K Lyons. *Advances in imaging mouse tumour models in vivo*. *J Pathol* **205**, 194–205 (2005).
- [62]. R. Heim, DC Prasher and RY Tsien. *Wavelength mutations and post-translational autooxidation of green fluorescent protein*. *Proceedings of the National Academy of Sciences* **91**, 12501–12504 (1994).
- [63]. N.C. Shaner, M.Z. Lin, M.R. McKeown, P.A. Steinbach, K.L. Hazelwood, M.W. Davidson and R.Y. Tsien. *Improving the photostability of bright monomeric orange and red fluorescent proteins*. *Nature Methods* **5**, 545–551 (2008).
- [64]. X. Michalet, FF Pinaud, LA Bentolila, JM Tsay, S. Doose, JJ Li, G. Sundaresan, AM Wu, SS Gambhir and S. Weiss. *Quantum dots for live cells, in vivo imaging, and diagnostics*. *Science* **307**, 538–544 (2005).
- [65]. Feng Wang, Wee Beng Tan, Yong Zhang, Xianping Fan and Minquan Wang. *Luminescent nanomaterials for biological labelling*. *Nanotechnology* **17**, R1–R13 (2006).
- [66]. S. Kumar and R. Richards-Kortum. *Optical molecular imaging agents for cancer diagnostics and therapeutics*. *Nanomedicine* **1**, 23–30 (2006).
- [67]. X. Gao, Y. Cui, R.M. Levenson, L.W.K. Chung and S. Nie. *In vivo cancer targeting and imaging with semiconductor quantum dots*. *Nature Biotechnology* **22**, 969–976 (2004).
- [68]. Dev K Chatterjee, Abdul J Rufaihah and Yong Zhang. *Upconversion fluorescence imaging of cells and small animals using lanthanide doped nanocrystals*. *Biomaterials* **29**, 937–943 (2008).
- [69]. S. A. Hilderbrand, F. Shao, C. Salthouse, U. Mahmood and R. Weissleder. *Upconverting luminescent nanomaterials: application to in vivo bioimaging*. *Chem. Commun.* **28**, 4188–4190 (2009).

- [70]. C. Vinegoni, D. Razansky, S.A. Hilderbrand, F. Shao, V. Ntziachristos and R. Weissleder. *Transillumination fluorescence imaging in mice using biocompatible upconverting nanoparticles*. *Optics Letters* **34**, 2566–2568 (2009).
- [71]. W. Stummer, A. Novotny, H. Stepp, C. Goetz, K. Bise, H.J. Reulen et al. *Fluorescence-guided resection of glioblastoma multiforme by using 5-aminolevulinic acid-induced porphyrins: a prospective study in 52 consecutive patients*. *J Neurosurg* **93**, 1003–1013 (2000).
- [72]. W. Stummer, U. Pichlmeier, T. Meinel, O.D. Wiestler, F. Zanella and H.J. Reulen. *Fluorescence-guided surgery with 5-aminolevulinic acid for resection of malignant glioma: a randomised controlled multicentre phase III trial*. *Lancet Oncology* **7**, 392–401 (2006).
- [73]. K.R. Weishaupt, C.J. Gomer, T.J. Dougherty et al. *Identification of singlet oxygen as the cytotoxic agent in photoinactivation of a murine tumor*. *Cancer Res* **36**, 2326–2329 (1976).
- [74]. I.J. MacDonald and T.J. Dougherty. *Basic principles of photodynamic therapy*. *J Porphyrins Phthalocyanines* **5**, 105–129 (2001).
- [75]. Z. Luksiene. *Photodynamic therapy: mechanism of action and ways to improve the efficiency of treatment*. *Medicina (Kaunas, Lithuania)* **39**, 1137 (2003).
- [76]. B.C. Wilson, Patterson M. S. and L. Lilge. *Implicit and Explicit Dosimetry in Photodynamic Therapy: a New Paradigm*. *Lasers Med Sci* **12**, 182–199 (1997).
- [77]. A.P. Castano, T.N. Demidova and M.R. Hamblin. *Mechanisms in photodynamic therapy: part one - photosensitizers, photochemistry and cellular localization*. *Photodiagnosis and Photodynamic Therapy* **1**, 279–293 (2004). Review article.
- [78]. E. Reddi. *Role of delivery vehicles for photosensitizers in the photodynamic therapy of tumours*. *Journal of Photochemistry & Photobiology, B: Biology* **37**, 189–195 (1997).
- [79]. D. Kessel, P. Thompson, K. Saatio and K.D. Nantwi. *Tumor localization and photosensitization by sulfonated derivatives of tetraphenylporphine*. *Photochemistry and photobiology* **45**, 787–790 (1987).
- [80]. Ana P. Castano, Tatiana N. Demidova and Michael R. Hamblin. *Mechanisms in photodynamic therapy: Part three Photosensitizer pharmacokinetics, biodistribution, tumor localization and modes of tumor destruction*. *Photodiagnosis and Photodynamic Therapy* **2**, 91–106 (2005).
- [81]. YK Ho, RG Smith, MS Brown and JL Goldstein. *Low-density lipoprotein (LDL) receptor activity in human acute*. *Blood* **52**, 1099 (1978).
- [82]. BA Allison, PH Pritchard and JG Levy. *Evidence for low-density lipoprotein receptor-mediated uptake of benzoporphyrin derivative*. *British journal of cancer* **69**, 833 (1994).
- [83]. W.G. Roberts and T. Hasan. *Role of neovasculature and vascular permeability on the tumor retention of photodynamic agents*. *Cancer Research* **52**, 924–930 (1992).
- [84]. SK Schwartz, K. Absolon and H. Vermund. *Some relationships of porphyrins, X-rays and tumors*. *Univ. Minn. Med. Bull* **27**, 7–8 (1955).
- [85]. JC Kennedy, RH Pottier and DC Pross. *Photodynamic therapy with endogenous protoporphyrin IX: basic principles and present clinical experience*. *Journal of photochemistry and photobiology. B, Biology* **6**, 143 (1990).
- [86]. Q. Peng, K. Berg, J. Moan, M. Kongshaug and J.M. Nesland. *5-Aminolevulinic acid-based photodynamic therapy: principles and experimental research*. *Photochemistry and photobiology* **65**, 235–251

- (1997).
- [87]. MM El-Sharabasy, AM El-Waseef, MM Hafez and SA Salim. *Porphyryn metabolism in some malignant diseases*. British journal of cancer **65**, 409 (1992).
- [88]. X. D. Zhou, B. W. Pogue, B. Chen, E. Demidenko, R. Joshi, J. Hoopes and T. Hasan. *Pretreatment photosensitizer dosimetry reduces variation in tumor response*. International Journal of Radiation Oncology Biology Physics **64**, 1211–1220 (2006).
- [89]. JM Houle and A. Strong. *Clinical pharmacokinetics of verteporfin*. The Journal of Clinical Pharmacology **42**, 547–557 (2002).
- [90]. L. Ayaru. *Photodynamic therapy using verteporfin photosensitization in the pancreas and surrounding tissues in the Syrian golden hamster*. Pancreatology **7**, 20–27 (2007).
- [91]. VH Fingar, PK Kik, PS Haydon, PB Cerrito, M. Tseng, E. Abang and TJ Wieman. *Analysis of acute vascular damage after photodynamic therapy using benzoporphyrin derivative (BPD)*. British journal of cancer **79**, 1702 (1999).
- [92]. T.J. Dougherty, C.J. Gomer, B.W. Henderson, G. Jori, D. Kessel, M. Korbelik, J. Moan and Q. Peng. *Photodynamic therapy*. J Natl Cancer Inst **90**, 889–905 (1998).
- [93]. S. Mitra and T.H. Foster. *Photophysical parameters, photosensitizer retention and tissue optical properties completely account for the higher photodynamic efficacy of meso-tetra-hydroxyphenyl-chlorin vs Photofrin*. Photochem Photobiol **81**, 849–859 (2005).
- [94]. Q. Chen, Z. Huang, D. Luck, J. Beckers, P.H. Brun, B.C. Wilson, A. Scherz, Y. Salomon and F.W. Hetzel. *Preclinical studies in normal canine prostate of a novel palladium-bacteriopheophorbide (WST09) photosensitizer for photodynamic therapy of prostate cancer*. Photochem Photobiol **76**, 438–445 (2002).
- [95]. Z. Huang, Q. Chen, D. Luck, J. Beckers, B.C. Wilson, N. Trncic, S.M. Larue, D. Blanc and F.W. Hetzel. *Studies of a vascular-acting photosensitizer, Pd-bacteriopheophorbide (Tookad), in normal canine prostate and spontaneous canine prostate cancer*. Lasers Surg Med **36**, 390–397 (2005).
- [96]. F. Borle. *Evaluation of the photosensitizer Tookad (R) for photodynamic therapy on the Syrian golden hamster cheek pouch model: Light dose, drug dose and drug-light interval effects*. Photochemistry and Photobiology **78**, 377–383 (2003).
- [97]. P.H. Brun, J.L. DeGroot, E.F.G. Dickson, M. Farahani and R.H. Potier. *Determination of the in vivo pharmacokinetics of palladium-bacteriopheophorbide (WST09) in EMT6 tumour-bearing Balb/c mice using graphite furnace atomic absorption spectroscopy*. Photochemical and Photobiological Sciences **3**, 1006–1010 (2004).
- [98]. Ohad Mazor, Alexander Brandis, Vicki Plaks, Eran Neumark, Varda Rosenbach-Belkin, Yoram Salomon and Avigdor Scherz. *WST11, a novel water-soluble bacteriochlorophyll derivative; cellular uptake, pharmacokinetics, biodistribution and vascular-targeted photodynamic activity using melanoma tumors as a model*. Photochem Photobiol **81**, 342–351 (2005).
- [99]. I. Ashur, R. Goldschmidt, I. Pinkas, Y. Salomon, G. Szweczyk, T. Sarna and A. Scherz. *Photocatalytic Generation of Oxygen Radicals by the Water-Soluble Bacteriochlorophyll Derivative WST11, Noncovalently Bound to Serum Albumin*. The Journal of Physical Chemistry A **113**, 8027–8037 (2009).
- [100]. SW Young, KW Woodburn, M. Wright, TD Mody, Q. Fan, JL Sessler,

- WC Dow and RA Miller. *Lutetium texaphyrin (PCI-0123): a near-infrared, water-soluble photosensitizer*. *Photochemistry and photobiology* **63**, 892–897 (1996).
- [101]. J.C. Finlay, T.C. Zhu, A. Dimofte, D. Stripp, S.B. Malkowcz, T.M. Busch and S.M. Hahn. *Interstitial fluorescence spectroscopy in the human prostate during motexafin lutetium-mediated photodynamic therapy*. *Photochem Photobiol* **82**, 1270–1278 (2006).
- [102]. R. A. Hsi, A. Kapatkin, J. Strandberg, T. Zhu, T. Vulcan, M. Solonenko, C. Rodriguez, J. Chang, M. Saunders, N. Mason and S. Hahn. *Photodynamic therapy in the canine prostate using motexafin lutetium*. *Clin Cancer Res* **7**, 651–660 (2001).
- [103]. KW Woodburn, Q. Fan, D. Kessel, M. Wright, TD Mody, G. Hemmi, D. Magda, JL Sessler, WC Dow, RA Miller et al. *Phototherapy of cancer and atheromatous plaque with texaphyrins*. *Journal of clinical laser medicine & surgery* **14**, 343–348 (1996).
- [104]. S.W. Young, M.K. Sidhu, F. Qing, H.H. Muller, M. Neuder, G. Zanassi, TD Mody, G. Hemmi, W. Dow, JD Mutch et al. *Preclinical evaluation of gadolinium (III) texaphyrin complex: a new paramagnetic contrast agent for magnetic resonance imaging*. *Investigative radiology* **29**, 330–330 (1994).
- [105]. A.E. O'Connor, W.M. Gallagher and A.T. Byrne. *Invited Review Porphyrin and Nonporphyrin Photosensitizers in Oncology: Preclinical and Clinical Advances in Photodynamic Therapy*. *Photochemistry and Photobiology* **85**, 1053–1074 (2009).
- [106]. D. Kessel and RD Poretz. *Sites of photodamage induced by photodynamic therapy with a chlorin e6 triacetoxymethyl ester (CAME)*. *Photochemistry and Photobiology* **71**, 94–96 (2000).
- [107]. A.P. Castano, T.N. Demidova and M.R. Hamblin. *Mechanisms in photodynamic therapy: part two—cellular signaling, cell metabolism and modes of cell death*. *Photodiagnosis and Photodynamic Therapy* **2**, 1–23 (2005).
- [108]. K. Plaetzer, T. Kiesslich, B. Krammer and P. Hammerl. *Characterization of the cell death modes and the associated changes in cellular energy supply in response to ALPcS 4-PDT*. *Photochemical & Photobiological Sciences* **1**, 172–177 (2002).
- [109]. S. Marchal, A. Fadloun, E. Maugain, M.A. D'Hallewin, F. Guillemin and L. Bezdetnaya. *Necrotic and apoptotic features of cell death in response to Foscan((R)) photo sensitization of HT29 monolayer and multicell spheroids*. *Biochem Pharmacol* **69**, 1167–1176 (2005).
- [110]. E. Buytaert, M. Dewaele and P. Agostinis. *Molecular effectors of multiple cell death pathways initiated by photodynamic therapy*. *BBA-Reviews on Cancer* **1776**, 86–107 (2007).
- [111]. D. Kessel and Y. Luo. *Mitochondrial photodamage and PDT-induced apoptosis*. *Journal of photochemistry and photobiology. B, Biology* **42**, 89 (1998).
- [112]. V.H. Fingar, T.J. Wieman, P.S. Karavolos, K.W. Doak, R. Ouellet and J.E. Lier. *The effects of photodynamic therapy using differently substituted zinc phthalocyanines on vessel constriction, vessel leakage and tumor response*. *Photochemistry and photobiology* **58**, 251–258 (1993).
- [113]. K.S. McMahon, T.J. Wieman, P.H. Moore and V.H. Fingar. *Effects of photodynamic therapy using mono-L-aspartyl chlorin e6 on vessel constriction, vessel leakage, and tumor response*. *Cancer Research* **54**, 5374–5379 (1994).
- [114]. C. Abels. *Targeting of the vascular system of solid tumours by photo-*

- dynamic therapy (PDT)*. *Photochemical and Photobiological Sciences* **3**, 765–771 (2004).
- [115]. A.P. Castano, P. Mroz and M.R. Hamblin. *Photodynamic therapy and anti-tumour immunity*. *Nature Reviews Cancer* **6**, 535–545 (2006).
- [116]. P.C. Kousis, B.W. Henderson, P.G. Maier and S.O. Gollnick. *Photodynamic therapy enhancement of antitumor immunity is regulated by neutrophils*. *Cancer Research* **67**, 10501 (2007).
- [117]. I. Cecic, CS Parkins and M. Korbek. *Induction of systemic neutrophil response in mice by photodynamic therapy of solid tumors*. *Photochemistry and photobiology* **74**, 712 (2001).
- [118]. A.P. Castano, P. Mroz, M.X. Wu and M.R. Hamblin. *Photodynamic therapy plus low-dose cyclophosphamide generates antitumor immunity in a mouse model*. *Proceedings of the National Academy of Sciences* **105**, 5495 (2008).
- [119]. M. Korbek, G. Kros, J. Kros and G.J. Dougherty. *The role of host lymphoid populations in the response of mouse EMT6 tumor to photodynamic therapy*. *Cancer Research* **56**, 5647–5652 (1996).
- [120]. M. Korbek and GJ Dougherty. *Photodynamic therapy-mediated immune response against subcutaneous mouse tumors*. *Cancer research* **59**, 1941 (1999).
- [121]. K.M. Case and P.F. Zweifel. *Linear transport theory*. Addison-Wesley Educational Publishers Inc., US (1967).
- [122]. A. Ishimaru. *Wave propagation and scattering in random media*. Academic Press (1978).
- [123]. SL Jacques, CA Alter and SA Prahl. *Angular dependence of HeNe laser light scattering by human dermis*. *Lasers Life Sci* **1**, 309–333 (1987).
- [124]. Scott A. Prahl. *Light transport in tissue*. PhD thesis University of Texas at Austin (1988).
- [125]. L. Heyney and JL Greenstein. *Diffuse radiation in the galaxy*. *Astrophysics Journal* **93**, 70–83 (1941).
- [126]. S.R. Arridge. *Optical tomography in medical imaging*. *Inverse Probl* **15**, R41–R93 (1999).
- [127]. M. Schweiger, S.R. Arridge, M. Hiraoka and D.T. Delpy. *The Finite-Element Method for the Propagation of Light in Scattering Media - Boundary and Source Conditions*. *Med Phys* **22**, 1779–1792 (1995).
- [128]. Tanja Tarvainen. *Computational methods for light transport in optical tomography*. PhD thesis University of Kuopio (2006).
- [129]. T. Durduran, A.G. Yodh, B. Chance and D.A. Boas. *Does the photon-diffusion coefficient depend on absorption?* *Journal of the Optical Society of America A* **14**, 3358–3365 (1997).
- [130]. R. Aronson and N Corngold. *Photon diffusion coefficient in an absorbing medium*. *Journal of the Optical Society of America A* **16**, 1066–1071 (1999).
- [131]. J.B. Fishkin and E. Gratton. *Propagation of photon-density waves in strongly scattering media containing an absorbing semi-infinite plane bounded by a straight edge*. *Journal of the Optical Society of America A* **10**, 127–140 (1993).
- [132]. M. Keijzer, W.M. Star and P.R.M. Storchi. *Optical diffusion in layered media*. *Appl Opt* **27**, 1820–1824 (1988).
- [133]. A.D. Klöse, V. Ntziachristos and A.H. Hielscher. *The inverse source problem based on the radiative transfer equation in optical molecular imaging*. *Journal of Computational Physics* **202**, 323–345 (2005).
- [134]. M.S. Patterson, B. Chance and B.C. Wilson. *Time resolved reflectance and transmittance for the non-invasive measurement of tissue optical*

- properties*. Appl Opt **28**, 2331–2336 (1989).
- [135]. R.C. Haskell, L.O. Svaasand, T.-T. Tsay, T.-C. Feng, M.S. McAdams and B.J. Tromberg. *Boundary conditions for the diffusion equation in radiative transfer*. Journal of the Optical Society of America A **11**, 2727–2741 (1994).
- [136]. A. Kienle and M.S. Patterson. *Improved solutions of the steady-state and the time-resolved diffusion equations for reflectance from a semi-infinite turbid medium*. Journal of the Optical Society of America A **14**, 246–254 (1997).
- [137]. A. H. Hielscher, S. L. Jacques, L. Wang and F. K. Tittel. *The influence of boundary conditions on the accuracy of diffusion theory in time-resolved reflectance spectroscopy of biological tissues*. Phys Med Biol **40**, 1957–1975 (1995).
- [138]. T. Nakai, G. Nishimura, K. Yamamoto and M. Tamura. *Expression of optical diffusion coefficient in high-absorption turbid media*. Phys Med Biol **42**, 2541–2549 (1997).
- [139]. J. Ripoll, D. Yessayan, G. Zacharakis and V. Ntziachristos. *Experimental determination of photon propagation in highly absorbing and scattering media*. Journal of the Optical Society of America A **22**, 546–551 (2005).
- [140]. E. Alerstam, S. Andersson-Engels and T. Svensson. *Improved accuracy in time-resolved diffuse reflectance spectroscopy*. Opt Express **16**, 10440–10454 (2008).
- [141]. T.J. Farrell, M.S. Patterson and B. Wilson. *A diffusion theory model of spatially resolved, steady-state diffuse reflectance for noninvasive determination of tissue optical properties in vivo*. Med Phys **19**, 879–888 (1992).
- [142]. Hamid Dehghani, Matthew E. Eames, Phaneendra K. Yalavarthy, Scott C. Davis, Subhadra Srinivasan, Colin M. Carpenter, Brian W. Pogue and Keith D. Paulsen. *Near infrared optical tomography using NIRFAST: Algorithm for numerical model and image reconstruction*. Communications in Numerical Methods in Engineering **9999**, n/a (2008).
- [143]. A.D. Klose and E.W. Larsen. *Light transport in biological tissue based on the simplified spherical harmonics equations*. Journal of Computational Physics **220**, 441–470 (2006).
- [144]. H. P. Xu and M. S. Patterson. *Application of the modified spherical harmonics method to some problems in biomedical optics*. Physics in Medicine and Biology **51**, N247–N251 (2006).
- [145]. A.D. Klose and A.H. Hielscher. *Iterative reconstruction scheme for optical tomography based on the equation of radiative transfer*. Medical Physics **26**, 1698 (1999).
- [146]. A.D. Klose, U. Netz, J. Beuthan and A.H. Hielscher. *Optical tomography using the time-independent equation of radiative transfer—Part 1: Forward model*. Journal of Quantitative Spectroscopy and Radiative Transfer **72**, 691–713 (2002).
- [147]. L. Wang and S.L. Jacques. *Hybrid model of Monte Carlo simulation and diffusion theory for light reflectance by turbid media*. Journal of the Optical Society of America A **10**, 1746–1752 (1993).
- [148]. T. Tarvainen, M. Vauhkonen, V. Kolehmainen, S. R. Arridge and J. P. Kaipio. *Coupled radiative transfer equation and diffusion approximation model for photon migration in turbid medium with low-scattering and non-scattering regions*. Physics in Medicine and Biology **50**, 4913–4930 (2005).
- [149]. T. Tarvainen, M. Vauhkonen, V. Kolehmainen and J. P. Kaipio. *Finite*

- element model for the coupled radiative transfer equation and diffusion approximation*. International Journal for Numerical Methods in Engineering **65**, 383–405 (2006).
- [150]. SA Prahl, M. Keijzer, SL Jacques and AJ Welch. *A Monte Carlo model of light propagation in tissue*. Proc. SPIE, Dosimetry of Laser Radiation in Medicine and Biology **IS 5**, 102–111 (1989).
- [151]. L. Wang, S.L. Jacques and L. Zheng. *MCML—Monte Carlo modeling of light transport in multi-layered tissues*. Computer Methods and Programs in Biomedicine **47**, 131–146 (1995).
- [152]. Steven L. Jacques. *Light Distributions from Point, Line and Plane Sources for Photochemical Reactions and Fluorescence in Turbid Biological Tissues*. Photochemistry and Photobiology **67**, 23 – 32 (1998).
- [153]. J. Swartling, A. Pifferi, A.M.K. Enejder and S. Andersson-Engels. *Accelerated Monte Carlo model to simulate fluorescence spectra from layered tissues*. Journal of the Optical Society of America A **20**, 714–727 (2003).
- [154]. David Boas, J. Culver, J. Stott and A. Dunn. *Three dimensional Monte Carlo code for photon migration through complex heterogeneous media including the adult human head*. Opt. Express **10**, 159–170 (2002).
- [155]. E. Alerstam, T. Svensson and S. Andersson-Engels. *Parallel computing with graphics processing units for high-speed Monte Carlo simulation of photon migration*. Journal of Biomedical Optics **13**, 060504 (2008).
- [156]. William Chun Yip Lo, Keith Redmond, Jason Luu, Paul Chow, Jonathan Rose and Lothar Lilge. *Hardware acceleration of a Monte Carlo simulation for photodynamic therapy treatment planning*. Journal of Biomedical Optics **14**, 014019 (2009).
- [157]. R.W. Clough. *The finite element method in plane stress analysis*. Conference on Electronic Computation, Pittsburgh **2nd** (1960).
- [158]. OC Zienkiewicz and YK Cheung. *Finite elements in the solution of field problems*. The Engineer **220**, 507–510 (1965).
- [159]. Comsol. *Multiphysics 3.4*. www.comsol.com (2009).
- [160]. S.R. Arridge, M. Schweiger, M. Hiraoka and D.T. Delpy. *A finite element approach for modeling photon transport in tissue*. Med Phys **20**, 299–309 (1993).
- [161]. TOAST. *Time-resolved Optical Absorption and Scattering Tomography*. <http://web4.cs.ucl.ac.uk/research/vis/toast/index.html> (2009).
- [162]. NIRFAST. *Near Infrared Frequency Domain Absorption and Scatter Tomography*. <http://www.dartmouth.edu/nir/nirfast/> (2009).
- [163]. D.G. Duffy. *Green's functions with applications*. CRC Press (2001).
- [164]. S.R. Arridge, M. Cope and D.T. Delpy. *The theoretical basis for the determination of optical pathlengths in tissue: temporal and frequency analysis*. Phys Med Biol **37**, 1531–1560 (1992).
- [165]. Jorge Ripoll. *Light diffusion in turbid media with biomedical application*. PhD thesis Universidad Autonoma de Madrid (2000).
- [166]. D. Contini, F. Martelli and G. Zaccanti. *Photon migration through a turbid slab described by a model based on diffusion approximation . 1. Theory*. Appl Opt **36**, 4587–4599 (1997).
- [167]. A.J. Welch, C.M. Gardner, R. Richards-Kortum, E. Chan, G. Criswell, J. Pfefer and S. Warren. *Propagation of fluorescence light*. Lasers Surg Med **21**, 166–178 (1997).
- [168]. M.S. Patterson and B.W. Pogue. *Mathematical model for time-resolved and frequency-domain fluorescence spectroscopy in biological tissues*. Appl Opt **33**, 1963–1974 (1994).
- [169]. E.M. Sevick-Muraca and C.L. Burch. *Origin of phosphorescence signals*

- reemitted from tissues. *Optics Letters* **19**, 1928–1930 (1994).
- [170]. CL Hutchinson, JR Lakowicz and EM Sevick-Muraca. *Fluorescence lifetime-based sensing in tissues: a computational study*. *Biophysical Journal* **68**, 1574–1582 (1995).
- [171]. M.A. O’Leary, D.A. Boas, X.D. Li, B. Chance and A.G. Yodh. *Fluorescence lifetime imaging in turbid media*. *Opt Lett* **21**, 158–160 (1996).
- [172]. X. D. Li, M. A. O’Leary, D. A. Boas, B. Chance and A. G. Yodh. *Fluorescent diffuse photon density waves in homogeneous and heterogeneous turbid media: analytic solutions and applications*. *Appl. Opt.* **35**, 3746–3758 (1996).
- [173]. K.R. Diamond, T.J. Farrell and M.S. Patterson. *Measurement of fluorophore concentrations and fluorescence quantum yield in tissue-simulating phantoms using three diffusion models of steady-state spatially resolved fluorescence*. *Phys Med Biol* **48**, 4135–4149 (2003).
- [174]. J. Wu, M.S. Feld and R.P. Rava. *Analytical model for extracting intrinsic fluorescence in turbid media*. *Appl Opt* **32**, 3585–3595 (1993).
- [175]. D.E. Hyde, T.J. Farrell, M.S. Patterson and B.C. Wilson. *A diffusion theory model of spatially resolved fluorescence from depth-dependent fluorophore concentrations*. *Phys Med Biol* **46**, 369–383 (2001).
- [176]. D. Stasic, T.J. Farrell and M.S. Patterson. *The use of spatially-resolved fluorescence and reflectance to determine interface depth in layered fluorophore distributions*. *Phys Med Biol* **48**, 3459–3474 (2003).
- [177]. A. D. Klose and A. H. Hielscher. *Fluorescence tomography with simulated data based on the equation of radiative transfer*. *Opt Lett* **28**, 1019–1021 (2003).
- [178]. J.C. Rasmussen, A. Joshi, T. Pan, T. Wareing, J. McGhee and E.M. Sevick-Muraca. *Radiative transport in fluorescence-enhanced frequency domain photon migration*. *Medical Physics* **33**, 4685 (2006).
- [179]. R.J. Crilly, W.F. Cheong, B. Wilson and J.R. Spears. *Forward-adjoint fluorescence model: Monte Carlo integration and experimental validation*. *Appl Opt* **36**, 6513–6519 (1997).
- [180]. I.J. Bigio and S.G. Bown. *Spectroscopic sensing of cancer and cancer therapy*. *Cancer Biol. Ther* **3**, 259–267 (2004).
- [181]. TJ Pfefer, LS Matchette, AM Ross and MN Ediger. *Selective detection of fluorophore layers in turbid media: the role of fiber-optic probe design*. *Optics letters* **28**, 120 (2003).
- [182]. P.R. Bargo, S.A. Prahl and S.L. Jacques. *Optical properties effects upon the collection efficiency of optical fibers in different probe configurations*. *IEEE Journal of Selected Topics in Quantum Electronics* **9**, 314–321 (2003).
- [183]. P.R. Bargo, S.A. Prahl and S.L. Jacques. *Collection efficiency of a single optical fiber in turbid media*. *Applied optics* **42**, 3187–3197 (2003).
- [184]. T.J. Pfefer, K.T. Schomacker, M.N. Ediger and N.S. Nishioka. *Light propagation in tissue during fluorescence spectroscopy with single-fiber probes*. *IEEE J Sel Topics in Quantum Electron* **7**, 1004–1012 (2001).
- [185]. JR Mourant, IJ Bigio, DA Jack, TM Johnson and HD Miller. *Measuring absorption coefficients in small volumes of highly scattering media: source-detector separations for which path lengths do not depend on scattering properties*. *Applied optics* **36**, 5655 (1997).
- [186]. J. Ankerst, S. Montan, K. Svanberg and S. Svanberg. *Laser-induced fluorescence studies of hematoporphyrin derivative (HpD) in normal and tumor tissue of rat*. *Applied Spectroscopy* **38**, 890–896 (1984).
- [187]. C. af Klinteberg, A.M.K. Enejder, I. Wang, S. Andersson-Engels, S. Svanberg and K. Svanberg. *Kinetic fluorescence studies of 5-*

- aminolaevulinic acid-induced protoporphyrin IX accumulation in basal cell carcinomas*. Journal of Photochemistry and Photobiology B: Biology **49**, 120–128 (1999).
- [188]. C. af Klinteberg, M. Andreasson, O. Sandstrom, S. Andersson-Engels and S. Svanberg. *Compact medical fluorosensor for minimally invasive tissue characterization*. Review of Scientific Instruments **76**, 034303 (2005).
- [189]. S. Andersson, S. Montan and S. Svanberg. *Multispectral System for Medical Fluorescence imaging*. IEEE journal of quantum electronics **23**, 1798–1805 (1987).
- [190]. S. Andersson-Engels, J. Johansson and S. Svanberg. *Medical diagnostic system based on simultaneous multispectral fluorescence imaging*. Applied Optics **33**, 8022–8029 (1994).
- [191]. R. Baumgartner, H. Fisslinger, D. Jocham, H. Lenz, L. Ruprecht, H. Stepp and E. Unsold. *A fluorescence imaging device for endoscopic detection of early stage cancer-instrumental and experimental studies*. Photochemistry and Photobiology **46**, 759–763 (1987).
- [192]. T. Vo-Dinh, B. Cullum and P. Kasili. *Development of a multi-spectral imaging system for medical applications*. Journal of Physics D **36**, 1663–1668 (2003).
- [193]. G. Zavattini, S. Vecchi, G. Mitchell, U. Weisser, R. M. Leahy, B. J. Pichler, D. J. Smith and S. R. Cherry. *A hyperspectral fluorescence system for 3D in vivo optical imaging*. Physics in Medicine and Biology **51**, 2029–2043 (2006).
- [194]. S. Andersson-Engels, C. Klinteberg, K. Svanberg and S. Svanberg. *In vivo fluorescence imaging for tissue diagnostics*. Physics in Medicine and Biology **42**, 815–824 (1997).
- [195]. A. Bogaards, M.C. Aalders, A.J.L. Jongen, E. Dekker and H.J.C.M. Sterenberg. *Double ratio fluorescence imaging for the detection of early superficial cancers*. Rev Sci Instrum **72**, 3956–3961 (2001).
- [196]. D.R. Lynch. *Numerical partial differential equations for environmental scientists and engineers: a first practical course*. Springer Verlag (2005).
- [197]. J.P.A. Marijnissen and W.M. Star. *Calibration of isotropic light dosimetry probes based on scattering bulbs in clear media*. Phys Med Biol **41**, 1191–1208 (1996).
- [198]. A. Dimofte, J.C. Finlay and T.C. Zhu. *A method for determination of the absorption and scattering properties interstitially in turbid media*. Phys Med Biol **50**, 2291–2311 (2005).
- [199]. T. Svensson, M. Einarsdottir, K. Svanberg and S. Andersson-Engels. *In vivo optical characterization of human prostate tissue using near-infrared time-resolved spectroscopy*. J Biomed Opt **12**, 014022–1–014022–10 (2007).
- [200]. C. D’Andrea, D. Comelli, A. Pifferi, A. Torricelli, G. Valentini and R. Cubeddu. *Time-resolved optical imaging through turbid media using a fast data acquisition system based on a gated CCD camera*. Journal of Physics D **36**, 1675–1681 (2003).
- [201]. Tomas Svensson. *Pharmaceutical and biomedical applications of spectroscopy in the photon migration regime*. PhD thesis Lund University (2008).
- [202]. Tuan H. Pham, Olivier Coquoz, Joshua B. Fishkin, Eric Anderson and Bruce J. Tromberg. *Broad bandwidth frequency domain instrument for quantitative tissue optical spectroscopy*. Review of Scientific Instruments **71**, 2500–2513 (2000).
- [203]. J.C. Finlay and T.H. Foster. *Recovery of hemoglobin oxygen saturation*

- and intrinsic fluorescence with a forward-adjoint model. *Applied optics* **44**, 1917–1933 (2005).
- [204]. K.R. Diamond, M.S. Patterson and T.J. Farrell. *Quantification of fluorophore concentration in tissue-simulating media by fluorescence measurements with a single optical fiber*. *Appl Opt* **42**, 2436–2442 (2003).
- [205]. R. Weersink, M.S. Patterson, K. Diamond, S. Silver and N. Padgett. *Noninvasive measurement of fluorophore concentration in turbid media with a simple fluorescence/reflectance ratio technique*. *Appl Opt* **40**, 6389–6395 (2001).
- [206]. A.P. Gibson, J.C. Hebden and S.R. Arridge. *Recent advances in diffuse optical imaging*. *Phys Med Biol* **50**, R1–43 (2005).
- [207]. A. C. Kak and M. Slaney. *Principles of Computerized Tomographic Imaging*. IEEE Press (1988).
- [208]. A.P. Gibson, J.C. Hebden, J. Riley, N. Everdell, M. Schweiger, S.R. Arridge and D.T. Delpy. *Linear and nonlinear reconstruction for optical tomography of phantoms with nonscattering regions*. *Appl Opt* **44**, 3925–3936 (2005).
- [209]. S. A. Walker, S. Fantini and E. Gratton. *Image reconstruction by back-projection from frequency-domain optical measurements in highly scattering media*. *Applied Optics* **36**, 170–179 (1997).
- [210]. R.J. Gaudette, DH Brooks, CA DiMarzio, ME Kilmer, EL Miller, T Gaudette and DA Boas. *A comparison study of linear reconstruction techniques for diffuse optical tomographic imaging of absorption coefficient*. *Phys Med Biol* **45**, 1051–1070 (2000).
- [211]. D.A. Boas. *A fundamental limitation of linearized algorithms for diffuse optical tomography*. *Opt Express* **1**, 404–413 (1997).
- [212]. J. Hadamard. *Lectures on Cauchy's Problem in Linear Partial Differential Equations*. Yale university press (1923).
- [213]. H.W. Engl, M. Hanke and A. Neubauer. *Regularization of inverse problems*. Kluwer Academic Pub (1996).
- [214]. P.C. Hansen. *REGULARIZATION TOOLS: A Matlab package for analysis and solution of discrete ill-posed problems*. *Numerical Algorithms* **6**, 1–35 (1994).
- [215]. A.N. Tikhonov, V.Y. Arsenin and F. John. *Solutions of ill-posed problems*. VH Winston Washington, DC (1977).
- [216]. B.A. Brooksby. *Combining near infrared tomography and magnetic resonance imaging to improve breast tissue chromophore and scattering assessment*. PhD thesis Thayer School of Engineering, Dartmouth College (2005).
- [217]. Simon R. Arridge. *Photon-measurement density functions. Part I: Analytical forms*. *Appl. Opt.* **34**, 7395–7409 (1995).
- [218]. S.R. Arridge and M. Schweiger. *Photon-measurement density functions. Part 2: Finite-element-method calculations*. *Appl Opt* **34**, 8026–8037 (1995).
- [219]. V. Ntziachristos and R. Weissleder. *Experimental three-dimensional fluorescence reconstruction of diffuse media by use of a normalized Born approximation*. *Opt Lett* **26**, 893–895 (2001).
- [220]. A. Soubret, J. Ripoll and V. Ntziachristos. *Accuracy of fluorescent tomography in the presence of heterogeneities: study of the normalized Born ratio*. *IEEE T Med Imaging* **24**, 1377–1386 (2005).
- [221]. S.R. Arridge and J.C. Hebden. *Optical imaging in medicine: II. Modelling and reconstruction*. *Phys Med Biol* **42**, 841–853 (1997).
- [222]. S.C. Davis, H. Deghani, J. Wang, S. Jiang, B. W. Pogue and K. D. Paulsen. *Image-guided diffuse optical fluorescence tomography imple-*

- mented with Laplacian-type regularization. *Opt Express* **15**, 4066–4082 (2007).
- [223]. A Corlu, R. Choe, T. Durduran, K Lee, M. Schweiger, S.R. Arridge, E.M.C. Hillman and A.G. Yodh. *Diffuse optical tomography with spectral constraints and wavelength optimization*. *Appl Opt* **44**, 2082–2093 (2005).
- [224]. S. Srinivasan, B.W. Pogue, S.D. Jiang, H. Dehghani and K.D. Paulsen. *Spectrally constrained chromophore and scattering near-infrared tomography provides quantitative and robust reconstruction*. *Appl Opt* **44**, 1858–1869 (2005).
- [225]. H. Dehghani, S.C. Davis and B.W. Pogue. *Spectrally resolved bioluminescence tomography using the reciprocity approach*. *Medical Physics* **35**, 4863 (2008).
- [226]. Anand T. Kumar, Scott B. Raymond, Gregory Boverman, David A. Boas and Brian J. Bacsikai. *Time resolved fluorescence tomography of turbid media based on lifetime contrast*. *Opt. Express* **14**, 12255–12270 (2006).
- [227]. J.D. Bronzino. *The biomedical engineering handbook*. Springer (2000).
- [228]. Zhun Xu and Jing Bai. *Analysis of finite-element-based methods for reducing the ill-posedness in the reconstruction of fluorescence molecular tomography*. *Progress in Natural Science* **19**, 501 – 509 (2009).
- [229]. P.C. Hansen and D.P. O’Leary. *The use of the L-curve in the regularization of discrete ill-posed problems*. *SIAM Journal on Scientific Computing* **14**, 1487 (1993).
- [230]. J.P. Culver, R. Choe, M.J. Holboke, L. Zubkov, T. Durduran, A. Slemph, V. Ntziachristos, B. Chance and A.G. Yodh. *Three-dimensional diffuse optical tomography in the parallel plane transmission geometry: evaluation of a hybrid frequency domain/continuous wave clinical system for breast imaging*. *Med Phys* **30**, 235–247 (2003).
- [231]. Alexei V Chvetsov. *L-curve analysis of radiotherapy optimization problems*. *Med Phys* **32**, 2598–2605 (2005).
- [232]. L. Hu, H. Wang, B. Zhao and W. Yang. *A hybrid reconstruction algorithm for electrical impedance tomography*. *Measurement Science and Technology* **18**, 813–818 (2007).
- [233]. Phaneendra K. Yalavarthy, Brian W. Pogue, Hamid Dehghani, Colin M. Carpenter, Shudong Jiang and Keith D. Paulsen. *Structural information within regularization matrices improves near infrared diffuse optical tomography*. *Opt. Express* **15**, 8043–8058 (2007).
- [234]. B.W. Pogue, T.O. McBride, J. Prewitt, U.L. Osterberg and K.D. Paulsen. *Spatially variant regularization improves diffuse optical tomography*. *Appl Opt* **38**, 2950–2961 (1999).
- [235]. Dax S Kepshire, Scott C Davis, Hamid Dehghani, Keith D Paulsen and Brian W Pogue. *Subsurface diffuse optical tomography can localize absorber and fluorescent objects but recovered image sensitivity is nonlinear with depth*. *Appl Opt* **46**, 1669–1678 (2007).
- [236]. H. Dehghani, B.R. White, B.W. Zeff, A. Tizzard and J.P. Culver. *Depth sensitivity and image reconstruction analysis of dense imaging arrays for mapping brain function with diffuse optical tomography*. *Applied Optics* **48**, 137–143 (2009).
- [237]. B.W. Pogue and K.D. Paulsen. *High-resolution near-infrared tomographic imaging simulations of the rat cranium by use of a priori magnetic resonance imaging structural information*. *Optics letters* **23**, 1716–1718 (1998).
- [238]. Yuting Lin, Han Yan, Orhan Nalcioglu and Gultekin Gulsen. *Quantitative fluorescence tomography with functional and structural a priori*

- information. *Appl. Opt.* **48**, 1328–1336 (2009).
- [239]. B. Brooksby, S.D. Jiang, H. Dehghani, B.W. Pogue, K.D. Paulsen, J. Weaver, C. Kogel and S.P. Poplack. *Combining near-infrared tomography and magnetic resonance imaging to study in vivo breast tissue implementation of a Laplacian-type regularization to incorporate magnetic resonance structure*. *J Biomed Opt* **10**, 1–10 (2005).
- [240]. P. K. Yalavarthy, B. W. Pogue, H. Dehghani and K. D. Paulsen. *Weight-matrix structured regularization provides optimal generalized least-squares estimate in diffuse optical tomography*. *Med Phys* **34**, 2085–2098 (2007).
- [241]. Phaneendra K. Yalavarthy. *A generalized least-squares minimization method for near infrared diffuse optical tomography*. PhD thesis Thayer School of Engineering (2007).
- [242]. J. C. Ye, K. J. Webb, C. A. Bouman and R. P. Millane. *Optical diffusion tomography by iterative-coordinate-descent optimization in a Bayesian framework*. *Journal of the Optical Society of America a-Optics Image Science and Vision* **16**, 2400–2412 (1999).
- [243]. Adam B Milstein, Seungseok Oh, Jeffery S Reynolds, Kevin J Webb, Charles A Bouman and Rick P Millane. *Three-dimensional Bayesian optical diffusion tomography with experimental data*. *Opt Lett* **27**, 95–97 (2002).
- [244]. A.B. Milstein, O. Seungseok, K.J. Webb, C.A. Bouman, Q. Zhang, D.A. Boas and R.P. Millane. *Fluorescence optical diffusion tomography*. *Appl Opt* **42**, 3081–3094 (2003).
- [245]. M. Guven, B. Yazici, X. Intes and B. Chance. *Diffuse optical tomography with a priori anatomical information*. *Phys Med Biol* **50**, 2837–2858 (2005).
- [246]. Xavier Intes, Clemence Maloux, Murat Guven, Birzen Yazici and Britton Chance. *Diffuse optical tomography with physiological and spatial a priori constraints*. *Phys Med Biol* **49**, N155–N163 (2004).
- [247]. DA Knoll and DE Keyes. *Jacobian-free Newton–Krylov methods: a survey of approaches and applications*. *Journal of Computational Physics* **193**, 357–397 (2004).
- [248]. Y. Saad. *Iterative methods for sparse linear systems*. Society for Industrial Mathematics (2003).
- [249]. HA Van der Vorst. *Iterative Krylov methods for large linear systems*. Cambridge Univ Pr (2003).
- [250]. Martin Schweiger, Simon R Arridge and Ilkka Nissilä. *Gauss-Newton method for image reconstruction in diffuse optical tomography*. *Phys Med Biol* **50**, 2365–2386 (2005).
- [251]. S. Arridge and M. Schweiger. *A General Framework for Iterative Reconstruction Algorithms in Optical Tomography, Using a Finite Element Method*. In F. Natterer C. Bergers, editor, *Computational Radiology and Imaging : therapy and Diagnosis*. IMA Volumes in Mathematics and its Applications Springer-Verlag (Berlin) (1998).
- [252]. A.H. Hielscher, A.D. Klose and K.M. Hanson. *Gradient-based iterative image reconstruction scheme for time-resolved optical tomography*. *IEEE T Med Imaging* **18**, 262–271 (1999).
- [253]. J. Califano, P. van der Riet, W. Westra, H. Nawroz, G. Clayman, S. Pilotadosi, R. Corio, D. Lee, B. Greenberg, W. Koch et al. *Genetic progression model for head and neck cancer: implications for field cancerization*. *Cancer research* **56**, 2488 (1996).
- [254]. George Themelis, Jung Sun Yoo and Vasilis Ntziachristos. *Multispectral imaging using multiple-bandpass filters*. *Opt. Lett.* **33**, 1023–1025 (2008).

- [255]. M. Kobayashi, H. Tajiri, E. Seike, M. Shitaya, S. Tounou, M. Mine and K. Oba. *Detection of early gastric cancer by a real-time autofluorescence imaging system*. *Cancer letters* **165**, 155–159 (2001).
- [256]. M.C. Pierce, D.J. Javier and R. Richards-Kortum. *Optical contrast agents and imaging systems for detection and diagnosis of cancer*. *Int J Cancer* **123**, 1979–1990 (2008).
- [257]. N. Thekkek and R. Richards-Kortum. *Optical imaging for cervical cancer detection: solutions for a continuing global problem*. *Nature reviews. Cancer* **8**, 725 (2008).
- [258]. D. Roblyer, R. Richards-Kortum, K. Sokolov, A.K. El-Naggar, M.D. Williams, C. Kurachi and A.M. Gillenwater. *Multispectral optical imaging device for in vivo detection of oral neoplasia*. *Journal of Biomedical Optics* **13**, 024019 (2008).
- [259]. C.S. Betz, H. Stepp, M. Havel, W. Jerjes, T. Upile, C. Hopper, R. Sroka and A. Leunig. *A set of optical techniques for improving the diagnosis of early upper aerodigestive tract cancer*. *Medical Laser Application* **23**, 175–185 (2008).
- [260]. M.A. Kara, F.P. Peters, P. Fockens, F.J.W. ten Kate and J.J. Bergman. *Endoscopic video-autofluorescence imaging followed by narrow band imaging for detecting early neoplasia in Barrett's esophagus*. *Gastrointestinal endoscopy* **64**, 176–185 (2006).
- [261]. K. Sokolov, J. Aaron, B. Hsu, D. Nida, A. Gillenwater, M. Follen, C. MacAulay, K. Adler-Storthz, B. Korgel, M. Descour, R. Pasqualini, W. Arap, W. Lam and R. Richards-Kortum. *Optical systems for in vivo molecular imaging of cancer*. *Technol Cancer Res Treat* **2**, 491–504 (2003).
- [262]. D. Zaak, D. Frimberger, H. Stepp, S. Wagner, R. Baumgartner, P. Schneede, M. Siebels, R. KN "UCHEL, M. Kriegmair and A. Hofstetter. *Quantification of 5-aminolevulinic acid induced fluorescence improves the specificity of bladder cancer detection*. *The Journal of urology* **166**, 1665–1669 (2001).
- [263]. S. Andersson-Engels, J. Johansson, K. Svanberg and S. Svanberg. *Fluorescence imaging and point measurements of tissue: applications to the demarcation of malignant tumors and atherosclerotic lesions from normal tissue*. *Photochemistry and photobiology* **53**, 807 (1991).
- [264]. C. Adam, G. Salomon, S. Walther, D. Zaak, W. Khoder, A. Becker, O. Reich, A. Blana, R. Ganzer, S. Denzinger et al. *Photodynamic diagnosis using 5-aminolevulinic acid for the detection of positive surgical margins during radical prostatectomy in patients with carcinoma of the prostate: A multicentre, prospective, phase 2 trial of a diagnostic procedure*. *European Urology* **55**, 1281–1288 (2009).
- [265]. A. Corlu, R. Choe, T. Durduran, M.A. Rosen, M. Schweiger, S.R. Arridge, M.D. Schnall and A.G. Yodh. *Three-dimensional in vivo fluorescence diffuse optical tomography of breast cancer in humans*. *Opt Express* **15**, 6696–6716 (2007).
- [266]. R. Roy, A. B. Thompson, A. Godavarty and E. M. Sevick-Muraca. *Tomographic fluorescence imaging in tissue phantoms: a novel reconstruction algorithm and imaging geometry*. *IEEE T Med Imaging* **24**, 137–154 (2005).
- [267]. J. Ge, S.J. Erickson and A. Godavarty. *Fluorescence Tomographic Imaging using a Hand-held Probe based Optical Imager: Extensive Phantom Studies*. *Appl. Opt* **48**, 6408–6416 (2009).
- [268]. X. Intes, S. Djeziri, Z. Ichalalene, N. Mincu, Y. Wang, P. St-Jean, F. Lesage, D. Hall, D. Boas, M. Polyzos et al. *Time-Domain Optical Mammography SoftScan: Initial Results*. *Academic Radiology* **12**,

- 934–947 (2005).
- [269]. B. Brooksby, B.W. Pogue, S. Jiang, H. Dehghani, S. Srinivasan, C. Kogel, T.D. Tosteson, J. Weaver, S.P. Poplack and K.D. Paulsen. *Imaging breast adipose and fibroglandular tissue molecular signatures by using hybrid MRI-guided near-infrared spectral tomography*. Proc.Natl Acad Sci U.S.A **103**, 8828–8833 (2006).
- [270]. T. Austin, A.P. Gibson, G. Branco, R.Md. Yusof, S.R. Arridge, J.H. Meek, J.S. Wyatt, D.T. Delpy and J.C. Hebden. *Three dimensional optical imaging of blood volume and oxygenation in the neonatal brain*. Neuroimage **31**, 1426–1433 (2006).
- [271]. Juliette Selb, Danny K Joseph and David A Boas. *Time-gated optical system for depth-resolved functional brain imaging*. J Biomed Opt **11**, 044008 (2006).
- [272]. R. Weissleder and M.J. Pittet. *Imaging in the era of molecular oncology*. Nature **452**, 580–589 (2008).
- [273]. C Kuo, O Coquoz, T L Troy, H Xu and B W Rice. *Three-dimensional reconstruction of in vivo bioluminescent sources based on multispectral imaging*. J Biomed Opt **12**, 024007–024007 (2007).
- [274]. D. Razansky, M. Distel, C. Vinegoni, R. Ma, N. Perrimon, R.W. Koster and V. Ntziachristos. *Multispectral opto-acoustic tomography of deep-seated fluorescent proteins in vivo*. Nature Photonics **3**, 412–417 (2009).
- [275]. K. Shah, A. Jacobs, X.O. Breakefield and R. Weissleder. *Molecular imaging of gene therapy for cancer*. Gene Ther **11**, 1175–1187 (2004).
- [276]. T.F. Massoud and S.S. Gambhir. *Molecular imaging in living subjects: seeing fundamental biological processes in a new light*. Genes & Development **17**, 545–580 (2003).
- [277]. K. Brindle. *New approaches for imaging tumour responses to treatment*. Nature Reviews Cancer **8**, 94–107 (2008).
- [278]. E.M. Sevick-Muraca and J.C. Rasmussen. *Molecular imaging with optics: primer and case for near-infrared fluorescence techniques in personalized medicine*. Journal of Biomedical Optics **13**, 041303 (2008).
- [279]. Robert M Hoffman. *Imaging tumor angiogenesis with fluorescent proteins*. APMIS **112**, 441–449 (2004).
- [280]. V. Ntziachristos, C. Bremer, E. Graves, J. Ripoll and R. Weissleder. *In vivo tomographic imaging of near-infrared fluorescent probes*. Molecular Imaging **1**, 82–88 (2002).
- [281]. E. Graves, J. Ripoll, R. Weissleder and V. Ntziachristos. *A submillimeter resolution fluorescence molecular imaging system for small animal imaging*. Med Phys **30**, 901–911 (2003).
- [282]. G. Zacharakis, H. Kambara, H. Shih, J. Ripoll, J. Grimm, Y. Saeki, R. Weissleder and V. Ntziachristos. *Volumetric tomography of fluorescent proteins through small animals in vivo*. Proc Natl Acad Sci U.S.A **102**, 18252–18257 (2005).
- [283]. V. Ntziachristos, C.-H. Tung, C. Bremer and R. Weissleder. *Fluorescence molecular tomography resolves protease activity in vivo*. Nat Med **8**, 757–760 (2002).
- [284]. Ralf B Schulz, Jorge Ripoll and Vasilis Ntziachristos. *Noncontact optical tomography of turbid media*. Opt Lett **28**, 1701–1703 (2003).
- [285]. R.B Schulz, J. Ripoll and V. Ntziachristos. *Experimental Fluorescence Tomography of Tissues With Noncontact Measurements*. IEEE T Med Imaging **23**, 492–500 (2004).
- [286]. Ralf B Schulz, Jörg Peter, Wolfhard Semmler, Cosimo D’Andrea, Gianluca Valentini and Rinaldo Cubeddu. *Comparison of noncontact and*

- fiber-based fluorescence-mediated tomography*. *Opt Lett* **31**, 769–771 (2006).
- [287]. Heiko Meyer, Anikitos Garofalakis, Giannis Zacharakis, Stylianos Psycharakis, Clio Mamalaki, Dimitris Kioussis, Eleftherios N Economou, Vasilis Ntziachristos and Jorge Ripoll. *Noncontact optical imaging in mice with full angular coverage and automatic surface extraction*. *Appl Opt* **46**, 3617–3627 (2007).
- [288]. Tobias Lasser, Antoine Soubret, Jorge Ripoll and Vasilis Ntziachristos. *Surface Reconstruction for free-space 360 degrees fluorescence molecular tomography and the effects of animal motion*. *IEEE Trans Med Imaging* **27**, 188–194 (2008).
- [289]. S. Bloch, F. Lesage, L. McIntosh, A. Gandjbakhche, K. Liang and S. Achilefu. *Whole-body fluorescence lifetime imaging of a tumor-targeted near-infrared molecular probe in mice*. *J Biomed Opt* **10**, 054003–1–054003–8 (2005).
- [290]. A.T.N. Kumar, E. Chung, S.B. Raymond, J.A.J.M. van de Water, K. Shah, D. Fukumura, R.K. Jain, B.J. Bacskai and D.A. Boas. *Feasibility of in vivo imaging of fluorescent proteins using lifetime contrast*. *Optics Letters* **34**, 2066–2068 (2009).
- [291]. D. Kepshire, S. Gibbs-Strauss, J. O’Hara, M. Hutchins, N. Mincu, F. Leblond, M. Khayat, H. Dehghani, S. Srinivasan and B. Pogue. *Imaging of glioma tumor with endogenous fluorescence tomography*. *Journal of Biomedical Optics* **14**, 30501–030501–3 (2009).
- [292]. D. Hyde, R. de Kleine, S.A. MacLaurin, E. Miller, D.H. Brooks, T. Krucker and V. Ntziachristos. *Hybrid FMT–CT imaging of amyloid- β plaques in a murine Alzheimer’s disease model*. *Neuroimage* **44**, 1304–1311 (2009).
- [293]. K.S. Samkoe, S.C. Davis, S. Srinivasan, J.A. O’Hara, T. Hasan and B.W. Pogue. *A study of MRI-guided diffuse fluorescence molecular tomography for monitoring PDT effects in pancreas cancer*. In *Proceedings of SPIE* p 73803M vol. 7380 (2009).
- [294]. D. L. Farkas, C. Du, G. W. Fisher, C. Lau, W. Niu, E. S. Wachman and R. M. Levenson. *Non-invasive image acquisition and advanced processing in optical bioimaging*. *Comput Med Imaging Graph* **22**, 89–102 (1998).
- [295]. James R Mansfield, Kirk W Gossage, Clifford C Hoyt and Richard M Levenson. *Autofluorescence removal, multiplexing, and automated analysis methods for in-vivo fluorescence imaging*. *J Biomed Opt* **10**, 41207 (2005).
- [296]. Abhijit J Chaudhari, Felix Darvas, James R Bading, Rex A Moats, Peter S Conti, Desmond J Smith, Simon R Cherry and Richard M Leahy. *Hyperspectral and multispectral bioluminescence optical tomography for small animal imaging*. *Phys Med Biol* **50**, 5421–5441 (2005).
- [297]. A. Corlu, T. Durduran, R. Choe, M. Schweiger, E.M.C. Hillman, S.R. Arridge and A.G. Yodh. *Uniqueness and wavelength optimization in continuous-wave multispectral diffuse optical tomography*. *Opt Lett* **28**, 2339–2341 (2003).
- [298]. H. Dehghani, S.C. Davis, S. Jiang, B.W. Pogue, K.D. Paulsen and M.S. Patterson. *Spectrally resolved bioluminescence optical tomography*. *Opt Lett* **31**, 365–367 (2006).
- [299]. J. Swartling, J. Svensson, D Bengtsson, K Terike and S. Andersson-Engels. *Fluorescence spectra provide information on the depth of fluorescent lesions in tissue*. *Appl Opt* **44**, 1934–1941 (2005).
- [300]. A.J. Chaudhari, S. Ahn, R. Levenson, R.D. Badawi, S.R. Cherry and R.M. Leahy. *Excitation spectroscopy in multispectral optical fluore-*

- science tomography: methodology, feasibility and computer simulation studies. *Phys. Med. Biol* **54**, 4687–4704 (2009).
- [301]. R.B. Schulz, J. Peter, W. Semmler and W. Bangerth. *Independent modeling of fluorescence excitation and emission with the finite element method*. Proceedings of the OSA Biomedical Topical Meetings (2004).
- [302]. Subhadra Srinivasan, Brian W. Pogue, Hamid Dehghani, Frederic Leblond and Xavier Intes. *Data subset algorithm for computationally-efficient reconstruction of 3-D spectral imaging in diffuse optical tomography*. *Opt. Express* **14**, 5394–5410 (2006).
- [303]. Z.M. Wang, G.Y. Panasyuk, V.A. Markel and J.C. Schotland. *Experimental demonstration of an analytic method for image reconstruction in optical diffusion tomography with large data sets*. *Opt Lett* **30**, 3338–3340 (2005).
- [304]. George Y. Panasyuk, Zheng-Min Wang, John C. Schotland and Vadim A. Markel. *Fluorescent optical tomography with large data sets*. *Opt. Lett.* **33**, 1744–1746 (2008).
- [305]. V.A. Markel and J.C. Schotland. *Symmetries, inversion formulas, and image reconstruction for optical tomography*. *Physical Review E* **70**, 056616–1–056616–19 (2004).
- [306]. Ilse C. F. Ipsen and Carl D. Meyer. *The Idea Behind Krylov Methods*. *American Mathematical Monthly* **105**, 889–899 (1998).
- [307]. S. Arridge and J. Schotland. *Optical tomography: forward and inverse problems*. Inverse Problems (accepted for publication) (2009).
- [308]. Matthew B Bouchard, Sarah A MacLaurin, Peter J Dwyer, James Mansfield, Richard Levenson and Thomas Krucker. *Technical considerations in longitudinal multispectral small animal molecular imaging*. *J Biomed Opt* **12**, 051601 (2007).
- [309]. N. Bloembergen. *Solid State Infrared Quantum Counters*. *Phys. Rev. Lett.* **2**, 84–85 (1959).
- [310]. F. Auzel. *Upconversion and anti-Stokes processes with f and d ions in solids*. *Chem. Rev* **104**, 139–174 (2004).
- [311]. JF Suyver, J. Grimm, MK Van Veen, D. Biner, KW Kramer and HU Gudel. *Upconversion spectroscopy and properties of NaYF₄ doped with Er³⁺, Tm³⁺ and/or Yb³⁺*. *Journal of Luminescence* **117**, 1–12 (2006).
- [312]. JF Suyver, A. Aebischer, D. Biner, P. Gerner, J. Grimm, S. Heer, KW Kramer, C. Reinhard and HU Gudel. *Novel materials doped with trivalent lanthanides and transition metal ions showing near-infrared to visible photon upconversion*. *Optical Materials* **27**, 1111–1130 (2005).
- [313]. G. Yi, H. Lu, S. Zhao, Y. Ge, W. Yang, D. Chen and L.H. Guo. *Synthesis, characterization, and biological application of size-controlled nanocrystalline NaYF₄: Yb, Er infrared-to-visible up-conversion phosphors*. *Nano Letters* **4**, 2191–2196 (2004).
- [314]. S. Jiang, Y. Zhang, K.M. Lim, E.K.W. Sim and L. Ye. *NIR-to-visible upconversion nanoparticles for fluorescent labeling and targeted delivery of siRNA*. *Nanotechnology* **20**, 155101 (2009).
- [315]. K. Moghissi, K. Dixon, M. Stringer, T. Freeman, A. Thorpe and S. Brown. *The place of bronchoscopic photodynamic therapy in advanced unresectable lung cancer: experience of 100 cases*. *Eur J Cardiothorac Surg* **15**, 1–6 (1999).
- [316]. U.O. Nseyo, J. DeHaven, T.J. Dougherty, W.R. Potter, D.L. Merrill, S.L. Lundahl and D.L. Lamm. *Photodynamic therapy (PDT) in the treatment of patients with resistant superficial bladder cancer: a long term experience*. *Journal of Clinical Laser Medicine & Surgery* **16**, 61–68 (1998).

- [317]. W.M. Star, H.P.A. Marijnissen, H. Jansen, M. Keijzer and M.J.C. VAN Gemert. *Light dosimetry for photodynamic therapy by whole bladder wall irradiation*. Photochemistry and Photobiology **46**, 619–624 (1987).
- [318]. JJ Schuitmaker, P. Baas, H. Van Leengoed, FW Van der Meulen, WM Star and N. Van Zandwijk. *Photodynamic therapy: a promising new modality for the treatment of cancer*. Journal of Photochemistry & Photobiology, B: Biology **34**, 3–12 (1996).
- [319]. T.J. Beck, F.W. Kreth, W. Beyer, J.H. Mehrkens, A. Obermeier, H. Stepp, W. Stummer and R. Baumgartner. *Interstitial photodynamic therapy of nonresectable malignant glioma recurrences using 5-aminolevulinic acid induced protoporphyrin IX*. Lasers in Surgery and Medicine **39**, 386 (2007).
- [320]. E. Kabingu, A.R. Oseroff, G.E. Wilding and S.O. Gollnick. *Enhanced systemic immune reactivity to a basal cell carcinoma associated antigen following photodynamic therapy*. Clinical Cancer Research **15**, 4460 (2009).
- [321]. U. Schmidt-Erfurth, J.W. Miller, M. Sickenberg, H. Laqua, I. Barbazetto, E.S. Gragoudas, L. Zografos, B. Piguat, C.J. Pournaras, G. Donati et al. *Photodynamic Therapy With Verteporfin for Choroidal Neovascularization Caused by Age-related Macular Degeneration: Results of Retreatments in a Phase 1 and 2 Study*. Archives of Ophthalmology **117**, 1177 (1999).
- [322]. Waseem Jerjes, Tahwinder Upile, Zaid Hamdoon, Farai Nhembe, Rishi Bhandari, Sorcha Mackay, Priya Shah, Charles Alexander Mosse, Jocelyn AS Brookes, Simon Morley and Colin Hopper. *Ultrasound-Guided Photodynamic Therapy for Deep Seated Pathologies Prospective Study*. Lasers in Surgery and Medicine **41**, 612–621 (2009).
- [323]. PJ Lou, HR Jäger, L. Jones, T. Theodossy, SG Bown and C. Hopper. *Interstitial photodynamic therapy as salvage treatment for recurrent head and neck cancer*. British journal of cancer **91**, 441–446 (2004).
- [324]. C.S. Betz, H.R. Jager, J.A.S. Brookes, R. Richards, A. Leunig and C. Hopper. *Interstitial photodynamic therapy for a symptom-targeted treatment of complex vascular malformations in the head and neck region*. Lasers in Surgery and Medicine **39** (2007).
- [325]. SG Bown, AZ Rogowska, DE Whitelaw, WR Lees, LB Lovat, P. Ripley, L. Jones, P. Wyld, A. Gillams and AWR Hatfield. *Photodynamic therapy for cancer of the pancreas*. Gut **50**, 549 (2002).
- [326]. J. Trachtenberg, A. Bogaards, R. A. Weersink, M. A. Haider, A. Evans, S. A. McCluskey, A. Scherz, M. R. Gertner, C. Yue, S. Appu, A. Aprikian, J. Savard, B. C. Wilson and M. Elhilali. *Vascular targeted photodynamic therapy with palladium-bacteriopheophorbide photosensitizer for recurrent prostate cancer following definitive radiation therapy: assessment of safety and treatment response*. J Urol **178**, 1974–9; discussion 1979 (2007).
- [327]. John Trachtenberg, Robert A Weersink, Sean R H Davidson, Masoom A Haider, Arjen Bogaards, Mark R Gertner, Andrew Evans, Avigdor Scherz, Joanne Savard, Joseph L Chin, Brian C Wilson and Mostafa Elhilali. *Vascular-targeted photodynamic therapy (padoporfin, WST09) for recurrent prostate cancer after failure of external beam radiotherapy: a study of escalating light doses*. BJU Int **102**, 556–562 (2008).
- [328]. K.L. Du, R. Mick, T. Busch, T.C. Zhu, J.C. Finlay, G. Yu, A.G. Yodh, S.B. Malkowicz, D. Smith, R. Whittington, D. Stripp and S.M. Hahn. *Preliminary results of interstitial motexafin lutetium-mediated PDT for prostate cancer*. Lasers Surg Med **38**, 427–434 (2006).
- [329]. M.J. Hammer-Wilson, M. Ghahramanlou and M.W. Berns. *Photo-*

- dynamic activity of lutetium-texaphyrin in a mouse tumor system.* Lasers in surgery and medicine **24**, 276–284 (1999).
- [330]. S.B. Brown, E.A. Brown and I. Walker. *The present and future role of photodynamic therapy in cancer treatment.* Lancet Oncology **5**, 497–508 (2004).
- [331]. Z Huang, H Xu, A D Meyers, A I Musani, L Wang, R Tagg, A B Barqawi and Y K Chen. *Photodynamic therapy for treatment of solid tumors—potential and technical challenges.* Technol Cancer Res Treat **7**, 309–320 (2008).
- [332]. B.J. Tromberg, L.O. Svaasand, M.K. Fehr, S.J. Madsen, P. Wyss, B. Sansone and Y. Tadir. *A mathematical model for light dosimetry in photodynamic destruction of human endometrium.* Phys Med Biol **41**, 223–237 (1996).
- [333]. WR Potter, TS Mang and TJ Dougherty. *The theory of photodynamic therapy dosimetry: consequences of photo-destruction of sensitizer.* Photochemistry and photobiology **46**, 97–101 (1987).
- [334]. HJ Nyst, RLP Van Veen, IB Tan, R. Peters, S. Spaniol, DJ Robinson, FA Stewart, PC Levendag and HJ Sterenborg. *Performance of a dedicated light delivery and dosimetry device for photodynamic therapy of nasopharyngeal carcinoma: Phantom and volunteer experiments.* Lasers in Surgery and Medicine **39**, 647–653 (2007).
- [335]. S.P. Pereira, L. Ayaru, A. Rogowska, A. Mosse, A.R.W. Hatfield and S.G. Bown. *Photodynamic therapy of malignant biliary strictures using meso-tetrahydroxyphenylchlorin.* European journal of gastroenterology & hepatology **19**, 479 (2007).
- [336]. H.C. Wolfsen. *Photodynamic therapy for pancreatic cancer: let's get serious.* Gastrointestinal Endoscopy **67**, 961–963 (2008).
- [337]. T. Xu, Y. Li and X. Wu. *Application of lower fluence rate for less microvasculature damage and greater cell-killing during photodynamic therapy.* Lasers in medical science **19**, 257–262 (2005).
- [338]. S.A. Blant, A. Woodtli, G. Wagnieres, C. Fontollet, H. Bergh and P. Monnier. *In vivo fluence rate effect in photodynamic therapy of early cancers with tetra (m-hydroxyphenyl) chlorin.* Photochemistry and photobiology **64**, 963–968 (1996).
- [339]. S. Coutier, S. Mitra, L.N. Bezdetsnaya, R.M. Parache, I. Georgakoudi, T.H. Foster and F. Guillemin. *Effects of fluence rate on cell survival and photobleaching in meta-tetra-(hydroxyphenyl)chlorin-photosensitized colo 26 multicell tumor spheroids.* Photochem Photobiol **73**, 297–303 (2001).
- [340]. S. Coutier, L.N. Bezdetsnaya, T.H. Foster, R.M. Parache and F. Guillemin. *Effect of irradiation fluence rate on the efficacy of photodynamic therapy and tumor oxygenation in meta-tetra (hydroxyphenyl) chlorin (mTHPC)-sensitized HT29 Xenografts in nude mice.* Radiat Res **158**, 339–345 (2002).
- [341]. B.W. Henderson, T.M. Busch and J.W. Snyder. *Fluence rate as a modulator of PDT mechanisms.* Lasers Surg Med **38**, 489–493 (2006).
- [342]. TM Busch, EP Wileyto, MJ Emanuele, F. Del Piero, L. Marconato, E. Glatstein and CJ Koch. *Photodynamic therapy creates fluence rate-dependent gradients in the intratumoral spatial distribution of oxygen.* Cancer research **62**, 7273 (2002).
- [343]. T. H. Foster, R. S. Murant, R. G. Bryant, R. S. Knox, S. L. Gibson and R. Hilf. *Oxygen consumption and diffusion effects in photodynamic therapy.* Radiat Res **126**, 296–303 (1991).
- [344]. H. Tsutsui, A.J. MacRobert, A. Curnow, A. Rogowska, G. Buonaccorsi, H. Kato and S.G. Bown. *Optimisation of illumination for photodynamic*

- therapy with *m*THPC on normal colon and a transplantable tumour in rats. *Lasers Med Sci* **17**, 101–109 (2002).
- [345]. T.H. Pham, R. Hornung, M.W. Berns, Y. Tadir and B.J. Tromberg. *Monitoring tumor response during photodynamic therapy using near-infrared photon-migration spectroscopy*. *Photochem Photobiol* **73**, 669–677 (2001).
- [346]. A. Johansson, T. Johansson, M. Soto Thompson, N. Bendsoe, K. Svanberg, S. Svanberg and S. Andersson-Engels. *In vivo measurement of parameters of dosimetric importance during photodynamic therapy of thick skin tumors*. *J Biomed Opt.* **11**, 0 (2006).
- [347]. I. Georgakoudi and T.H. Foster. *Effects of the subcellular redistribution of two nile blue derivatives on photodynamic oxygen consumption*. *Photochemistry and photobiology* **68**, 115–122 (1998).
- [348]. J Buchholz, B Kaser-Hotz, T Khan, C Rohrer Bley, K Melzer, R A Schwendener, M Roos and H Walt. *Optimizing photodynamic therapy: in vivo pharmacokinetics of liposomal meta-(tetrahydroxyphenyl)chlorin in feline squamous cell carcinoma*. *Clin Cancer Res* **11**, 7538–7544 (2005).
- [349]. W.M. Sharman, J.E. van Lier and C.M. Allen. *Targeted photodynamic therapy via receptor mediated delivery systems*. *Advanced drug delivery reviews* **56**, 53–76 (2004).
- [350]. B Chen, BW Pogue, PJ Hoopes and T Hasan. *Combining vascular and cellular targeting regimens enhances the efficacy of photodynamic therapy*. *International Journal of Radiation Oncology Biology Physics* **61**, 1216–1226 (2005).
- [351]. H.J. Jones, D.I. Vernon and S.B. Brown. *Photodynamic therapy effect of *m*-THPC (Foscanr) in vivo: correlation with pharmacokinetics*. *Br J Cancer* **89**, 398–404 (2003).
- [352]. W. Alian, S. Andersson-Engels and S. Svanberg. *Laser-induced fluorescence studies of meso-tetra (hydroxyphenyl) chlorin in malignant and normal tissues in rats*. *British journal of cancer* **70**, 880–885 (1994).
- [353]. R.B. Veenhuizen, M.C. Ruevekamp, H. Oppelaar, T.J.M. Helmerhorst, P. Kenemans and F.A. Stewart. *Foscan-mediated photodynamic therapy for a peritoneal-cancer model: Drug distribution and efficacy studies*. *Int J Cancer* **73**, 230–235 (1997).
- [354]. P. Cramers, M. Ruevekamp, H. Oppelaar, O. Dalesio, P. Baas and F.A. Stewart. *Foscan uptake and tissue distribution in relation to photodynamic efficacy*. *Br J Cancer* **88**, 283–290 (2003).
- [355]. M. Triesscheijn, M. Ruevekamp, M. Aalders, P. Baas and F.A. Stewart. *Outcome of *m*THPC mediated photodynamic therapy is primarily determined by the vascular response*. *Photochem Photobiol* **81**, 1161–1167 (2005).
- [356]. J.C. Finlay, S. Mitra and T.H. Foster. *In vivo *m*THPC photobleaching in normal rat skin exhibits unique irradiance-dependent features*. *Photochem Photobiol* **75**, 282–288 (2002).
- [357]. A. MPhil, M.R. Stringer, J.E. Cruse-Sawyer and S.B. Brown. *Fluence-rate effects upon *m*-THPC photobleaching in a formalin-fixed cell system*. *Photodiagnosis and Photodynamic Therapy* **1**, 173 – 180 (2004).
- [358]. M.S. Patterson, B.C. Wilson and R. Graff. *In vivo tests of the concept of photodynamic threshold dose in normal rat liver photosensitized by aluminum chlorosulphonated phthalocyanine*. *Photochemistry and Photobiology* **51**, 343–349 (1990).
- [359]. Theresa M Busch. *Local physiological changes during photodynamic therapy*. *Lasers Surg Med* **38**, 494–499 (2006).
- [360]. MC Berenbaum, R. Bonnett and PA Scourides. *In vivo biological activ-*

- ity of the components of haematoporphyrin derivative. *British Journal of Cancer* **45**, 571 (1982).
- [361]. JC Van Gemert, MC Berenbaum and GH Gijsbers. *Wavelength and light-dose dependence in tumour phototherapy with haematoporphyrin derivative*. *British Journal of Cancer* **52**, 43 (1985).
- [362]. X.G. Xu, B. Bednarz and H. Paganetti. *A review of dosimetry studies on external-beam radiation treatment with respect to second cancer induction*. *Phys. Med. Biol* **53**, R193–R241 (2008).
- [363]. BW Pogue, T. Momma, HC Wu and T. Hasan. *Transient absorption changes in vivo during photodynamic therapy with pulsed-laser light*. *British Journal of Cancer* **80**, 344–351 (1999).
- [364]. B.W. Pogue, J.A. O'Hara, I.A. Goodwin, C.J. Wilmot, G.P. Fournier, A.R. Akay and H. Swartz. *Tumor PO₂ changes during photodynamic therapy depend upon photosensitizer type and time after injection*. *Comparative Biochemistry and Physiology A-Molecular and Integrative Physiology* **132**, 177–184 (2002).
- [365]. B. Chen. *Tumor vascular permeabilization by vascular-targeting photosensitization: Effects, mechanism, and therapeutic implications*. *Clinical Cancer Research* **12**, 917–923 (2006). 1.
- [366]. J.H. Woodhams, L. Kunz, S.G. Bown and A.J. MacRobert. *Correlation of real-time haemoglobin oxygen saturation monitoring during photodynamic therapy with microvascular effects and tissue necrosis in normal rat liver*. *Br J Cancer* **91**, 788–794 (2004).
- [367]. S. Gross, A. Gilead, A. Scherz, M. Neeman and Y. Salomon. *Monitoring photodynamic therapy of solid tumors online by BOLD-contrast MRI*. *Nature medicine* **9**, 1327–1331 (2003).
- [368]. G. Yu, T. Durduran, C. Zhou, H.W. Wang, M.E. Putt, H.M. Saunders, C.M. Sehgal, E. Glatstein, A.G. Yodh and T.M. Busch. *Noninvasive Monitoring of Murine Tumor Blood Flow During and After Photodynamic Therapy Provides Early Assessment of Therapeutic Efficacy*. *Clinical Cancer Research* **11**, 3543 (2005).
- [369]. B.A. Standish, K.K.C. Lee, X. Jin, A. Mariampillai, N.R. Munce, M.F.G. Wood, B.C. Wilson, I.A. Vitkin and V.X.D. Yang. *Interstitial Doppler Optical Coherence Tomography as a Local Tumor Necrosis Predictor in Photodynamic Therapy of Prostatic Carcinoma: An In vivo Study*. *Cancer Research* **68**, 9987 (2008).
- [370]. L. Xiang, H. Gu, D. Yang, S. Yang, L. Zeng and W.R. Chen. *Real-time optoacoustic monitoring of vascular damage during photodynamic therapy treatment of tumor*. *Journal of Biomedical Optics* **12**, 014001 (2007).
- [371]. Masoom A Haider, Sean R H Davidson, Ashwini V Kale, Robert A Weersink, Andrew J Evans, Ants Toi, Mark R Gertner, Arjen Bogaards, Brian C Wilson, Joseph L Chin, Mostafa Elhilali and John Trachtenberg. *Prostate gland: MR imaging appearance after vascular targeted photodynamic therapy with palladium-bacteriopheophorbide*. *Radiology* **244**, 196–204 (2007).
- [372]. M. Niedre, M.S. Patterson and B.C. Wilson. *Direct Near-infrared Luminescence Detection of Singlet Oxygen Generated by Photodynamic Therapy in Cells In Vitro and Tissues In Vivo*. *Photochemistry and photobiology* **75**, 382–391 (2002).
- [373]. M.J. Niedre, A.J. Secord, M.S. Patterson and B.C. Wilson. *In vitro tests of the validity of singlet oxygen luminescence measurements as a dose metric in photodynamic therapy*. *Cancer Res* **63**, 7986–7994 (2003).
- [374]. M.J. Niedre, C.S. Yu, M.S. Patterson and B.C. Wilson. *Singlet oxygen*

- luminescence as an in vivo photodynamic therapy dose metric: validation in normal mouse skin with topical amino-levulinic acid.* Br J Cancer **92**, 298–304 (2005).
- [375]. M.J. Niedre, M.S. Patterson, A. Giles and B.C. Wilson. *Imaging of photodynamically generated singlet oxygen luminescence in vivo.* Photochem Photobiol **81**, 941–943 (2005).
- [376]. Hans-Joachim Laubach, Sung K. Chang, Seonkyung Lee, Imran Rizvi, David Zurakowski, Steven J. Davis, Charles R. Taylor and Tayyaba Hasan. *In-vivo singlet oxygen dosimetry of clinical 5-aminolevulinic acid photodynamic therapy.* Journal of Biomedical Optics **13**, 050504 (2008).
- [377]. I. Georgakoudi, M.G. Nichols and T.H. Foster. *The mechanism of Photofrin photobleaching and its consequences for photodynamic dosimetry.* Photochemistry and photobiology **65**, 135–144 (1997).
- [378]. J.C. Finlay, S. Mitra, M.S. Patterson and T.H. Foster. *Photobleaching kinetics of Photofrin in vivo and in multicell tumour spheroids indicate two simultaneous bleaching mechanisms.* Physics in medicine and biology **49**, 4837–4860 (2004).
- [379]. C. Sheng, P. Jack Hoopes, T. Hasan and B.W. Pogue. *Photobleaching-based dosimetry predicts deposited dose in ALA-PpIX PDT of rodent esophagus.* Photochemistry and Photobiology **83**, 738–748 (2007).
- [380]. J.S. Dysart and M.S. Patterson. *Characterization of Photofrin photobleaching for singlet oxygen dose estimation during photodynamic therapy of MLL cells in vitro.* Physics in Medicine and Biology **50**, 2597–2616 (2005).
- [381]. J.S. Dysart and M.S. Patterson. *Photobleaching kinetics, photoproduct formation, and dose estimation during ALA induced PpIX PDT of MLL cells under well oxygenated and hypoxic conditions.* Photochemical and Photobiological Sciences **5**, 73–81 (2006).
- [382]. JC Finlay, DL Conover, EL Hull and TH Foster. *Porphyrin Bleaching and PDT-induced Spectral Changes are Irradiance Dependent in ALA-sensitized Normal Rat Skin In Vivo.* Photochemistry and Photobiology **73**, 54–63 (2001).
- [383]. D.J. Robinson, H.S. Bruijn, N. Veen, M.R. Stringer, S.B. Brown and W.M. Star. *Fluorescence photobleaching of ALA-induced protoporphyrin IX during photodynamic therapy of normal hairless mouse skin: the effect of light dose and irradiance and the resulting biological effect.* Photochemistry and photobiology **67**, 140–149 (1998).
- [384]. J.S. Dysart, G. Singh and M.S. Patterson. *Calculation of singlet oxygen dose from photosensitizer fluorescence and photobleaching during mTHPC photodynamic therapy of MLL cells.* Photochem Photobiol **81**, 196–205 (2005).
- [385]. J. Moan and K. BERG. *The photodegradation of porphyrins in cells can be used to estimate the lifetime of singlet oxygen.* Photochemistry and photobiology **53**, 549–553 (1991).
- [386]. Brian C. Wilson and Michael S. Patterson. *The physics, biophysics and technology of photodynamic therapy.* PHYSICS IN MEDICINE AND BIOLOGY **53**, R61–R109 (2008).
- [387]. A. Dimofte, T.C. Zhu, S.M. Hahn and R.A. Lustig. *In vivo light dosimetry for motecafin lutetium-mediated PDT of breast cancer.* Lasers Surg Med **31**, 305–312 (2002).
- [388]. L. Lilje, N. Pomerleau-Dalcourt, A. Douplik, S.H. Selman, R.W. Keck, M. Szkudlarek, M. Pestka and J. Jankun. *Transperineal in vivo fluorescence dosimetry in the canine prostate during SnET2-mediated PDT.* Phys Med Biol **49**, 3209–3225 (2004).

- [389]. R.A. Weersink, A. Bogaards, M. Gertner, S.R.H. Davidson, K. Zhang, G. Netchev, J. Trachtenberg and B.C. Wilson. *Techniques for delivery and monitoring of TOOKAD (WST09)-mediated photodynamic therapy of the prostate: Clinical experience and practicalities*. Journal of Photochemistry and Photobiology B-Biology **79**, 211–222 (2005).
- [390]. T.C. Zhu, A. Dimofte, J.C. Finlay, D. Stripp, T. Busch, J. Miles, R. Whittington, S.B. Malkowicz, Z. Tochner, E. Glatstein and S.M. Hahn. *Optical Properties of Human Prostate at 732 nm Measured In Vivo During Motexafin Lutetium-mediated Photodynamic Therapy*. Photochem Photobiol **81**, 96–105 (2005).
- [391]. T.C. Zhu, J.C. Finlay and S.M. Hahn. *Determination of the distribution of light, optical properties, drug concentration, and tissue oxygenation in-vivo in human prostate during motexafin lutetium-mediated photodynamic therapy*. Journal of Photochemistry and Photobiology B: Biology **79**, 231–241 (2005).
- [392]. K.K.H. Wang and T.C. Zhu. *Reconstruction of in-vivo optical properties for human prostate using interstitial diffuse optical tomography*. Optics Express **17**, 11665–11672 (2009).
- [393]. G. Xu, D. Piao, CH Musgrove, CF Bunting and H. Dehghani. *Trans-rectal ultrasound-coupled near-infrared optical tomography of the prostate, part I: simulation*. Optics Express **16**, 17484 (2008).
- [394]. Z. Jiang, D. Piao, G. Xu, J.W. Ritchey, GR Holyoak, K.E. Bartels, C.F. Bunting, G. Slobodov and J.S. Krasinski. *Trans-rectal ultrasound-coupled near-infrared optical tomography of the prostate, Part II: Experimental demonstration*. Optics Express **16**, 17505–17520 (2008).
- [395]. Chengyu Li, Raweevan Liengsawangwong, Haesun Choi and Rex Cheung. *Using a priori structural information from magnetic resonance imaging to investigate the feasibility of prostate diffuse optical tomography and spectroscopy: A simulation study*. Medical Physics **34**, 266–274 (2007).
- [396]. D. J. Dickey, R. B. Moore, D. C. Rayner and J. Tulip. *Light dosimetry using the P3 approximation*. Phys Med Biol **46**, 2359–2370 (2001).
- [397]. Dwayne J. Dickey, Kevin Partridge, Ronald B. Moore and John Tulip. *Light dosimetry for multiple cylindrical diffusing sources for use in photodynamic therapy*. Phys Med Biol **49**, 3197–3208 (2004).
- [398]. SR Davidson, R.A. Weersink, M.A. Haider, M.R. Gertner, A. Bogaards, D. Giewercer, A. Scherz, M.D. Sherar, M. Elhilali, J.L. Chin et al. *Treatment planning and dose analysis for interstitial photodynamic therapy of prostate cancer*. Physics in Medicine and Biology **54**, 2293 (2009).
- [399]. J. Li and T. C. Zhu. *Determination of in vivo light fluence distribution in a heterogeneous prostate during photodynamic therapy*. PHYSICS IN MEDICINE AND BIOLOGY **53**, 2103–2114 (2008).
- [400]. M.D. Altschuler, T.C. Zhu, J. Li and S.M. Hahn. *Optimized interstitial PDT prostate treatment planning with the Cimmino feasibility algorithm*. Med Phys **32**, 3524–3536 (2005).
- [401]. Jun Li, Martin D Altschuler, Stephen M Hahn and Timothy C Zhu. *Optimization of light source parameters in the photodynamic therapy of heterogeneous prostate*. Physics in Medicine and Biology **53**, 4107–4121 (2008).
- [402]. Augusto Rendon, J Christopher Beck and Lothar Lilje. *Treatment planning using tailored and standard cylindrical light diffusers for photodynamic therapy of the prostate*. Physics in Medicine and Biology **53**, 1131–1149 (2008).
- [403]. J.H. Woodhams, A.J. MacRobert and S.G. Bown. *The role of oxygen monitoring during photodynamic therapy and its potential for treatment*

- dosimetry*. Photochemical and Photobiological Sciences **6**, 1246–1256 (2007).
- [404]. G.Q. Yu, T. Durduran, C. Zhou, T.C. Zhu, J.C. Finlay, T.M. Busch, S.B. Malkowicz, S.M. Hahn and A.G. Yodh. *Real-time in situ monitoring of human prostate photodynamic therapy with diffuse light*. Photochem Photobiol **82**, 1279–1284 (2006).
- [405]. K. K. H. Wang. *A comprehensive mathematical model of microscopic dose deposition in photodynamic therapy*. Medical Physics **34**, 282–293 (2007).
- [406]. T. Windahl, S. O. Andersson and L. Lofgren. *Photodynamic therapy of localised prostatic cancer*. Lancet **336**, 1139 (1990).
- [407]. Dirk Zaak, Ronald Sroka, Michael Höppner, Wael Khoder, Oliver Reich, Stefan Tritschler, Rolf Muschter, Ruth Knüchel and Alfons Hofstetter. *Photodynamic Therapy by Means of 5-ALA Induced PPIX in Human Prostate Cancer - Preliminary Results*. Medical Laser Application **18**, 91 – 95 (2003).
- [408]. T.R. Nathan, D.E. Whitelaw, S.C. Chang, W.R. Lees, P.M. Ripley, H. Payne, L. Jones, M.C. Parkinson, M. Emberton, A.R. Gillams, A.R. Mundy and S.G. Bown. *Photodynamic Therapy for Prostate Cancer Recurrence After Radiotherapy: A Phase I Study*. J Urol **168**, 1427–1432 (2002).
- [409]. C.M. Moore, T.R. Nathan, W.R. Lees, C.A. Mosse, A. Freeman, M. Emberton and S.G. Bown. *Photodynamic therapy using meso tetra hydroxy phenyl chlorin (mTHPC) in early prostate cancer*. Lasers Surg Med **38**, 356–363 (2006).
- [410]. K Verigos, DCH Stripp, R Mick, TC Zhu, R Whittington, D Smith, A Dimofte, J Finlay, TM Busch, ZA Tochner, SB Malkowicz, E Glatstein and SM Hahn. *Updated results of a phase I trial of motexafin lutetium-mediated interstitial photodynamic therapy in patients with locally recurrent prostate cancer*. JOURNAL OF ENVIRONMENTAL PATHOLOGY TOXICOLOGY AND ONCOLOGY **25**, 373–387 (2006).
- [411]. Hiral Patel, Rosemarie Mick, Jarod Finlay, Timothy C Zhu, Elizabeth Rickter, Keith A Cengel, S. Bruce Malkowicz, Stephen M Hahn and Theresa M Busch. *Motexafin lutetium-photodynamic therapy of prostate cancer: short- and long-term effects on prostate-specific antigen*. Clin Cancer Res **14**, 4869–4876 (2008).
- [412]. Thomas Johansson, Marcelo Soto Thompson, Maria Stenberg, Klinteberg Claes af, Stefan Andersson-Engels, Sune Svanberg and Katarina Svanberg. *Feasibility study of a system for combined light dosimetry and interstitial photodynamic treatment of massive tumors*. Appl Opt **41**, 1462–1468 (2002).
- [413]. M. Soto-Thompson, A. Johansson, T. Johansson, S. Andersson-Engels, S. Svanberg, N. Bendsoe and K. Svanberg. *Clinical system for interstitial photodynamic therapy with combined on-line dosimetry measurements*. Appl Opt **44**, 4023–4031 (2005).
- [414]. Ann Johansson, Johan Axelsson, Johannes Swartling, Thomas Johansson, Sara Palsson, Johan Stensson, Margret Einarsdottir, Katarina Svanberg, Niels Bendsoe, Karl Mikael Kalkner, Sten Nilsson, Sune Svanberg and Stefan Andersson-Engels. *Interstitial photodynamic therapy for primary prostate cancer incorporating real-time treatment dosimetry*. In David Kessel, editor, *Optical Methods for Tumor Treatment and Detection: Mechanisms and Techniques in Photodynamic Therapy XVI* p 64270O. SPIE vol. 6427 (2007).
- [415]. U. Gustafsson, S. Palsson and S. Svanberg. *Compact fibre-optic fluorosensor using a continuous wave violet diode laser and an integrated*

-
- spectrometer*. Rev Sci Instrum **71**, 3004–3006 (2000).
- [416]. Y. Censor, M.D. Altschuler and W.D. Powlis. *On the Use of Cimmino Simultaneous Projections Method for Computing A Solution of the Inverse Problem in Radiation-Therapy Treatment Planning*. Inverse Probl **4**, 607–623 (1988).
- [417]. Tomas Svensson, Erik Alerstam, Margret Einarsdottir, Katarina Svanberg and Stefan Andersson-Engels. *Towards accurate in vivo spectroscopy of the human prostate*. Journal of Biophotonics **1**, 200–203 (2008).
- [418]. K. D. Paulsen and H. Jiang. *Spatially varying optical property reconstruction using a finite element diffusion equation approximation*. Med Phys **22**, 691–701 (1995).
- [419]. A. Roggan, M. Friebel, K. Doerschel, A. Hahn and G.J. Mueller. *Optical properties of circulating human blood*. In *Proceedings of SPIE* p 51 vol. 3195 (1998).